SYNTHESIS AND CHARACTERIZATION OF Zn (ZINC), Co (COBALT), Fe (IRON) CONTAINING METAL ORGANIC FRAMEWORKS (MOFs) FOR MICROBIAL FUEL CELLS (MFCs)

by

Müşerref Eryılmaz

B.S., Chemistry, Boğaziçi University, 2020

Submitted to the Institute for Graduate Studies in

Science and Engineering in partial fulfillment of

the requirements for the degree of

Master of Science

Graduate Program in Chemistry

Boğaziçi University

2023

ACKNOWLEDGEMENTS

First of all, I would like to express my gratitude to my thesis advisor Assoc. Prof. Oktay Demircan for his continuous support, encouragement and most importantly the chance to do research in a field where I am highly interested in.

I want to give my deepest appreciation to my thesis committee members, Prof. A. Neren ÖKTE and Prof. Emren NALBANT for reviewing my thesis with their valuable time.

In addition, I would like to acknowledge that this thesis has been supported by TÜBİTAK National MSc Scholarship Program for Former Undergraduate Scholars (BİDEB 2210/E).

I am also very grateful for the continuous support and help my lab mates, Eslem, Çağla, Hüseyin, and Janset, have given me throughout my thesis study.

Finally, I would like to thank my family and my beloved friends, my mother Nilda, my father Bülent, my sister Zeynep, my grandmother Ayla and my best friends in the whole world Furkan and Ece. I am very grateful that they were always there for me with their understanding, endless support, encouragement, compassion, and love.

ABSTRACT

SYNTHESIS AND CHARACTERIZATION OF Zn (ZINC), Co (COBALT), Fe (IRON) CONTAINING METAL ORGANIC FRAMEWORKS (MOFs) FOR MICROBIAL FUEL CELLS (MFCs)

Metal organic Frameworks (MOFs) with their unique characteristics such as high surface area, variable functionalities and structural diversity, stability, and porous structure can be used as Microbial Fuel Cell (MFC) cathode catalysts. In this study, MOFs are synthesized from metal salts of zinc (Zn), cobalt (Co) and iron (Fe) and organic linkers as fumaric acid, terephthalic acid, 2-aminoterephthalic acid and 2-methlyimidazole via room temperature and sonochemical synthesis methods which are easy and energy-efficient. Effect of metal doping, reactant molar ratios and concentrations and metal ion precursors on synthesis of MOFs were investigated and formed frameworks are characterized by Scanning Electron Microscopy/Energy Dispersive X-Ray Analysis and X-Ray Diffraction Analysis. Obtained MOFs' applicability as Microbial Fuel Cell (MFC) cathode catalysts are studied by preparing slurries with carbon black (CB) and polyvinyl alcohol (PVA) as binder, coating them on stainless-steel mesh (SSM) current collectors for the first time. Electrochemical characterization of coated SSMs were performed via Chronopotentiometry and Cyclic Voltammetry (CV) and morphology of the coatings were established via SEM. SSM coated with 80% ZIF-L/10% CB/10% PVA slurry demonstrated the best oxygen reduction reaction (ORR) performance via CV. SSMs with ZIF-8/CB/PVA, ZIF-L/CB/PVA, Zn-doped ZIF-67/CB/PVA, and MIL-88A/CB/PVA composites that had demonstrated catalytic activity towards ORR utilized in MFCs for further performance analysis by Open Circuit Voltage (OCV), Linear Sweep Voltammetry (LSV) and Electrochemical Impedance Spectroscopy (EIS) in a two-chamber MFC inoculated with E.Coli K-12. Among the MFCs with novel cathodes, MFC with SSM cathode containing 80% ZIF-L/10% CB/10% PVA coating demonstrated the lowest charge transfer resistance and highest current density.

ÖZET

MİKROBİYAL YAKIT HÜCRELERİNDE (MYH) KULLANILMAK ÜZERE Zn (ÇİNKO), Co (KOBALT), Fe (DEMİR) İÇEREN METAL ORGANİK KAFES YAPILARIN (MOFs) SENTEZİ VE KARAKTERİZASYONU

Yüksek yüzey alanı, değişken işlevsellikler ve yapısal çeşitlilik, kararlılık ve gözenekli yapı gibi özellikleri sayesinde metal organik kafesler (MOFs), Mikrobiyal Yakıt Hücresi (MYH) katot katalizörleri olarak kullanılabilir. Bu çalışmada, çinko (Zn), kobalt (Co) ve demirin (Fe) metal tuzlarından, fumarik asit, tereftalik asit, 2-aminotereftalik asit ve 2-metilimidazol gibi organik bağlayıcılardan kolay ve enerji verimli sonokimyasal ve oda sıcaklığında sentez metotlarıyla MOF yapılar sentezlendi. Metal katkılamanın, kullanılan metal tuzunun, reaktant molar oranlarının ve konsantrasyonlarının MOF yapıları üzerindeki etkisi araştırılmış ve oluşan malzemeler Taramalı Elektron Mikroskobu/Enerji Dağılımlı X-Işını Analizi (SEM/EDX) ve X-Işını Kırınım Analizi (XRD) ile incelenmiştir. Elde edilen MOF yapılarının MYH katot katalizörü olarak uygulanabilirliği karbon siyahı (CB) ve bağlayıcı olarak polivinil alkol (PVA) içeren bulamaçlar hazırlanarak paslanmaz çelik ağ (stainless-steel mesh, SSM) akım toplayıcıları üzerine kaplanarak ilk kez incelenmiştir. Kaplanmış SSM morfolojileri SEM, elektrokimyasal özellikleri ise Kronopotansiyometri ve Dönüşümlü Voltametri (CV) ile gerçekleştirilmiştir. CV analizlerinde en iyi oksijen indirgenme performansı %80 ZIF-L/%10 CB/%10 PVA içeren bulamaç ile kaplanmış SSM ile gözlenmiştir. ZIF-8/CB/PVA, ZIF-L/CB/PVA, Zn-katkılı ZIF-67/CB/PVA ve MIL-88A/CB/PVA kompozit kaplamalarına sahip katotlar E. Coli K-12 ile aşılanmış iki bölmeli MYH'lerinde kullanılarak performansları Açık Devre Gerilimi (OCV), Doğrusal Taramalı Voltametri (LSV) ve Elektrokimyasal İmpedans Spektroskopi (EIS) ile araştırılmış ve %80 ZIF-L/%10 CB/%10 PVA içeren kaplamaya sahip katotlu MYH, en düşük yük aktarım direncini ve en yüksek akım yoğunluğunu göstermiştir.

TABLE OF CONTENTS

ACKNOWLEDGEMENTS ii

ABSTRACT iii

ÖZET iv

LIST OF FIGURES viii

LIST OF TABLES xix

LIST OF ACRONYMS/ABBREVIATIONS xx

1. INTRODUCTION 1

1.1. Microbial Fuel Cells (MFCs) 1

1.1.1. Working Principles 1

1.1.2. Factors Affecting MFC Performance 4

1.2. Metal Organic Frameworks (MOFs) 11

1.2.1. Design and Synthesis of MOFs 14

1.2.2. Factors Affecting MOF Synthesis 19

1.2.3. MOFs Applications in MFCs 21

2. SCOPE OF THESIS 24

3. EXPERIMENTAL 26

3.1. Materials 26

3.2. Synthesis of Metal Organic Frameworks 27

3.2.1. Zn-MOFs 27

3.2.1.1. Zn^{II}(2-MeIm).H_2O (ZIF-L). 27

3.2.1.2. Zn^{II}(2-MeIm).MeOH (ZIF-8) and M/Zn^{II}(2-MeIm).MeOH. 28

3.2.2. Co-MOFs 30

3.2.2.1. Co^{II}(2-MeIm).H_2O (ZIF-67-1) and M/Co^{II}(2-MeIm).H_2O. 30

3.2.2.2. Co^{II}(2-MeIm).MeOH/EtOH (ZIF-67-2) and M/Co^{II} (2-MeIm).MeOH/EtOH. 30
3.2.3. Fe-MOFs 32
3.2.3.1. Fe^{III}(FA).H_2O/EtOH (MIL-88A) and M/Fe^{III}(FA).H_2O/EtOH. 32
3.2.3.2. Fe^{III}(TPA).DMF. 33
3.2.3.3. Fe^{III}(NH_2-TPA).DMF and Co^{II}/Fe^{III}(NH_2-TPA).DMF. 33
3.3. Preparation of Coated Stainless-Steel Mesh (SSM) Electrodes 34
3.3.1. SSM Electrodes Coated with Carbon Slurries 35
3.3.1.1. Binder-Free Coating. 35
3.3.1.2. Coatings with PVA Binder. 35
3.3.2. SSM Electrodes Coated with MOF and MOF-Carbon Composite Slurries 36
3.4. Setup of MFC and Bacterial Inoculation 40
3.5. Characterization Methods 42
3.5.1. X-Ray Diffraction Analysis (XRD) 42
3.5.2. Scanning Electron Microscopy/Energy Dispersive X-Ray Analysis (SEM/EDX) 42
3.5.3. Chronopotentiometry 43
3.5.4. Electrochemical Impedance Spectroscopy (EIS) 44
3.5.5. Cyclic Voltammetry (CV) 45
3.5.6. Open Circuit Voltage Analysis (OCV) 45
3.5.7. Linear Sweep Voltammetry (LSV) 46
4. RESULTS AND DISCUSSION 47
4.1. Characterization of Zn-MOFs 47
4.1.1. Zn^{II}(2-MeIm).H_2O (ZIF-L) 47
4.1.2. Zn^{II}(2-MeIm).MeOH (ZIF-8) 49
4.2. Characterization of Co-MOFs 55

4.2.1. Co^{II}(2-MeIm).H_2O (ZIF-67-1) and M/Co^{II}(2-MeIm).H_2O 55

4.2.2. $Co^{II(}$2-MeIm).MeOH/EtOH (ZIF-67-2) and M/Co^{II}(2-MeIm).MeOH/EtOH 58

4.3. Characterization of Fe-MOFs 62

4.3.1. Fe^{III}(FA).H_2O/EtOH (MIL-88A) 62

4.3.2. Fe^{III}(TPA).DMF 64

4.3.3. Fe^{III}(NH_2-TPA).DMF (Fe-MIL-88B) and Co^{II}/ Fe^{III}(NH_2-TPA).DMF 68

4.4. Characterization of Prepared Electrodes 71

4.4.1. SSMs Coated with Carbon Slurries 71

4.4.1.1. SSMs Coated with Binder-Free Coating. 71

4.4.1.2. SSMs Coated with PVA Binder Containing Carbon Slurries. 72

4.4.4. SSMs Coated with MOF Containing Slurries 77

4.5. Performance of SSM Electrodes in MFCs 96

5. CONCLUSION 109

6. FUTURE WORK 111

REFERENCES 113

APPENDIX A: COPYRIGHT NOTICES 133

LIST OF FIGURES

Figure 1.1. Schematic illustration of a two-chamber microbial fuel cell and its working mechanism. 2

Figure 1.2. Schematic illustration of electron transfer mechanisms between microorganisms and the electrode. 4

Figure 1.3. Schematic representations of (a) two-chamber and (b) single-chamber MFCs. 6

Figure 1.4. Schematic representation of ORR with 2 e^- and 4 e^- pathway. 10

Figure 1.5. Schematic representation of MOF formation. 12

Figure 1.6. Illustration of SBUs and arrangements of metals in BMOFs [82]. 13

Figure 1.7. Effect of metal ions/clusters with different connection geometry on produced MOF [92]. 15

Figure 1.8. Commonly used synthesis methods of MOFs. 16

Figure 3.1. Pictures of Zn-MOFs (a) ZIF-L-1, (b) ZIF-L-2, (c) ZIF-8-1, (d) Co doped ZIF-8-1, (e) Fe-doped ZIF-8-1, (f) Ni-doped ZIF-8-1, (g) ZIF-8-2 and (h) ZIF-8-3 respectively. 29

Figure 3.2. Pictures of the synthesized Co-MOFs, (a) ZIF-67-1, (b) Fe-doped ZIF-67-1, (c) Mn-doped ZIF-67-1 (d) Ni-doped ZIF-67-1 (e) ZIF-67-2 and (f) Zn-doped ZIF-67-2 respectively. 31

Figure 3.3. Pictures of synthesized Fe-MOFs, (a) MIL-88A-1, (b) MIL-88A-2, (c) Co-doped MIL-88A-2, (d) Zn-doped MIL-88A-2, (e) Fe^{III}(TPA).DMF-1, (f) Fe^{III}(TPA).DMF-2, (g) Fe^{III}(NH_2-TPA).DMF, (h) Co^{II}/Fe^{III}(NH_2 -TPA).DMF respectively..... 34

Figure 3.4. Image of the drawing (a) and constructed MFC (b). 41

Figure 3.5. Schematic representation of physical chronopotentiometry measurements by four probes with equal spacing, shown as “l”. 43

Figure 3.6. An example of a chronopotentiogram obtained from physical chronopotentiometry measurement. 44

Figure 4.1. SEM images of ZIF-L-1 at (a) 5000x, (b) 10000x and ZIF-L-2 at (c) 5000x, (d) 10000x zoom level. 47

Figure 4.2. SEM images of (a) ZIF-L-1 and (b) ZIF-L-2. 48

Figure 4.3. XRD pattern of ZIF-L-1 and ZIF-L-2. 48

Figure 4.4. Figure 4.4. SEM images of ZIF-8-1 at (a) 50000x and (b) 100000x zoom level. 49

Figure 4.5. XRD pattern of ZIF-8-1. 50

Figure 4.6. SEM images of ZIF-8-2 at (a) 50000x and (b) 100000x zoom level. 50

Figure 4.7. XRD pattern of ZIF-8-2. 51

Figure 4.8. SEM images of ZIF-8-3 at (a) 50000x and (b) 200000x zoom level. 52

Figure 4.9. XRD pattern of ZIF-8-3. 52

Figure 4.10. XRD pattern of all synthesized single metal ZIF-8s. 53

Figure 4.11. SEM images of (a) and (b) Ni-doped ZIF-8-1, (c) and d) Co-doped ZIF 8-1, (e) and (f) Fe-doped ZIF-8-1 respectively. 54

Figure 4.12. XRD pattern of ZIF-8-1 and bimetallic ZIF-8s. 55

Figure 4.13. SEM images of ZIF-67-1 at (a) 10000x and (b) 50000x zoom level. 56

Figure 4.14. XRD pattern of ZIF-67-1. 56

Figure 4.15. SEM images of (a) and (b) Fe-doped ZIF-67-1, (c) and (d) Mn-doped ZIF-67-1 (e) and (f) Ni-doped ZIF-67-1. 57

Figure 4.16. XRD pattern of ZIF-67 and Bimetallic ZIF-67s synthesized with NaOH. 58

Figure 4.17. SEM images of ZIF-67-2 at (a) 50000x and (b) 100000x zoom level. 59

Figure 4.18. XRD pattern of ZIF-67-2. 59

Figure 4.19. SEM images of Zn-doped ZIF-67-2 at (a) 50000x and (b) 100000x zoom level. 60

Figure 4.20. XRD pattern of Zn-doped ZIF-67-2. 60

Figure 4.21. XRD patterns of ZIF-67-2 and Zn-doped ZIF-67-2. 61

Figure 4.22. XRD patterns of ZIF-67-1 and ZIF-67-2. 62

Figure 4.23. SEM images of (a) and (b) MIL-88A-1, (c) and (d) MIL-88A-2. 63

Figure 4.24. XRD patterns of MIL-88A-1 and MIL-88A-2. 64

Figure 4.25. SEM images of Fe^{III}(TPA).DMF-1 at (a) 10000x and (b) 50000x zoom level. 65

Figure 4.26. XRD Pattern of Fe^{III}(TPA).DMF-1. 65

Figure 4.27. SEM images of Fe^{III}(TPA).DMF-2 at (a) 10000x and (b) 100000x zoom level. 66

Figure 4.28. XRD Pattern of Fe^{III}(TPA).DMF-2. 67

Figure 4.29. XRD Pattern of Fe^{III}(TPA).DMF-1 and Fe^{III}(TPA).DMF-2. 67

Figure 4.30. SEM images of Fe^{III}(NH_2-TPA).DMF. 68

Figure 4.31. XRD pattern of Fe^{III}(NH_2-TPA).DMF. 69

Figure 4.32. SEM images of CoII/ FeIII(NH2-TPA).DMF-1 at (a) 20000x and (b) 100000x zoom level. 69

Figure 4.33. XRD pattern of Co^{II}/ Fe^{III}(NH_2-TPA).DMF. 70

Figure 4.34. XRD patterns of Fe^{III}(NH_2-TPA).DMF (Fe-MIL-88B) and Co^{II}/ Fe^{III}(NH_2-TPA).DMF (Co/Fe-MIL-88B). 71

Figure 4.35. CV of coated SSM #1 in N_2 and O_2 purged PB medium at mV/s scan rate. 72

Figure 4.36. SEM images of the coated SSM, SSM #2, at (a) 400x, (b) 1600x,(c) 13000x and (d) 50000x zoom level. 73

Figure 4.37. CV plot of the coated SSM, SSM #2, in N_2 and O_2 purged PB medium at 100 mV/s scan rate. 74

Figure 4.38. CV plot of the coated SSM, SSM #3, in N_2 and O_2 purged PB medium at 50 mV/s scan rate. 74

Figure 4.39. CV plot of the coated SSM, SSM #4, in N_2 and O_2 purged PB medium at 100 mV/s scan rate. 75

Figure 4.40. CV plot of the coated SSM, SSM #4, in O_2 purged PB medium at 50 and 100 mV/s scan rates. 75

Figure 4.41. CV plot of the coated SSMs, SSM #3 and SSM #4, in oxygen purged PB medium at 100 mV/s scan rate. 76

Figure 4.42. CV plot of the coated SSM, SSM #2 and SSM #4, in oxygen purged PB medium at 100 mV/s scan rate. 76

Figure 4.43. SEM images of the coated SSM, SSM #5, at (a) 500x, (b) 1600x, (c) 4000x and (d) 8000x zoom level. 78

Figure 4.44. CV of the coated SSM, SSM #5, at 100 mV/s scan rate in N_2 and O_2 purged PB medium. 78

Figure 4.45. SEM images of the coated SSM, SSM #6, at (a) 400x, (b) 1500x, (c) 12000x and (d) 50000x zoom level. 79

Figure 4.46. CV of the coated SSM, SSM #6, at 100mV/s scan rate in N_2 and O_2 purged PB medium. 80

Figure 4.47. CV of the coated SSM, SSM #6, at 50 and 100 mV/s scan rates in PB medium. 80

Figure 4.48. SEM images of the coated SSM, SSM #7, at (a) 500x, (b) 1000x, (c) 8000x and (d) 60000x zoom level. 81

Figure 4.49. CV plot of the coated SSM, SSM #7, at 50mV/s scan rate in N_2 and O_2 purged PB medium. 81

Figure 4.50. CV of the coated SSMs, SSM #7 and SSM #2, at 100mV/s scan rate in N_2 and O_2 purged PB medium. 82

Figure 4.51. CV plot of the coated SSMs, SSM #6 and SSM #7, at 50mV/s scan rate in oxygen purged PB medium. 82

Figure 4.52. SEM images of the coated SSM, SSM #8, at (a) 500x, (b) 4000x, (c) 16000x and (d) 60000x zoom level. 83

Figure 4.53. CV plot of the coated SSM, SSM #8, at 50mV/s scan rate in N_2 and O_2 purged PB medium. 84

Figure 4.54. SEM image of the coated SSM, SSM #9, at (a) 400x, (b) 5000x, (c) 60000x and (d) 120000x zoom level. 84

Figure 4.55. CV plot of the coated SSM, SSM #9, at 50mV/s scan rate in N_2 and O_2 purged PB medium. 85

Figure 4.56. CV plot of the SSMs coated with Zn-MOF containing slurries at 50 mV/s scan rate. 86

Figure 4.57. SEM images of the coated SSM, SSM #10, (a) 750x, (b) 4000x, (c) 25000x and (d) 60000x zoom level. 86

Figure 4.58. CV plot of the coated SSM, SSM #10, at 50 mV/s scan rate in N_2 and O_2 purged PB medium. 87

Figure 4.59. SEM images of the coated SSM, SSM #11, at (a) 500x, (b) 1000x, (c) 4000x and (d) 7000x zoom level. 88

Figure 4.60. CV plot of the coated SSM, SSM #11, at 50 mV/s scan rate in N_2 and O_2 purged PB medium. 88

Figure 4.61. CV of the coated SSMs, SSM #11 and SSM #2, and bare SSM at 50mV/s in oxygen purged PB medium. 89

Figure 4.62. SEM images of the coated SSM, SSM #12, at (a) 600x, (b) 1000x, (c) 40000x and (d) 120000x zoom level. 89

Figure 4.63. CV plot of the coated SSM, SSM #12, at 100mV/s scan rate in N_2 and O_2 purged PB medium. 90

Figure 4.64. CV plot of SSMs coated with Co-MOFs at 50 mV/s scan rate. 91

Figure 4.65. SEM images of the coated SSM, SSM #13, (a) 500x, (b) 15000x, (c) 60000x and (d) 300000x zoom level. 91

Figure 4.66. CV plot of the coated SSM, SSM #13, at 50mV/s scan rate in PB medium. 92

Figure 4.67. CV plot of the coated SSMs, SSM #13 and SSM #2, at 50mV/s scan rate in oxygen purged PB medium. 93

Figure 4.68. SEM images of the coated SSM, SSM #14, at (a) 400x, (b) 16000x, (c) 60000x and (d) 120000x zoom level. 93

Figure 4.69. CV plot of the coated SSM, SSM #14, at 100 mV/s scan rate in N_2 and O_2 purged PB medium. 94

Figure 4.70. SEM images of the coated SSM, SSM #15, at (a) 1600x, (b) 10000x, (c) 50000x and (d) 100000x zoom level. 95

Figure 4.71. CV plot of the coated SSM, SSM #15, at 50mV/s scan rate in N_2 and O_2 purged PB medium. 95

Figure 4.72. CV plots of the SSMs containing Fe-MOFs at 50 mV/s scan rate. 96

Figure 4.73. Images of the SSM #5, SSM #6 and SSM #7, SSMs coated with Zn-MOFs, employed in MFC analysis. 97

Figure 4.74. Current density vs. potential plot obtained from LSV of MFC with SSM #5. 97

Figure 4.75. Nyquist plot of the MFC with SSM #5 cathode. 98

Figure 4.76. SEM images of SSM #5 (a) and (b) before MFC, (c) and (d) after MFC tests. 98

Figure 4.77. Current density vs. potential plot obtained from LSV of MFC with SSM #6. 99

Figure 4.78. Nyquist plot of the MFC with SSM #6 cathode. 99

Figure 4.79. SEM images of SSM #6 before (a), (b), (c) and after (d), (e), (f) MFC tests. 100

Figure 4.80. Current density vs. potential plot obtained from LSV of MFC with SSM #7. 100

Figure 4.81. Nyquist plot of the MFC with SSM#7 cathode. 101

Figure 4.82. SEM images of the SSM #7 (a) and (b) before, (c) and (d) after MFC tests. 101

Figure 4.83. Image of the SSM #10, SSM coated with Co-MOF, employed in MFC analysis. 102

Figure 4.84. Current density vs. potential plot obtained from LSV of the MFC with SSM #10. 102

Figure 4.85. Nyquist plot MFC with SSM #10 cathode. 103

Figure 4.86. SEM images of SSM #10 (a) and (b) before, (c) and (d) after MFC tests. 103

Figure 4.87. Image of the SSM #13, SSM coated with Fe-MOF, employed in MFC analysis. 104

Figure 4.88. Current density vs. potential curve obtained from LSV of the MFC with SSM #13. 104

Figure 4.89. Nyquist plot of the MFC with SSM #13 cathode. 105

Figure 4.90. SEM images of SSM #9 (a) and (b) before, (c) and (d) after MFC tests. .. 105

Figure 4.91. Current density vs. potential plot of MFCs with various cathodes. 106

Figure 4.92. Nyquist plots of MFCs with various cathodes. 107

Figure 4.93. Current density vs. potential plots of the coated SSMs obtained from CV. 107

Figure 4.94. SEM images of the anode, SSM #2, (a) and (b) before, (c) and (d) after MFC tests. 108

Figure A.1. Copyright notice for Figure 1.6. Reproduced from Ref. 82 with permission from the Royal Society of Chemistry. 133

Figure A.2. Copyright notices for Figure 1.7. 133

Figure A.3. Copyright notices for Figure 1.7. 134

Figure A.4. Copyright notices for Figure 1.7. 134

LIST OF TABLES

Table 3.1. Properties of SSM coated without binder, SSM #1. 35

Table 3.2. Properties of SSMs coated with slurries prepared with PVA as binder. 36

Table 3.3. Properties of the SSMs coated with MOFs and MOF-carbon composites. 39

Table 4.1. Conductivities of SSM before and after coating with binder- free carbon slurry. 71

Table 4.2. Conductivities of SSMs before and after coating with carbon and PVA binder containing slurries. 72

Table 4.3. Conductivities of the SSMs before and after coating with MOF-containing slurries. 77

LIST OF ACRONYMS/ABBREVIATIONS

2D	2-Dimensional
2-MeIm	2-Methylimidazole
BDC	1,4-Benzenedicarboxylate
BET	Brunauer-Emmett-Teller
BMOF	Bimetallic Metal Organic Framework
BTC	1,3,5-Benzenetricarboxylate
CB	Carbon Black
CF	Carbon Felt
CNT	Carbon Nanotube
CV	Cyclic Voltammetry
DET	Direct Electron Transfer
DMF	N,N-Dimethylformamide
DMSO	Dimethyl Sulfoxide
DUT	Dresden University of Technology
EC	Ethyl Cellulose
EDX	Energy Dispersive X-Ray Analysis
EET	Extracellular Electron Transfer
EIS	Electrochemical Impedance Spectroscopy
EtOH	Ethanol
FA	Fumaric Acid
FC	Fuel Cell

GO	Graphene Oxide
H_2BDC	Benzene-1,4-dicarboxylic acid
HER	Hydrogen Evolution Reaction
HHTP	2,3,6,7,10,11-hexahydroxytriphenylene
HKUST	Hong Kong University of Science and Technology
H_2O_2	Hydrogen Peroxide
H_3BTC	1,3,5-Benzenetricarboxylic acid
LSV	Linear Sweep Voltammetry
MeOH	Methanol
MET	Mediated Electron Transfer
MFC	Microbial Fuel Cell
MIL	Material Institute Lavoisier
MOF	Metal Organic Framework
NaOH	Sodium Hydroxide
NH_2-TPA	2-Aminoterephthalic Acid
OCP	Open Circuit Potential
OCV	Open Circuit Voltage
OER	Oxygen Evolution Reaction
ORR	Oxygen Reduction Reaction
Ox	Oxalic Acid
PB	Phosphate Buffer
PDMS	Polydimethylsiloxane
PEM	Proton Exchange Membrane
PTFE	Polytetrafluoroethylene

PVA	Polyvinyl Alcohol
RT	Room Temperature
SBU	Secondary Building Unit
SDA	Structure Directing Agent
SEM	Scanning Electron Microscope
SS	Stainless-Steel
TEA	Terminal Electron Acceptor
TPA	Terephthalic Acid
UiO	Universitetet i Oslo
US	Ultrasound
w %	Weight Percent
XRD	X-Ray Diffraction Analysis
ZIF	Zeolitic Imidazolate Framework

λ	Wavelength
p	Resistivity
Ω	Resistance (ohm)
σ	Conductivity

1. INTRODUCTION

1.1. Microbial Fuel Cells (MFCs)

The rapid increase in the global energy demand with the increasing population, developing technologies, rapid depletion of natural energy sources and fossil fuels, the increase in environmental pollution and the impact of the climate crisis have caused the researchers to be directed to renewable alternative energy sources. Alternative renewable energy generation devices in the areas such as solar, geothermal, wind and biomass gained vast amount of interest in research and their applications demonstrated as useful alternatives to fossil fuel-based energy generation that provides for most of the energy need for so long. Another promising alternative energy generation technology is fuel cells (FCs) which is invented by William Grove and can utilize various sources such as hydrogen, methanol, wastes, etc. In recent years, studies were held for the development of Microbial Fuel Cells, a class of bio-electrochemical fuel cells, as an efficient, low-cost, environmentally friendly, clean energy generation technology. First microbial fuel cell is built by Michael C. Potter in 1911, showing a current flow between electrodes that are emerged in a bacterial culture medium [1].

1.1.1. Working Principles

Microbial fuel cells are powerful alternative energy sources in fuel cell technologies. They work similarly as conventional fuel cells. However, they utilize the metabolic activities of microorganisms through which the chemical energy stored in organic/inorganic substrates is directly converted into electrical energy. Catalytic reactions that take place within the bacteria by using biodegradable substrates as fuel, the MFC can simultaneously generates electricity even while treating wastewater as well [2].

A simple MFC system that is commonly used in research consists of anode and cathode chambers, a proton exchange membrane separating these compartments while allowing H^+ transfer between electrodes (Figure 1.1). Electrons, protons, and CO_2 are released when microorganisms growing around the anode electrode surface oxidize the substrate/fuel through its metabolic activities. Generated electrons are transferred to the anode electrode, then reach the cathode electrode through external circuit via an external resistor connected through the electrodes and protons that are generated in the anode compartment transfer through the proton exchange membrane to the cathode compartment. In MFCs, air or dissolved oxygen is used as the terminal electron acceptor (TEA) in the cathode compartment usually due to their high reduction performance and abundancy. The oxygen reduction reaction occurs when protons reach to the cathode compartment and combine with oxygen. The potential is generated by the concentration differences of the solutions at the anode and cathode. Electrons formed from the metabolic activities of the bacteria in the anode compartment reach the cathode electrode from the external circuit, combining with the TEA and protons in the cathode compartment to complete the circuit and produce electricity [3].

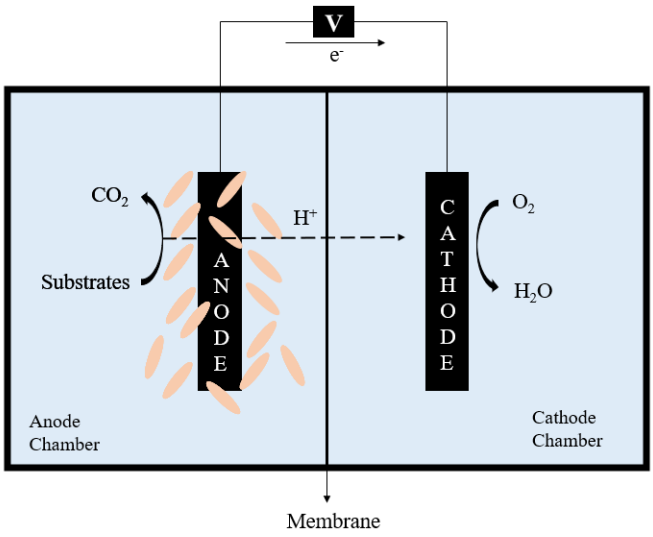


Figure 1.1. Schematic illustration of a two-chamber microbial fuel cell and its working mechanism.

Electrochemical reactions that take place at anode and cathode can be summarized as followed for a representative MFC utilizing acetate as substrate/fuel and oxygen as final electron acceptor [4].

At the anode, oxidation reaction taking place when electrochemically active bacteria use acetate as substrate can be expressed as

$$CH_3COO^- + 2H_2O \rightarrow 2CO_2 + 7H^+ + 8e^-, \quad (1.1)$$

and the oxygen reduction reaction taking place on the cathode electrode can be expressed as

$$O_2 + 4H^+ + 4e^- \rightarrow 2H_2O. \quad (1.2)$$

In the MFC anode compartment, as the substrate is being oxidized it is renewed intermittently or continuously. Most microbial fuel cells operate as a closed system so that the anode chamber is anaerobic, depending on the bacteria species being used. It is necessary to provide this environment for the growth of anaerobic bacteria such as G. Sulfurreducens and for the formation of biofilms [5]. In cases where the anode compartment is aerobic, the oxygen content becomes high and due to its electronegativity, electrons produced by the bacteria are taken up by the oxygen instead of the mediator or anode electrode which hinder the electricity production highly [3].

Microorganisms used in MFC can transfer the electrons, that are released because of oxidation of the substrate, to the anode electrode in two ways as direct and indirect electron transfer (Figure 1.2). Direct electron transfer requires a physical connection between the bacterial cell and the electrode surface through conductive pili (nanowires) and/or redox-active proteins. Indirect electron transfer does not require any physical contact but proceeds via electron shuttling molecules, mediators. Electron transfer via mediators is often utilized in MFC systems in which the microbial species used have a non-conductive lipid membrane and a peptidoglycan layer. Bacteria with these properties cannot transfer their electrons directly to the anode electrode. These redox mediators are classified as exogeneous if they are added to the MFC system manually or endogenous if they are produced by the bacteria itself. By producing secondary metabolites, also known as electron shuttles, which can function as endogenous redox mediators, bacteria are able to produce energy. These electron shuttles are organic molecules with low molecular weight that can both be oxidized and

reduced [2,6]. Examples to endogenous redox mediators are flavins as pyocyanin and riboflavin, phenazines and quinones. Mediators that can easily enter the cell are reduced by taking electrons from electron carriers involved in the cell and electron transport systems first, then they are oxidized by leaving the cell and giving these electrons to the anode electrode. Some of the exogeneous redox mediators used in MFC research are thionine, methyl viologen, methylene blue and humic acids [2,6].

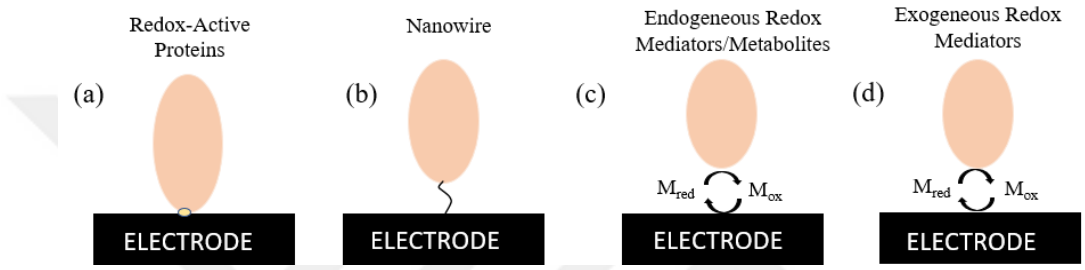


Figure 1.2. Schematic illustration of electron transfer mechanisms between microorganisms and the electrode.

1.1.2. Factors Affecting MFC Performance

Low power outputs and high costs of MFCs produced so far are the biggest obstacle for the industrial applications of microbial fuel cells beyond the research level. There are many factors that can be improved to increase the performance and reduce production and operation costs in MFC systems. Those factors are mainly MFC configuration, membrane performance, bacterial metabolism, biofilm formation, electron transfer mechanisms, anode and cathode electrode materials, composition of anolyte/catholyte solutions and reduction reaction efficiency in cathode.

MFC Configuration: MFC performance can be improved by changing the configuration since power generation is highly dependent on the size of electrode and membrane, reactor volume and distance between electrodes. Briefly, MFC configurations can be divided into single-chamber and two-chamber MFCs (Figure 1.3). Single-chamber MFC systems have

no separate cathode compartment. Anode and air-cathode electrodes are separated by a gas diffusion layer and/or a proton exchange membrane [3]. Cathode electrode is in direct contact with the air and protons released because of the catalytic activity of microorganisms are transferred from the anolyte solution to this porous air cathode. The circuit is completed when the generated electrons reach the porous air cathode over a conductive wire, combine with the protons and final electron acceptor and reduction reaction take place [7]. On the other hand, two-chamber MFC systems consist of anode and cathode compartments separated by a proton exchange membrane generally which can be seen in Figure 1.3. It is one of the most widely used MFC configurations. The proton transfer is enhanced, mixing of anode and cathode solutions and back diffusion of oxygen to anode chamber is prevented due to presence of proton exchange membrane. Air-cathodes can be utilized in two-chamber MFCs as well [8].

For simple, common two-chamber MFCs, the cathode chamber contains aqueous solution, water sparged with air. Increased concentrations of dissolved oxygen and using pure oxygen to sparge the water in cathode chamber showed improved performance of the MFC [9]. Instead of using oxygen as terminal electron acceptor (TEA), soluble catholytes as ferricyanide or permanganate catholytes can be used as well. In a study, improved performance of a two-chamber MFC with carbon paper anode and carbon cloth cathode was demonstrated when soluble catholytes are used as TEA. Power density of 116 mW/m^2 was obtained with permanganate as TEA, which was 11.3-fold higher than the one with dissolved oxygen [10].

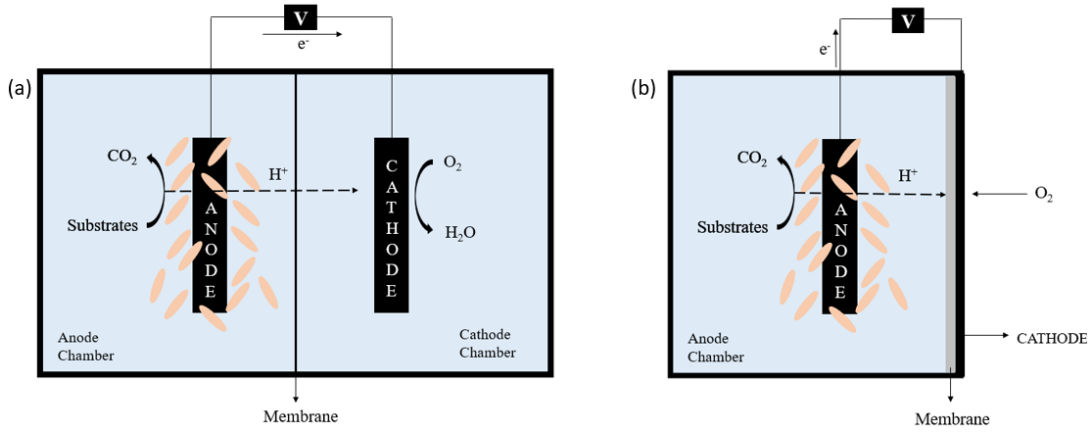


Figure 1.3. Schematic representations of (a) two-chamber and (b) single-chamber MFCs.

MFC systems can be operated in batch mode with chemically defined solutions containing fuels such as acetate or glucose or in continuous flow mode to optimize the power output [11,12]. There are various architectural designs for both two-chamber and single-chamber microbial fuel cells demonstrated in MFC research such as H-type bottle reactors, cubic reactors, tubular packed bed reactors and stacked MFCs [3].

Membrane: In MFCs, membrane is responsible for the ion transfer and separation of anode-cathode chambers. Different types of membranes being used in MFC technologies as anion exchange membranes, ultrafiltration membranes but most widely employed one is the proton exchange membranes (PEM). PEM prevents the diffusion of gases such as CO_2 and O_2 from the compartments they belong to the other compartment, and it transfers the protons formed in the anode chamber to the cathode. While selecting the proper membrane, internal resistance, substrate loss, biofouling, oxygen diffusion, thermal and mechanical stability are important parameters for the performance of the cell [13]. Nafion is one of the most utilized proton exchange membranes in MFCs due to its high efficiency. Nafion consists of ether side chains and hydrophilic sulfonic acid groups attached to the hydrophobic polytetrafluoroethylene (PTFE) backbone chain [14]. It has high proton conductivity due to its sulfonic acid groups and is chemically inert in both oxidizing and reducing atmospheres due to the hydrophobic PTFE backbone chain [6]. Biggest disadvantage in MFC systems without a proton exchange membrane the loss of substrate due to aerobic oxidation of

bacteria in the anode compartment with increasing oxygen levels due to back diffusion of oxygen which highly decrease coulombic efficiency. In a study with a glucose fed single chamber MFC, it was demonstrated that coulombic efficiency is 40-55% in the presence of Nafion-117 whereas it is 9-12% in the absence of PEM which is most likely because of increased oxygen diffusion [7].

Microorganisms and Substrates: Electricity is produced in MFC systems directly by the electrons that are released when microorganisms oxidize the substrate, reach the anode and to the cathode via the external circuit and combine with the final electron acceptor. For this reason, the performance of MFC systems depends highly on the catalytic properties and behaviour of the bacteria used [15]. Many different microorganisms have been used in studies on electricity generation and/or wastewater treatment with MFCs. Some microorganisms commonly used in MFC systems can be listed as Escherichia Coli, Shewanella Oneidensis, Shewanella Loihica, Shewanella Putrefaciens, Geobacter Sulfurreducens, and Rhodoferax Ferrireducens. E. Coli, gram-negative and selectively anaerobic bacteria, is widely used in MFC research because it can be easily found, reproduces, grows and is resilient. E. coli can ferment many types of sugar and it does not necessarily require a mediator for extracellular electron transfer (EET) since it can excrete its own electron shuttling molecules as reported [16,17]. Schwanella which is a gram-negative, selective anaerobic bacteria family that is also widely used in MFC systems. Schwanella has many species in nature that can decompose various organic compounds and use many different electron acceptors for growth under anaerobic conditions [16]. Besides various operational parameters affecting MFC performance, the efficiency of extracellular electron transfer mechanism of microorganisms and biofilm formation have an important effect on power generation. For this reason, biofilm engineering, genetic and/or chemical modifications to microorganisms are being studied to improve MFC performance [18,19].

Anode: Anode is one of the key elements to improve the MFC performance due to its high impact on electricity generation and system efficiency. Since the structure and composition of the anode electrode has effects on microbial adhesion and biofilm formation, electron transfer efficiency, electrode resistance and electrode surface reactions, selection of

the electrode material is very important for electricity generation and organic matter removal performance of MFC systems. Anode electrode should have high electrical conductivity, chemical stability, low resistance, high specific surface area, surface roughness/hardness, porosity, biocompatibility, appropriate mechanical durability, anti-corrosion, easy production, and cost efficiency for enhanced fuel cell performance. Some of the commonly used carbon-based electrodes as MFC anodes are graphite [20,21], reticulated vitreous carbon (RVC) [22], graphite rods [23], graphite felts [24], carbon cloths [25], carbon meshes [26], carbon nanotubes (CNTs) [27], carbon foam [28], carbon paper [2], and graphene [29]. Enhanced fuel cell performance can be achieved through modifications on the anode electrode via changing its physical and chemical properties as conductivity, hydrophilicity, biocompatibility, surface area and electrocatalytic activity through coating slurries with different compositions [30,31]. Modified electrodes can be obtained by implementing nanomaterials, metals, metal oxides and composite materials [32–34]. Generally, surfaces of bacterial cells have a hydrophilic nature, and they are negatively charged. That is why anodes containing hydrophilic parts and positive charges may increase biofilm formation of electroactive microorganisms that can lead to improved MFC performance [35]. Improved power output of an E. Coli-based single chamber microbial fuel cell using PVA as anode binder material instead of PTFE, that is one of the most used polymer binders in electrode coatings was demonstrated in a study where anode slurries containing CNTs, that provide more electrically conductive network, PVA or PTFE binder solutions were coated on carbon felt (CF) anode electrode. Effect of binder amount was examined, and highest power outputs were obtained from 10% PVA and %5 PTFE. MFCs containing electrodes with 10% PVA binder content resulted in a maximum power output of 1.631 W m^{-2}, 97.9% greater than the one using 5% PTFE due to PVA's hydrophilic nature and enhanced interaction of coated anode and bacteria [36]. In another study, mixed transition metal oxide, $MnCo_2O_4$, was directly grown on CF via hydrothermal synthesis route without any binder which generated a rough anode with higher surface area resulting in enhanced microbial adhesion. Power density obtained from the two chamber MFCs with $MnCo_2O_4$ coated CF anode was 945 mW/m^{-2}, 3.8 times higher than cell with uncoated CF anode due to $MnCo_2O_4$ coated CF anode's lower charge transfer resistance, higher surface area and higher electrochemically active sites resulted by mixed metals variable oxidation states [37].

As an alternative to carbon-based electrodes, metal-based materials as electrodes are utilized in research too [38-40]. One study showed that when metals as gold, silver, copper,

nickel and stainless-steel (SS) are used as anode materials, electrochemically active biofilms were formed. Additionally, silver and copper showed comparable current densities to graphite and among all the metals highest performance obtained when copper was used as the electrode [38]. Stainless-steel materials are especially highly used in MFC technologies due to their electrically conductive nature, mechanical properties, corrosion resistance and cost efficiency [39]. Higher current density is reported when stainless-steel anode is utilized compared to flat graphite with same experimental conditions [40]. More studies are being conducted to develop advanced electrode materials with modifications on SS. In a study, surface modifications as heat treatment, carbon coating, conductive polymer (PANI) coating and hydrophilization on SS demonstrated better performance than unmodified bare SS anodes [41]. Carbon-based coatings on SS electrodes showed increased microbial adhesion and improved electron transfer efficiency between the microorganism and the anode, demonstrating fuel cell examples with good performance [42].

Cathode: The cathode electrode is another component of a MFC that determine both the cost and performance. In MFCs, the terminal electron acceptor is generally oxygen due to its abundance and high reduction potential. Efficient oxygen reduction reaction that takes place on cathode is a crucial parameter for improved performance of an MFC. Most of the materials used as anode electrode can be used as current collector for the cathode as well. In addition to high electrical conductivity, high specific surface area, stability, durability, and cost-effectiveness, high ionic conductivity and redox potential are required features for a cathode electrode. Electrochemical reduction of oxygen can mainly proceed through either in direct four-electron pathway or a two-electron pathway including formation of intermediates as hydrogen peroxide. The exact mechanism highly depends on the cathode material, electrolyte and catalyst used. Two different ORR mechanisms in general, demonstrated in Figure 1.4. Partial reduction of O_2 proceed with two-electron ORR pathway including adsorption of O_2 on the surface of the catalyst in which the O=O bond does not break. $2H^+$ addition to adsorbed O_2 lead to hydrogen peroxide formation which can either form two water molecules with further reduction or dissociate from the catalyst surface to form free hydrogen peroxide [43]. Hydrogen peroxide that is formed via two-electron ORR pathway can lead to high overpotential and facilitate fuel cell component degradation. To overcome these shortcomings and obtain an efficient ORR, catalysts that follow a four-

electron pathway in which O_2 is directly reduced to H_2O is desired [44,45]. In case of full reduction, ORR proceed with more efficient four-electron pathway without production of hydrogen peroxide [46,47].

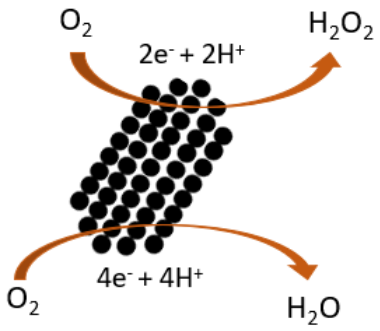


Figure 1.4. Schematic representation of ORR with 2 e^- and 4 e^- pathway.

The performance of the cell is reported to be decreased due to mainly three losses as activation, mass transfer and ohmic losses [48]. Activation loss is the loss of potential due to activation of the reactants. The rate of reduction reaction taking place on the cathode surface is hindered due to reaction activation energy barrier [30] Insufficient mass transfer that may result in product accumulation, insufficient proton removal and oxygen supply and depletion of reactants also affects the reaction rates and performance of fuel cell and referred as mass transfer losses [49]. On the other hand, ohmic losses caused by the resistance to flow of electrons through electrodes, flow of protons through the membrane and the resistances of electrolyte solutions results in voltage losses. Effects of those limitations for MFC performance can be minimized by using cathode catalysts [50]. In a study, power densities when catalysts were employed on the cathodes were nearly 4 times more than carbon electrode without catalyst [51]. The most used cathode catalysts in studies are platinum and platinum- based materials [52]. However, high costs as a precious metal, being prone to biofouling and pH sensitivity limits is application in MFC technology leading to the search of cheaper, biofouling resistant and higher catalytic activity materials that will increase the cost-effectiveness, ORR rate, efficiency, and power output of MFC.

In that respect, carbon-based or metal-based current collectors are modified, often coated with catalysts [53], activated carbon [54], graphite [55], graphene, carbon cloth [10], their composites with other carbon materials[56,57], metals, metal oxides, polymers [58,59] and metal organic framework based materials [60,61].

Biological cathodes (bio-cathodes) have been also studied for enhanced MFC performance. Microorganisms that are utilized in cathode compartment are used as biocatalysts to accept electrons from the cathode electrode and assist the reduction reaction. Oxygen, inorganic salts, transition metal compounds, carbon dioxide any many others can be used as the final electron acceptor in bio-cathode microbial fuel cells [62]. In a study with bio-cathodes that are utilized in a two chamber MFC with oxygen as TEA in the cathode chamber, bio-cathode was fed using the effluent of an acetate-fed anode compartment. Formation of a cathodic biofilm demonstrated a fourfold increase of the current output compared to abiotic MFC with graphite cathode [63]. Even tough, the reduction reaction is catalysed by the microorganisms, there is still need for advanced cathode electrode materials that will enhance the formation of biofilm and efficient electron transport.

1.2. Metal Organic Frameworks (MOFs)

Metal organic frameworks (MOFs) are porous coordination polymers that are constructed from organic linkers and metal nodes. Historically, it is recognized that the development of MOFs is based on the fields of coordination and solid-state/zeolite chemistry. Organic linkers acting as “strut” and metal cations, or metal clusters known as secondary building units (SBUs) acting as “joints” result in crystalline materials with permanent porosity [64,65,66] (Figure 1.5).

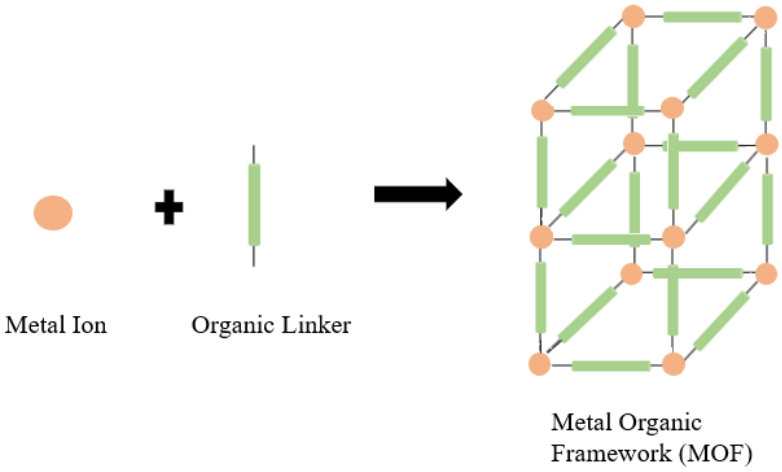


Figure 1.5. Schematic representation of MOF formation.

Nomenclature of MOFs differ with respect to various conditions. They can be named with respect to the metal used in the synthesis (Zn-MOF, Fe-MOF, Cu-MOF) or the location where the frameworks are produced (MIL; Material Institut Lavoisier, DUT; Dresden University of Technology, UiO; Universitetet I Oslo), or structural similarities (ZIF; Zeolitic Imidazolate Framework). The numbers following the MOF's name are assigned based on the order of synthesis regarding that specific MOF (MIL-53, MIL-88, MIL-101) [67].

Porous structures can be tailored in terms of pore size by selection of metal clusters with different sizes and organic ligands with different lengths that will connect secondary building units. Besides adjustable porous structure of MOFs, they have unique characteristics as high surface area, flexibility, crystallinity, structural diversity, and functionality due to adjustable chemical and structural composition [65].

DUT-60, a crystalline MOF, reported with very high porosity, 5.02 cm^3g^{-1}, and specific surface area of 7839 m^2g^{-1} [68] resulted in great interest in the research of MOFs and applications in various areas such as gas adsorption and storage [69], gas separation [70], catalysis [71,72], drug delivery [73], luminescence [74,75], sensors [76], batteries [77], supercapacitors [78], fuel cells [61,79] and many more throughout the years.

Further improvements on unique characteristics of MOFs are obtained by incorporation of a second metal node into the system generating bi-metallic MOFs (BMOFs). Doping a secondary metal to the framework creates a synergistic effect between the metals, favours electronic coupling between metal nodes, improves electroactive redox reactions and the electrical conductivity [80]. Incorporated secondary metal can be in the same SBU with the primary metal and these SBU structure can be present throughout the whole MOF for generally metals with similar ionic radius or only same metals are present in each SBU and those two different SBUs are mixed in the whole MOF structure (Figure 1.6). Unfortunately, in the overall crystal structure of a BMOF, specific orientation of metals in the SBUs are not known for most of the reported BMOFs [80]. Also, there is a possibility that each metal may form separate MOFs without any connection to the other SBUs which creates a challenge for synthesis and applications of BMOFs [81].

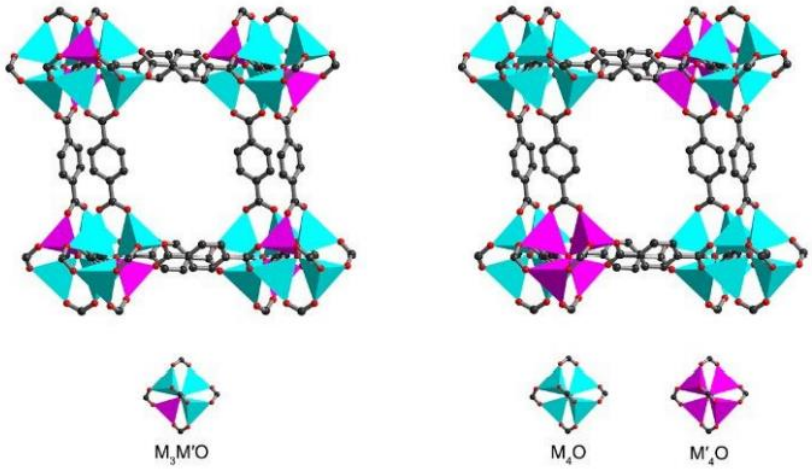


Figure 1.6. Illustration of SBUs and arrangements of metals in BMOFs [82].

MOFs often lack stability in water, aqueous medias. By incorporation of a second metal, their stability can be improved [83]. In a study, Zeolitic Imidazolate frameworks (ZIFs) which are sodalite-type MOFs with zeolite like morphology was synthesized in mild conditions from Zn and Co metal ions and 2-methylimidazole (2-MeIm) as organic linker. Besides single metal MOFs, ZIF-8 and ZIF-67, their mixed metal version was also produced by a single step synthesis. BMOF, Zn/Co-ZIF, demonstrated to have different physical properties as surface area, porosity and improved stability compared to single metal ZIFs

[81]. Besides enhanced hydrolytic stability, improved catalytic activities of MOFs can be achieved via doping a second metal to its structure as well [84–86]. For example, Pd doped-ZIF-67 was obtained via Pd metal incorporation into ZIF-67 that was formed via ultrasound assisted synthesis. Obtained BMOF showed enhanced catalytic activity towards the reduction of aromatic nitro pollutants [87]. BMOFs can be used as powerful electrocatalysts due to their improved ORR/OER/HER efficiencies [88,89]. A synthesized bimetallic 2D layered hexagonal Co_xNi_y-CATs, that are formed from 2,3,6,7,10,11-hexahydroxytriphenylene (HHTP) organic linker, Co and Ni metal ions, demonstrated 4^- electron transfer pathway ORR and improved ORR performance compared to MOFs with singe metal, Co-CAT and Ni-CAT [90].

1.2.1. Design and Synthesis of MOFs

Design and the synthesis method can introduce different properties to MOFs as adjusted pore size, electrical and magnetic properties, catalytic characteristics by selection of specific metal node and organic ligand. While designing the desired MOF, it is important that fundamental characteristics as number of binding sites and available connection geometry of the metal ion/cluster are considered. Transition metals that are commonly utilized in metal organic framework synthesis with their partially filled d orbitals have various oxidation states which lead them to exhibit different coordination geometries as trigonal planar, pyramidal, square planar, tetrahedral, square pyramidal, trigonal bipyramidal and octahedral [91]. For example, when terephthalic acid with its rod-like linear connectivity geometry was used as organic linker, different metal ions/clusters with different geometries resulted in various morphologies (Figure 1.7) [92].

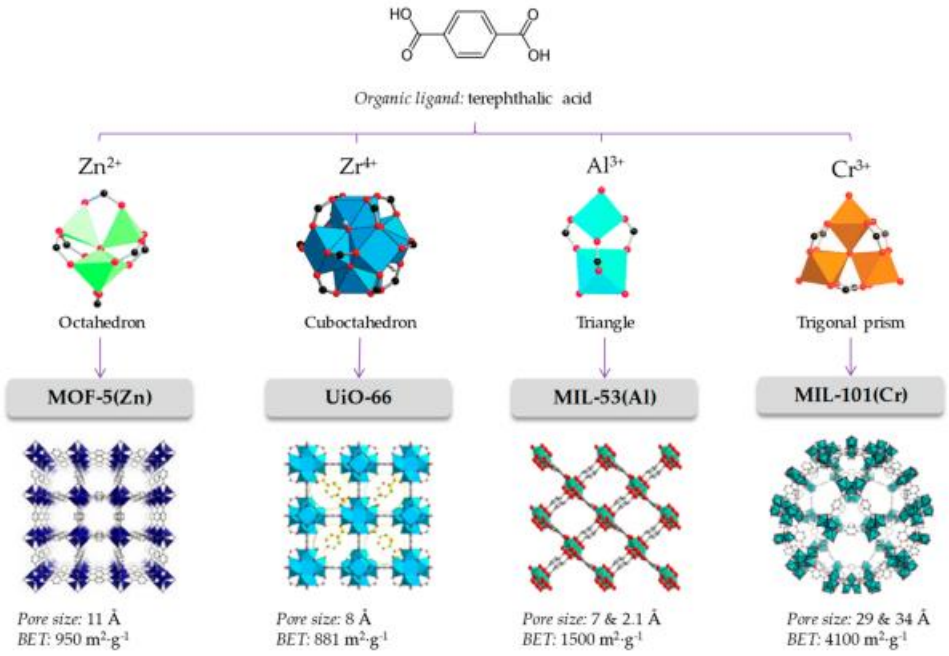


Figure 1.7. Effect of metal ions/clusters with different connection geometry on produced MOF [92].

Also, sites on the ligand that can be linked with metal centres and their modes of coordination is highly important [93]. There are various organic ligands being utilized that lead to MOFs with different features as flexible or rigid MOFs or MOFs with enhanced catalytic activity, adjusted porous structure and conductivity. Some of the highly used organic ligands in MOF synthesis belong to carboxylic acids and imidazolates.

The nature of the MOFs as particle size, morphology and size distribution depends on parameters such as temperature, reaction time, pressure, pH, solvent, linker substituent and metal ion concentration and type. Even though identical reactive mixture (metal source, organic ligand, and solvent) is used during the formation of MOFs, structure may differ due to different synthesis procedures, reaction times, pressures, temperatures etc.

There are different types of reported synthetic approaches for producing MOFs such as room temperature (RT) synthesis, solvothermal/hydrothermal synthesis, microwave synthesis, sonochemical synthesis and electrochemical synthesis method (Figure 1.8). They all have distinctive advantageous and disadvantageous properties in terms of synthesizing the targeted MOFs [66].

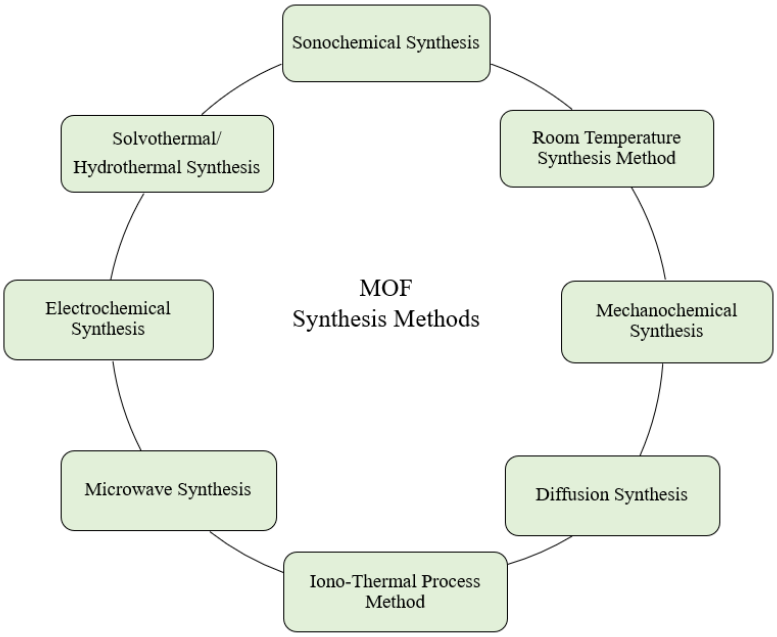


Figure 1.8. Commonly used synthesis methods of MOFs.

Room Temperature Synthesis Method: Self-assembly of MOF units from soluble precursors as organic ligands, metal salts and other raw materials as modulators are mixed in solvent at RT for a certain time. Formation of the MOFs takes place in ambient conditions without externally heating the reaction mixture [94]. Then, centrifugation and/or filtration is being used to separate the product and solvent is evaporated to obtain the desired MOF [95]. This method is very energy efficient since external energy supply is not required in most of the synthesis route. Also, low temperature-induced defects (LTID) can be introduced easily using this technique [96].

Solvothermal/Hydrothermal Synthesis Method: Solvothermal synthesis for MOFs is one of the most used methods that is employing electrical heating. Metal salts and organic ligands that are dissolved in the solvent are placed in a closed reaction vessel, commonly a stainless-steel autoclave for MOF crystals synthesis [97]. In these sealed high-temperature reactor under autogenous pressure and set temperature, crystallization may take hours, days or weeks which might became very time consuming. When reaction ends and mixture cools down to RT, the product is washed to remove impurities and unreacted parts before vacuum drying [65,66].

Microwave Synthesis Method: Microwave assisted synthesis is a rapid procedure which has been also used to produce small metal and oxide nanoparticles via heating the solution with microwaves [65,98]. Besides being rapid, microwave synthesis is a useful method to follow for obtaining phase purity, high yield, and controlled particle size. However, it also has its own limitations in terms of reproducibility since creating same conditions with different instruments might be challenging [99].

Electrochemical Synthesis Method: Electrochemical synthesis of MOFs requires an anode and a cathode which are placed in an electrochemical medium containing organic ligand and metal salt and attached to a power supply [66]. Since the metal ions are produced by anodic dissolution due to anodic oxidation of metal salts, this method is reported to be more rapid and cost-efficient than most employed solvothermal method [100] and it is being used for industrial scale synthesis that require higher solid content [65].

Mechanochemical Synthesis Method: In mechanochemical synthesis method, with the aid of mechanical forces molecule-surface collisions take place that leads to formation of MOFs. Reactions can take place at RT without need of external heat and in a solvent-free environment which is useful to eliminate the use of hazardous organic solvents [101].

Sonochemical Synthesis Method: Sonochemical synthesis uses ultrasound power which provides an energy efficient, rapid, simple route for MOF production. Formation, growth, and collapse of bubbles (acoustic cavitation) cause extreme local heating, high pressure that enables rapid release of energy with high heating and cooling rates above 1010K/s [102]. By ultrasonication, the time taking for MOF formation is reduced due to improved, accelerated dissolution of precursor materials [65] and formation of nucleation centres by collapsing of the bubbles, cavities compared to other methods [103]. Besides its advantages as being environmentally friendly, rapid and energy efficient, limitation to its applications result from the need of control over the temperature since increase of temperature occur in the reaction mixture and this increase can be varied in amount with the equipment used [104].

Diffusion Synthesis Method: Diffusion method is classified into three as liquid phase diffusion, gas phase diffusion and gel diffusion. All of them works by bringing the different species into interaction slowly. In liquid phase diffusion, metal ion precursor and organic ligand are dissolved in immiscible solvents [105] whereas in gas phase diffusion volatile organic solvent is used [106]. In the gel phase diffusion method, MOF crystals are formed from organic ligand and metal precursor that are diffused in a gel substance [48,66].

Iono-Thermal Process Method: Ionothermal synthesis offers a simple method for production of MOFs. Metal ion precursor, organic ligand and the ionic liquid or deep eutectic solvents, that can act as both solvent and structure directing agents (SDA), get mixed and incubated at high temperature for some time. Ionic liquids are defined as liquids composed of ions that are fluid below or around 100°C [107] and deep eutectic solvents are composed of two or more compounds and result in low melting point than its constituent compounds [104]. This synthesis method offers a wide range of solvents whose effect on MOF formation, morphology can be studied [108].

Synthesis of BMOFs can take place as one-step in situ synthesis where two metal precursors and organic ligand are coupled in single step in one of the above-mentioned synthesis methods. Whereas with post-synthesis modification of MOFs, firstly MOF is

synthesized with one of the common methods then as a second step, secondary metal is added to replace some portion of the primary metal [80]. Proportions of the metals can be adjusted and controlled so that, physicochemical properties of BMOFs can be tailored [82].

1.2.2. Factors Affecting MOF Synthesis

Crystallization, growth, structure, morphology, and topology of MOFs depend on various factors of synthesis condition besides the building blocks, metal, and organic linker. Some of these factors are pH, temperature and solvent of the synthetic medium, reactant molar ratios and modulators if present [109].

Solvent: Except mechanochemical synthesis method, most of the methods require presence of a properly selected solvent due to poor solubilities of organic linkers [48]. The solvent selection is one of the important parameters in the synthesis of MOFs since solvents can be involved in the coordination with metal ions, act as a medium for reaction or a guest molecule that is behaving like SDA [109]. Effect of different solvents on the formed structure of MOFs was investigated in a study that utilized $Cr^{3+,}$ H_3BTC and solvent in synthesis. When water was used as the solvent alone, Cr-MIL-100 with a pure phase was obtained. On the other hand, when water-methanol mixture with small amounts of methanol used, Cr-MIL100 and Cr-MIL-96 coexisted in the product formed. Higher amounts of methanol in the solvent mixture led to formation of pure phase Cr-MIL-96, whereas in the absence of water Cr-MIL-96 exhibited a poor crystallinity [110].

pH: Crystallization and growth of MOFs are highly influenced by the acidity/basicity of the reaction media. Usually, MOF synthesis are carried out in low pH values since the nature of metal ion clusters, linkers and modulators if used is acidic. However, at very low pH values organic linkers as 4,4'-bipy and imidazolates, cannot coordinate with metal ions due to protonation and then organic linkers act as limiting reagents. Also, low pH values can influence the extend of deprotonation of carboxylate type ligands which may lead to lower the yield and increased reaction times [111].

Deprotonating agents, pH modulators such as trimethylamine and sodium hydroxide are used to enhance and fasten deprotonation of organic linkers as carboxylates in MOF synthesis [112,113].

Modulators/Additives: Modulators, that are inherited from modulated coordination synthesis techniques can be used in MOF synthesis primarily to cap the growth of MOF crystals. Modulators with similar functionalities with the linkers used to modulate, adjust the coordination between metal ion and linker so that crystal growth, size and morphology of the framework can be controlled [114]. Also, they are employed in MOF synthesis to enhance crystallinity and stability, generate defects, control particle size, or produce specific pure phases of MOFs [115]. Synergistic effect of pH and coordination modulators, capping agents, demonstrated as an effective vey to control and reduce the particle size of Dy(BTC)H_2O crystals that are formed with 1,3,5-BTC linker. Deprotonation of 1,3,5-BTC was proposed to be more rapid at higher pH values leading to fast nucleation and reduced particle size. Additional presence of capping modulator as sodium acetate, restrict the crystal growth, nano-sized crystals are obtained. Similar low particle sized crystals were obtained with acetic acid as modulator and TEA as pH modulator. However, without the capping agent, only tuning pH of the medium resulted in a fast deprotonation of 1,3,5-BTC and nucleation due to increased basicity so micro-sized crystals were produced. On the other hand, bulk crystals of Dy(BTC)H_2O were obtained at lower pH values due to slow deprotonation of BTC linker and nucleation [114].

Time and Temperature: Reaction temperature and time are important parameters in majority of the MOF synthesis methods. Solubilities of organic linkers, reaction energy barriers and the reaction kinetics are highly dependent on temperature of the synthesis medium. For some flexible organic linkers, carboxylates, and metal centres [116], the coordination modes and conformations can be altered with different temperatures leading to MOFs with different dimensionality and topology [117]. Phase pure MOF-5 (a MOF constructed from zinc metal ion and terephthalic acid organic linker in DMF). that was synthesized at 140 °C was produced relatively rapidly from a metastable intermediate solid phase, that was formed priorly, rather than a reaction progressed straightforwardly. Whereas,

at 120°C and below, metastable intermediate solid phases reported to be persistent for longer period so longer reaction times were required for MOF-5 synthesis [118]. In another study, the effect of reaction time on the yield of HKUST-1, ($Cu_3(BTC)_2$) was demonstrated. The yield was increased with increased reaction time for both solvothermal and microwave synthesis methods. However, this increase was especially rapid in case of MW synthesis [119].

Molar Ratio of Reactants: Morphology, topological pattern of MOFs differs with molar ratios of metal, ligand solvent and modulator if present [109]. In a study with ZIF-8, held by Lai et al., changes in solvent to metal molar ratio in the synthesis shown to result in different particle sizes and crystallinities which affected the CO_2 uptake performance of the resultant frameworks. Among the ZIF-8 crystals, that are synthesized at RT from zinc nitrate, 2-MeIm linker and methanol as solvent, the one with synthesis solution containing lowest methanol to zinc nitrate molar ratio obtained largest particle sizes, highest crystallinity, and CO_2 uptake [120]. Wang et al. demonstrated the effect of temperature and reactant molar ratios on the synthesis of MOF-5 that is obtained from solvothermal synthesis of zinc metal ions and terephthalic acid linkers. Increased temperatures and metal to ligand ratios resulted in different morphology such that morphology changed from sheet to cubic [121].

1.2.3. MOFs Applications in MFCs

Unique characteristics of MOFs make them useful materials in various application areas such as drug delivery, biomedicine, batteries, gas adsorption and separation, fuel cells and many more. In microbial fuel cells, different MOFs can be utilized as catalysts in novel anode and cathode electrodes as well as conductive filler materials for PEM.

MOF Supported Anodes in MFCs: Pristine Metal Organic Frameworks can be used in anode electrodes of MFCs for enhanced electron transfer efficiency and improved performance of the cell due to their high surface area, porous structure and functionalities that are gained through the type of linker and metal used for synthesis. However, there are

not many publications regarding MOFs as anodic materials in MFC technology which might be due to their moderately low electrical conductivities and lack of biocompatibility studies. In a study, MIL-53(Fe) and NH_2-MIL-53(Fe) frameworks were employed in a coating slurry with PTFE as binder material and acetylene black as active material and conducting constituent, to enhance biofilm formation on the anode surface to be used in a two-chamber microbial fuel cell. Also, another anode electrode is prepared by coating a slurry containing only acetylene black and PTFE on stainless-steel mesh (SSM) for comparison. Anodes containing MOF-AB composites showed higher redox current densities of the amino groups in the anodic solution (NH_2-MIL-53(Fe) highest) and additional oxidation peaks of Fe^{3+} in the solution compared to electrode with AB with CV analysis. MFCs with MOF composites demonstrated improved performances and highest maximum power density was reported from MFC with NH_2-MIL-53(Fe) anode, which is increased by 21% and 53% compared to the MFC with MIL-53(Fe) and AB anodes. Introduction of amino groups to Fe-MOF resulting in NH_2-MIL-53(Fe) reported to generate rougher anode surface with increased active sites and the obtained biocompatibility and increased electrostatic attraction of anode with the improved electron transfer between microorganism and anode increased the performance of the fuel cell [122].

MOFs as Cathode Catalysts in MFCs: Pristine MOFs, their composites, and derivatives each with their porous structure, high surface area and active sites have great potential as electrocatalysts for OER/ORR [123].

Pristine MOFs are powerful candidates for ORR catalysts due to their high surface area, porous structure, functionality, and high active sites. However, they often show poor conductivities due to MOF's nature. Approaches like mixed valency [124] and selection of conductive organic linkers with highly conjugated structures (such 2,3,6,7,10,11-hexaiminotriphenylen) can be employed to overcome this limitation. Besides pristine MOFs, MOF composites with conductive carbon materials can be employed as electrocatalysts in which MOFs are responsible for active sites for ORR and carbon materials are present to increase conductivities for related energy applications [125]. Porous MOF derivatives often obtained by post treatments such as pyrolysis of MOFs that is leading to carbon-based

catalysts with both inherited characteristics of MOFs and additional features as higher active sites, more porous structure, and improved conductivity [126]. On the other hand, metallic derivatives with high specific area, porosity, and active sites are produced when the organic linkers in MOFs are consumed by calcination in air or chemical etching [127]. ORR that is taking place in MFC cathode is a key factor that is responsible for optimization of their performances. Pristine MOFs, MOF derivatives and MOF composites with their unique characteristics can be used as high performance electrocatalysts for enhanced ORR to improve power outputs of MFCs due to their high surface area, porosity, conductivity, and stabilities [82]. For instance, a MOF-derived catalyst was obtained from pyrolysis of ZIF-67, a Co-MOF, at 900 °C under nitrogen gas. When obtained CoNC was employed as cathode catalyst, the single chamber MFC exhibited a maximum power density of 1665 mWm^{-2} which is 39.8% higher than the MFC with commercial Pt/C cathode catalysts [128]. In another study, a water stable Zr-MOF (UiO-66) that is obtained through solvothermal synthesis was coated on CF cathode and utilized as an air cathode catalyst. Catalyst ink solution was composed of UiO-66, acetylene black, acetone and a binder polymer (PDMS). The MOF-containing cathode showed lower charge transfer resistance compared to cathode with 10% Pt/C coating and CF cathode without a catalyst. Through electrochemical characterizations, UiO-66 showed superior catalytic activity for ORR and when these cathodes were utilized in MFC, highest power density and power output was obtained by MOF supported cathode [61].

Besides the demonstrated good performances of MOF derivatives as cathode catalysts, use of pristine MOFs is highly important area for research since MFCs with bio-cathodes are an important emerging type of fuel cells. Microorganisms that are utilized in cathode compartment are used as biocatalysts to accept electrons from the cathode electrode and assist the reduction reaction further. For this manner, pristine MOFs with their unique characteristics as high surface area, porosity, and different chemical structures with a vast variety of organic linker choice may increase bacterial adhesion and enhance electron transfer.

2. SCOPE OF THESIS

Metal organic frameworks (MOFs) are the porous materials that are constructed from metal ions or clusters and organic linkers. Due to their unique characteristics as high surface area and porosity, stability, tunable pore size and composition make them useful materials in various application areas such as drug delivery, biomedicine, batteries, gas adsorption and separation, fuel cells, catalysis, and energy storage. In this thesis study, zinc (Zn), cobalt (Co) and iron (Fe) MOFs are aimed to be synthesized since they are highly abundant and cost-efficient metals and the effect of metal ion precursor type, reactant molar ratios, solvent amount and second metal addition on the formed framework is also examined. 2-metylimidazole, fumaric acid, terephthalic acid and 2-aminoterephthalic acid were used as the organic linkers for the formation of Zn, Co and Fe-MOFs since their synthesis conditions are rather convenient, they are cost efficient, and frameworks constructed from these linkers have potential towards catalytic activity towards oxygen reduction reaction. In this study, the aim is to expand the study of pristine Zn, Co and Fe-MOFs applicability as Microbial Fuel Cell (MFC) cathode catalysts. Synthesized MOFs are used to prepare slurries with carbon black and polyvinyl alcohol (as binder) and coated on stainless-steel mesh current collectors for the first time. Performances of prepared cathodes are evaluated in MFCs. Such a study also allowed investigation of composites prepared from pristine Zn, Co, and Fe-MOFs suitability as MFC cathode catalysts.

In Chapter 1, metal organic frameworks (MOFs) are introduced briefly. Different design approaches, synthesis methods and factors affecting the synthesis of MOFs are discussed. Some of the application areas of MOFs are also mentioned. Especially, their role as active materials for MFC electrode coatings are addressed. The aim of this thesis study and its summary are included in Chapter 2. Experimental procedures of MOF synthesis, preparation of coating slurries, properties of coated current collectors and information about the used characterization techniques are presented in Chapter 3. Results of this study and their discussion is held on Chapter 4. Synthesized frameworks were characterized by X-Ray Diffraction Analysis (XRD), Scanning Electron Microscopy and/or Energy-Dispersive X-

Ray Spectroscopy (SEM and/or EDX). The applicability of the electrodes that are prepared by coating stainless-steel mesh current collectors with MOFs and MOF-carbon composites was examined by Chronopotentiometry and Cyclic Voltammetry. Their morphologies are demonstrated via SEM images. Further performance analyses were performed on selected electrodes by utilizing them in the constructed MFC and performing Open Circuit Voltage, Linear Sweep Voltammetry and Electrochemical Impedance Spectroscopy Analysis. SEM images of the electrodes before and after being analysed in MFCs are also included. This thesis study is concluded in Chapter 5 and possible future works are mentioned in Chapter 6.

3. EXPERIMENTAL

3.1. Materials

Cobalt (II) nitrate hexahydrate (98%, Alfa Aesar), zinc (II) nitrate hexahydrate (98%, Thermo Scientific), zinc (II) chloride (99,99%, Alfa Aesar), manganese (II) nitrate hexahydrate (98%, Alfa Aesar), nickel (II) nitrate hexahydrate (98%, Alfa Aesar), iron (III) chloride hexahydrate (Merck), iron (II) chloride tetrahydrate ((98%, Alfa Aesar), Carbon Black Vulcan XC-72 (Fuel Cell Earth LLC), Graphene Oxide, 2- methylimidazole (99%, Thermo Scientific), 2- methylimidazole (99%, Sigma Aldrich), terephthalic acid (98+%, Thermo Scientific), 2-aminoterephthalic acid (99%, Thermo Scientific), fumaric acid (Fischer Scientific), ethyl cellulose (Sigma Aldrich), polyvinyl alcohol (Fluka Chemie) terpineol (Merck), ultra-pure water (obtained from Millipore, Milli-Q), ethanol (absolute, Merck), methanol, DMF and sodium hydroxide (VWR) were used in the experiments. Mercury Ultrasonic Cleaner with 40 kHz were used for sonochemical MOF synthesis and preparation of the slurries, to coat the stainless-steel mesh current collectors (stainless-steel Mesh 50, 304 grade) with carbon source MOF and binder. Drying oven (BINDER GmbH) and Domel Centric 260 R for centrifuge were used through MOF synthesis experiments. Heat gun (Steinel HL 2010 E) was employed for drying coated SSMs. GAMRY Interface Potentiostat was used for electrochemical evaluations of the prepared electrodes. LB Broth (Sigma Aldrich) was used for cultivation and growth of E. Coli K-12 to be utilized in MFC.

3.2. Synthesis of Metal Organic Frameworks

Zn, Co, Fe, and mixed metal MOFs are synthesized from organic ligands, metal salts, soluble precursors of metals, and other materials such as modulators via RT and sonochemical synthesis methods since they are easy to employ, advantageous synthesis routes. Precursors are mixed in solvent with different molar ratios at a fixed temperature for a certain time in each synthesis route. Products are separated by centrifugation, washed to remove unreacted constituents and solvent is evaporated to obtain the framework [96]. Fumaric acid, terephthalic acid, 2-aminoterephthalic acid and 2-methylimidazole were the organic ligands used to constitute the frameworks with different transition metals as Zn, Co, Fe, Mn, and Ni.

3.2.1. Zn-MOFs

3.2.1.1. Zn^{II}(2-MeIm).H_2O (ZIF-L).Zeolitic imidazolate frameworks with leaf-like morphologies were synthesized with two different zinc metal salts with metal to ligand molar ratios of 1:8 in accordance with the literature with some modifications. [129].

ZIF-L-1: 0.73g $Zn(NO_3)_2.6H_2O$ and 1.65 g 2-MeIm dissolved in 50 mL distilled water upon stirring separately. Then two solutions were mixed with constant stirring. Very cloudy, dense solution formed in 5 minutes. The mixture stirred at 350 rpm for 3.5 hours at RT on a magnetic stirrer then the solid content separated with the aid of centrifuge at 5000 rpm for 15 minutes. Product was washed with distilled water and centrifuged at 5000 rpm for 3 minutes three times. The solid obtained was dried at RT and in an oven at 60 °C for 7.5 hours.

ZIF-L-2: 0.34 g $ZnCl_2$ and 1.65 g 2-MeIm dissolved in 50 mL distilled water upon stirring separately. Then two solutions were mixed with constant stirring. The mixture stirred at 350 rpm for 3.5 hours at RT on a magnetic stirrer then the solid content separated with the aid of centrifuge at 5000 rpm for 15 minutes. It took longer for the formation of the dense

mixture. Product was washed with distilled water and centrifuged at 5000 rpm for 3 minutes three times. The solid obtained was dried at RT and in an oven at 60°C for 7.5 hours.

3.2.1.2. Zn^{II}(2-MeIm).MeOH (ZIF-8) and M/Zn^{II}(2-MeIm).MeOH.Zeolitic Imidazolate Frameworks are synthesized with 1:8 molar ratios of metal ion precursor and organic linker at RT with modified version of reported procedure [130].

ZIF-8-1: Each, 2 mmol (0.595 g) $Zn(NO_3)_2.6H_2O$ and 16 mmol (1.31 g) 2-MeIm dissolved in 12.8 g methanol separately on magnetic stirrer. Metal solution was added to ligand solution upon stirring on magnetic stirrer at 300 rpm for 3 hours at RT. White precipitates separated via centrifugation at 5000 rpm for 15 minutes. Then, washed with methanol and centrifuged for 3 minutes respectively three times. Obtained product was dried in oven at 65°C for 12 hours.

Bimetallic ZIF-8-1: Same procedure applied to ZIF-8-1 were performed only replacing half of the $Zn(NO_3)_2.6H_2O$ in terms of moles with the second metal salt. 1 mmol $Zn(NO_3)_2.6H_2O$ and 1 mmol $Co(NO_3)_2.6H_2O$ / $FeCl_2.4H_2O$ / $Ni(NO_3)_2.6H_2O$ were dissolved in 12.8 g methanol to obtain Co-doped ZIF-8-1, Fe-doped ZIF-8-1 and Ni-doped ZIF-8-1 respectively which are added to 16 mmol 2-MeIm dissolved in 12.8 g methanol separately on magnetic stirrer and stirred on magnetic stirrer at 300 rpm for 3 hours at RT. Precipitates separated via centrifugation at 5000 rpm for 15 minutes. Then, washed with methanol and centrifuged for 3 minutes respectively three times. Obtained products was dried in oven at 65°C for 12 hours.

ZIF-8-2: Zn-MOF was synthesized with metal to ligand molar ratio of 1:8 and methanol used as solvent with total of 1410 mmol. Each 1.19 g $Zn(NO_3)_2.6H_2O$ and 2.63 g 2-MeIm dissolved in 22.6 g methanol seperately with stirring at 300 rpm. Metal salt solution was added to ligand solution slowly under stirring. Mixture stirred on magnetic stirrer for 30 minutes at 250 rpm and 40 minutes at 200 rpm respectively at RT then centrifuged at 5000

rpm for 15 minutes. Seperated solid was then washed with methanol and centrifuged at 5000 rpm 3min four times. Obtained solid product dried at 65°C for 12 hours.

ZIF-8-3: ZIF-8-3 was synthesized at RT according to the reported procedure with some modifications without any additives [131]. 5 mmol (1.5 g) $Zn(NO_3)_2.6H_2O$ and 40 mmol (3.3 g) 2-MeIm both dissolved in 70 mL methanol on magnetic stirrer at 250 rpm separately. Metal solution added to ligand solution upon stirring and a very dense, cloudy mixture formed in a few minutes. Mixture was stirred at 250 rpm for 24 hours at RT. Solid was separated via centrifugation at 5000 rpm for 10 minutes, washed with methanol three times and then dried at 80°C for 12 hours.

Pictures of the synthesized Zn-MOFs with different colors after removing the solvent are shown in Figure 3.1 below.

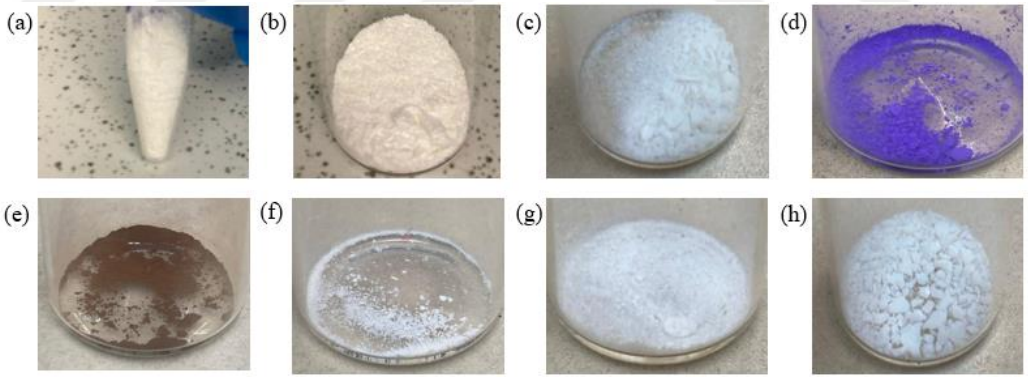


Figure 3.1. Pictures of Zn-MOFs (a) ZIF-L-1, (b) ZIF-L-2, (c) ZIF-8-1, (d) Co-doped ZIF-8-1, (e) Fe-doped ZIF-8-1, (f) Ni-doped ZIF-8-1, (g) ZIF-8-2 and (h) ZIF-8-3 respectively.

3.2.2. Co-MOFs

3.2.2.1. Co^{II}(2-MeIm).H_2O (ZIF-67-1) and M/Co^{II}(2-MeIm).H_2O.Co-MOFs were synthesized at RT with metal to ligand ratio of 1:21 and NaOH was used as additive to regulate and fasten the reaction as reported in the literature [76].

ZIF-67-1: 5 mmol NaOH and 16.8 mmol 2-MeIm dissolved in 5 mL distilled water upon stirring separately. 0.8 mmol $Co(NO_3)_2.6H_2O$ dissolved in 6 mL distilled water. Dissolved NaOH solution was first added to ligand solution then the metal solution is added drop by drop while stirring. When the metal was added to ligand solution, color turned to blue immediately. Mixture had stirred at 300 rpm 3 hours at RT then centrifuged 15 minutes at 5000 rpm. Obtained solid was washed with methanol and centrifuged for 4 minutes at 5000 rpm three times. Product was dried at 65°C in oven for 12 hours.

Bimetallic ZIF-67-1: Same procedure applied to form ZIF-67-1 was employed to obtain bimetallic ZIF-67-1 particles only with replacing half of the moles of $Co(NO_3)_2.6H_2O$ in the reactant mixture with the related doping metal ion salt. 5 mmol NaOH and 16.8 mmol 2-MeIm dissolved in 5 mL distilled water upon stirring separately. 0.4 mmol $Co(NO_3)_2.6H_2O$ and 0.4 mmol $FeCl_2.4H_2O$ / $Mn(NO_3)_2.6H_2O$ / $Ni(NO_3)_2.6H_2O$ were dissolved in 6 mL distilled water for each framework. Dissolved NaOH solution was first added to ligand solution then the metal solution is added drop by drop while stirring. Mixture had stirred at 300 rpm 3 hours at RT then centrifuged 15 minutes at 5000 rpm. Obtained solid was washed with methanol and centrifuged for 4 minutes at 5000 rpm three times. Products were dried at 65°C in oven for 12 hours to obtain Fe-doped ZIF-67, Mn-doped ZIF-67 and Ni-doped ZIF-67 respectively.

3.2.2.2. Co^{II}(2-MeIm).MeOH/EtOH (ZIF-67-2) and M/Co^{II}(2-MeIm).MeOH/EtOH.Co-MOFs were synthesized without any use of modulators similarly with reported procedure [132].

ZIF-67-2: 6 mmol $Co(NO_3)_2.6H_2O$ dissolved in 40 mL solvent mixture of 1:1 (v/v) methanol and ethanol with stirring. 24 mmol 2-MeIm dissolved in 40 mL solvent mixture of 1:1 (v/v) methanol and ethanol with stirring. Metal solution and ligand solution were mixed upon stirring at 250 rpm and stirred for 30 minutes at RT. Then left to settle and kept undisturbed for 20 hours for formation of ZIF-67. Purple precipitate ascribed as ZIF-67-2 was separated by centrifugation, washed with ethanol three times and dried at 80°C for 12 hours.

Zn-doped ZIF-67-2: Zn-doped ZIF-67-2 was synthesized accordingly with the same molar ratios as the described procedure above. 3 mmol $Co(NO_3)_2.6H_2O$ and 3 mmol $Zn(NO_3)_2.6H_2O$ dissolved in 40 mL solvent mixture of 1:1 (v/v) methanol and ethanol with stirring. 24 mmol 2-MeIm dissolved in 40 mL solvent mixture of 1:1 (v/v) methanol and ethanol with stirring. Metal solution and ligand solution were mixed upon stirring at 250 rpm and stirred for 30 minutes at RT. Then it was left to settle, age. It was kept at RT for 20 hours without being disturbed. Dark purple to blue precipitate was separated by centrifugation, washed with ethanol and centrifuged three times and dried at 80°C for 12 hours.

Pictures of the synthesized Co-MOFs are shown in Figure 3.2.

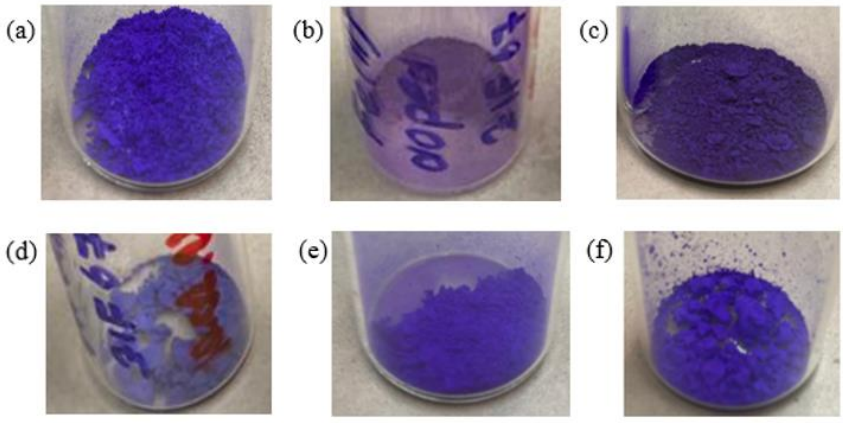


Figure 3.2. Pictures of the synthesized Co-MOFs, (a) ZIF-67-1, (b) Fe-doped ZIF-67-1, (c) Mn-doped ZIF-67-1 (d) Ni-doped ZIF-67-1 (e) ZIF-67-2 and (f) Zn-doped ZIF-67-2 respectively.

3.2.3. Fe-MOFs

3.2.3.1. Fe^{III}(FA).H_2O/EtOH (MIL-88A) and M/Fe^{III}(FA).H_2O/EtOH.Fe-MOFs were synthesized at RT accordingly with the reference procedure with few modifications using fumaric acid as the organic linker [133].

Fe^{III}(FA).DMF/EtOH (MIL-88A): 20 mmol (5.406 g) $FeCl_3.6H_2O$ dissolved in 75 mL distilled water with stirring on magnetic stirrer at 200 rpm. 20 mmol Fumaric Acid (2.321 g) dissolved in 75 mL EtOH with stirring on magnetic stirrer at 200 rpm. Metal salt solution was added to ligand solution and stirred for 24 hours at 100 rpm at RT. Solution is centrifuged at 5000 rpm for 10 minutes. Then, half of the solution washed with ethanol, centrifuged at 5000 rpm for 4 minutes twice and dried in oven at 80 °C for 12 hours. Obtained Fe-MOF was abbreviated as MIL-88A-1. Other half washed with distilled water and ethanol respectively and dried in oven at 80 °C for 12 hours was abbreviated as MIL-88A-2.

Co-doped MIL-88A-2: 2 mmol (1.0812 g) $FeCl_3.6H_2O$ and 2 mmol $Co(NO_3)_2.6H_2O$ were dissolved in 15 mL Distilled water with stirring on magnetic stirrer at 200 rpm. 4 mmol Fumaric Acid (0.4642 g) dissolved in 15 mL ethanol with stirring on magnetic stirrer at 200 rpm. Metal salt solution was added to ligand solution and stirred for 24 hours at 100 rpm at RT. Solid was separated via centrifugation at 5000 rpm for 10 minutes. Then, washed with Distilled water and ethanol respectively. Obtained brownish solid products dried in oven at 80 °C for 12 hours.

Zn-doped MIL-88A-2: 2 mmol (1.0812 g) $FeCl_3.6H_2O$ and 2 mmol $Zn(NO_3)_2.6H_2O$ were dissolved in 15 mL Distilled water with stirring on magnetic stirrer at 200 rpm. 4 mmol Fumaric Acid (0.4642 g) dissolved in 15 mL Ethanol with stirring on magnetic stirrer at 200 rpm. Metal salt solution was added to ligand solution and stirred for 24 hours at 100 rpm at RT. Solid was separated via centrifugation at 5000 rpm for 10 minutes. Then, washed with distilled water and ethanol respectively. Obtained light brown solid products dried in oven at 80 °C for 12 hours.

3.2.3.2. Fe^{III}(TPA).DMF.Fe-MOFs were constructed with the terephthalic acid as the organic linker accordingly with reported procedure [73].

Fe^{III}(TPA).DMF-1: 50 mmol $FeCl_3.6H_2O$ and 50 mmol TPA was dissolved in 25 mL DMF upon stirring on magnetic stirrer. Then kept in ultrasonic (US) bath for 4.30 hours at RT. When centrifugation was performed, there were no solid separated, so the mixture was placed on hot magnetic stirrer and stirred for 10 minutes at 60°C. Formation of very dense mixture was observed. It was centrifuged and washed with DMF twice. Then, the obtained solid was kept still in small amount of DMF overnight, dried in oven for 3 hours at 150°C

Fe^{III}(TPA).DMF-2: 5 mmol TPA and 5 mmol $FeCl_3.6H_2O$ mixed well in 25 mL DMF. Stirred at 200 rpm until clear mixture was formed then placed in US bath at 70°C for 2.5 hours. Solid was separated via centrifugation at 5000 rpm for 15 minutes, washed with DMF twice and washed with distilled water twice. Product was dried in oven at 80°C for 12 hours.

3.2.3.3. Fe^{III}(NH_2-TPA).DMF and Co^{II}/Fe^{III}(NH_2-TPA).DMF.Fe-MOFs were constructed from 1:1 metal to ligand ratio with the 2-amino terephthalic acid organic linker accordingly with reported procedure [73] with some modifications.

Fe^{III}(NH_2-TPA).DMF: 5 mmol NH_2-TPA (0.84 g) and 5 mmol $FeCl_3.6H_2O$ (1.36 g) mixed well in 25 mL DMF. Stirred at 200 rpm until clear mixture was formed then placed in US bath at 70°C for 2.5 hours. Solid was separated via centrifugation at 5000 rpm for 15 minutes, washed with DMF twice and washed with distilled water twice. Obtained dark brown solid was dried in oven at 80°C for 12 hours.

Co^{II}/Fe^{III}(NH_2-TPA).DMF: 1 mmol $FeCl_3.6H_2O$, 1 mmol $Co(NO_3)_2.6H_2O$ and 2 mmol 2-aminoterephthalic acid was dissolved and mixed in 5 mL DMF on magnetic stirrer at 200 rpm to create bimetallic Fe/Co-MOF with one pot synthesis procedure. Solution was transferred to US bath and kept for 2.5 hours at 70°C. SSM was centrifuged at 5000 rpm for

15 minutes, washed with DMF twice and washed with distilled water twice. Obtained dark green to brown solid was dried in oven at 80 °C for 12 hours.

Pictures of the synthesized Fe-MOFs with different colours are shown in Figure 3.3 below.

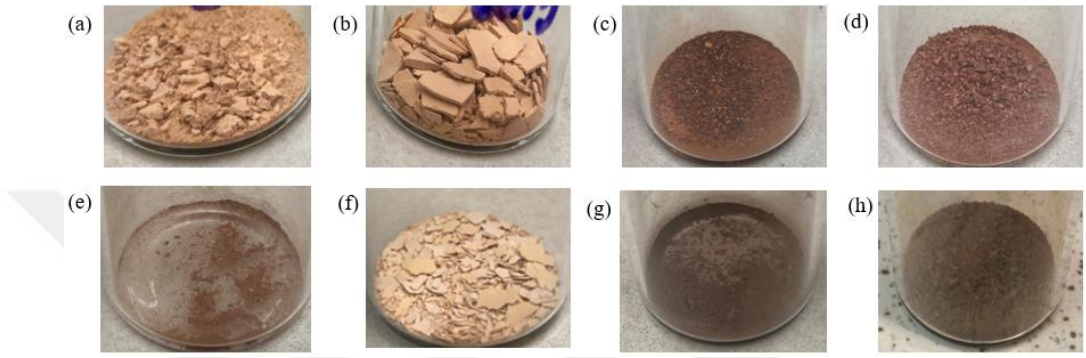


Figure 3.3. Pictures of synthesized Fe-MOFs, (a) MIL-88A-1, (b) MIL-88A-2, (c) Co-doped MIL-88A-2, (d) Zn-doped MIL-88A-2, (e) Fe^{III}(TPA).DMF-1, (f) Fe^{III}(TPA).DMF-2, (g) $Fe^{III}(NH_2\text{-TPA})$.DMF, (h) $Co^{II}/Fe^{III}(NH_2\text{-TPA})$.DMF respectively.

3.3. Preparation of Coated Stainless-Steel Mesh (SSM) Electrodes

Slurries to coat stainless-steel mesh current collectors are prepared from various constituents. Utilized stainless-steel meshes (SSMs) that are 0.35 mm thick, cut into different dimensions and treated with ethanol, acetone respectively, washed with distilled water and dried prior to coating. Slurries were prepared as binder-free and with polyvinyl alcohol (PVA) as binder. SSM current collectors were coated with carbon materials, carbon material/MOF composites, and MOFs only.

3.3.1. SSM Electrodes Coated with Carbon Slurries

3.3.1.1. Binder-Free Coating.SSM coated with carbon material without using any binder, only using the carbon source and solvent. Properties of the coating are given in Table 3.1.

SSM #1 (100% CB): 55 mg CB was dispersed in 1 mL EtOH and stirred on magnetic stirrer at 300 rpm for 3 hours. Obtained slurry was coated on a SSM, dried with application of heat gun at 50°C, 70°C, 100°C and this process repeated three times. Then, the coated mesh left at RT open air.

Table 3.1. Properties of SSM coated without binder, SSM #1.

SSM	**Carbon Source**	**SSM Coated Area (WxH, cm^2)**	**Binder**
SSM #1	CB	3.1 x 2.1	None

3.3.1.2. Coatings with PVA Binder.10% by weight PVA solution was prepared with distilled water to be used as binder in the following coatings by dissolving PVA (10% by weight) in distilled water at 60°C on magnetic stirrer at 350 rpm.

SSM #2 (90% CB / 10% PVA): 90% CB and 10% PVA by weight based on solid contents from 90 mg CB slurry was prepared. CB was dispersed in 1 mL ethanol with stirring. Then, 100 mg PVA solution (prepared with 10% by weight PVA solid) and 10 drops of ethanol was added additionally and stirred on magnetic stirrer for 1.5 hours. Then, mixture was placed in US bath, stirred continuously for an hour. Slurry was coated on the SSM, dried with application of heat gun at 50°C, 70°C, 100°C . This process was repeated twice.

SSM #3 (90% CB / 10% PVA): 90% CB and 10% PVA by weight based on solid contents from 56.25 mg CB slurry was prepared. CB was dispersed in 1 mL ethanol and placed in US bath with continuous. PVA was added and stirred for an hour.

Obtained slurry was coated on SSM #3, dried with application of heat gun at 50°C, 70°C, 100°C , and left at RT.

SSM #4 (90% GO /10% PVA): Slurry was prepared 90% GO and 10% PVA by weight based on solid contents from 22 mg GO. GO was dispersed in 2 mL EtOH and placed in US bath. 10% PVA solution was added upon continuous stirring with 4 drops of additional distilled water. Obtained slurry was coated on SSM #4, dried with application of heat gun at 50°C, 70°C, 100°C , and left at RT.

The properties of the coated SSMs, when polyvinyl alcohol was used as a binder to adhere the slurry onto the SSM surface, are listed in Table 3.2.

Table 3.2. Properties of SSMs coated with slurries prepared with PVA as binder.

SSMs	**Carbon Source**	**SSM Coated Area (WxH, cm^2)**	**Binder**
SSM #2	CB	2.3 x 2.0	PVA
SSM #3	CB	2.5 x 2.0	PVA
SSM #4	GO	3.0 x 1.5	PVA

3.3.2. SSM Electrodes Coated with MOF and MOF-Carbon Composite Slurries

SSM #5 (75% ZIF-8-3 / 15% CB / 10%PVA): Slurry was prepared by 75% ZIF-8-3, 15% CB and 10%PVA by weight based on solids. 45 mg ZIF-8 was mixed with 9 mg CB and dispersed in 3,6 mL ethanol on magnetic stirrer at 350 rpm. 60 mg of 10% by weight PVA solution that was prepared with distilled water was added to the mixture upon stirring. The coated mesh was dried with application of heat gun at 50°C, 70°C, 100°C respectively approximately for 5 minutes and left to dry further at RT.

SSM #6 (60% ZIF-L-1 / 30% CB / 10%PVA): 60% Zn-MOF, 30% CB and 10%PVA by weights of solids were used to prepare the coating slurry from 60 mg ZIF-L-1. 30 mg CB was dispersed in 1mL EtOH and mixed well and placed in US bath. Then PVA solution was added and stirred continuously for an hour. Through this process 1 mL EtOH was added additionally. Obtained slurry was then coated on the SSM, dried with application of heat gun at 50°C, 70°C, 100°C respectively approximately for 5 minutes and left at RT.

SSM #7 (80% ZIF-L-1 / 10% CB / 10% PVA): Slurry was prepared from approximately 80% ZIF-L, 10% PVA binder and 10% CB by weight based on solids from 50 mg ZIF-L. ZIF-L and CB was mixed well in 1 mL EtOH. Then, mixture was placed in US bath. PVA was added to the mixture and stirred well for an hour. 3 drops of distilled water was added while stirring.Slurry was then coated on SSM. Dried via applying heat gun at at 50°C, 70°C, 100°C and left at RT.

SSM #8 (100% ZIF-L-1): Slurry was prepared by dispersing 50 mg ZIF-L in 1 mL EtOH on magnetic stirrer. Then, 3 drops of terpineol were added to adjust the texture. Mixture was heated to 70°C for 10 minutes. Then, placed in US bath with addition of one more drop of terpineol, stirred continuously for an hour. Obtained slurry was coated on the SSM. Heat gun treatment was applied at 50°C, 70°C, 100°C and left at RT.

SSM #9 (80% ZIF-8-1 / 10% CB / 10% PVA): 80% Zn-MOF, 10% CB and 10%PVA by weight based on solid contents were used for preparation of the slurry from 45 mg ZIF-8-1. Zn-MOF and CB were dispersed in 1 mL EtOH. Then, 10% PVA solution was added, mixed at 350 rpm at 60°C. Then, mixture was placed in US and stirred well for 40 minutes. The slurry was coated on the SSM. Dried primarily with application of heat gun at 50°C, 70°C, 100°C respectively and left at RT.

SSM #10 (60% Zn-doped ZIF-67-2 / 30% CB / 10% PVA): 60% Zn/Co-MOF, 30% CB and 10% PVA based on solid weights were used to preapre the coating slurry with 42 mg Zn-doped ZIF-67-2. Zn/Co-MOF and CB were dispersed in 1.5 mL EtOH. Dispersion

stirred on magnetic stirrer for an hour at 350 rpm. Then, 10% by weight PVA solution was added and stirred on magnetic stirrer at 60°C, 350 rpm. Then, mixture was placed in US bath, stirred continuously for 40 minutes with addition of additional 0.5 mL ethanol. Slurry was coated on the SSM. Dried primarily with application of heat gun at 50°C, 70°C, 100°C respectively and left at RT.

SSM #11 (75% Zn-doped ZIF-67-2 / 15% CB 10% PVA): 75% Zn/Co-MOF, 15% CB and 10% PVA based on solid weights were used to preapre the coating slurry. 52.5 mg Zn-doped ZIF-67-2 was mixed with 10.5 mg CB and dispersed in 1 mL ethanol with stirring. Then, 70 mg 10% by weight PVA solution was added and stirred for an hour on magnetic stirrer at 60°C, 350 rpm. Then, mixture was placed in US bath, stirred continuously for 40 minutes. Some of the slurry was coated on the SSM. Dried primarily with application of heat gun at 50°C, 70°C, 100°C respectively and left at RT.

SSM #12 (80% ZIF-67-2 / 10% CB / 10% PVA): 80% Co-MOF, 10% CB and 10% PVA by weight based on solid contents mixed and dispersed in 1 mL EtOH on magnetic stirrer at 300 rpm. 56 mg ZIF-67 was used for coating slurry preparation. Through this procedure, stirred for an hour on magnetic stirrer at 60°C, 350 rpm. mixed well and stirred until it reached back to RT. Mixture was placed in US bath for an hour, stirred. When the texture became honey-like, coated on SSM. Dried primarily with application of heat gun at 50°C, 70°C, 100°C respectively and left at RT.

SSM #13 (80% MIL-88A-1 / 10% CB / 10% PVA): MOF-carbon composite to coat SSM electrode was prepared by 80% MIL-88A-1, 10% PVA binder and 10% CB by weight based on solid contents from 80 mg MIL-88A. Fe-MOF and CB was mixed on magnetic stirrer with 5 mL ethanol for 30 minutes at 250 rpm. Then, 100 mg PVA binder solution (10% by weight PVA in distilled water) added and stirred. After addition of binder solution, mixture was placed in US bath and stirred continuously for an hour. Obtained slurry was coated on SSM and each side was subjected to heat gun treatment of 50°C, 70°C, 100°C respectively approximately for 5 minutes.

SSM #14 (32.25% MIL-88A-1 / 68.75% PVA): 20 mg MIL-88A-1, a Fe-MOF, was dispersed in 15 drops of ethanol and placed in US bath. 0.44g 10% by weight PVA solution was added and stirred. After addition of binder solution, mixture was placed in US bath and stirred continuously for an hour. To adjust the texture of coating material, 5 drops of distilled water was added as well. Some of the obtained slurry was coated on the SSM and heat gun treatment at 50°C, 70°C, 100°C were applied.

SSM #15 (80% Fe-MIL-88B / 10%CB / 10% PVA): Slurry was prepared with 80% Fe-MOF, 10% CB and 10% PVA binder by weight in terms of solid content. 25 mg Fe-MIL-88B and 3.12 mg CB was dispersed in 1 mL EtOH, mixed well. After addition of binder solution, mixture was placed in US bath and stirred continuously for an hour. Obtained slurry was then coated on the SSM and heat gun treatment at 50°C, 70°C, 100°C were applied.

Properties of SSMs coated with MOFs and MOF-carbon composites are summarized in Table 3.3.

Table 3.3. Properties of the SSMs coated with MOFs and MOF-carbon composites.

SSM	**MOF/Carbon**	**SSM Coated Area (WxH, cm^2)**	**Binder**
SSM #5	ZIF-8-3/CB	2.5 x 1.6	10% by weight PVA
SSM #6	ZIF-L-1/CB	2.6 x 1.1	10% by weight PVA
SSM #7	ZIF-L-1/CB	2.5 x 1.6	10% by weight PVA
SSM #8	ZIF-L-1	2.7 x 1.7	Binder free

Table 3.3. Properties of the SSMs coated with MOFs and MOF-carbon composites. (cont.)

SSM	MOF/Carbon	SSM Coated Area (WxH, cm^2)	Binder
SSM #9	ZIF-8-1/CB	3.2 x 1.5	10% by weight PVA
SSM #10	Zn-doped-ZIF-67-2/CB	2.3 x 1.5	10% by weight PVA
SSM #11	Zn-doped-ZIF-67-2/CB	2.4 x 2.1	10% by weight PVA
SSM #12	ZIF-67/CB	3.4 x 1.5	10% by weight PVA
SSM # 13	MIL-88A/CB	2.5 x 1.5	10% by weight PVA
SSM #14	MIL-88A	2.3 x 1.9	10% by weight PVA
SSM #15	MIL-88B(Fe)/ CB	2.6 x 1.3	10% by weight PVA

3.4. Setup of MFC and Bacterial Inoculation

The construction of the fuel cell is shown in Figure 3.4, which was modelled from the reference [8]. Chambers and plates of the MFC is produced from plexiglass (PMMA) which are autoclavable. Each piece is connected to one another with rubber O-rings to seal and prevent leakage. Chambers have dimensions of 50 x 50 x 30 mm and 20 mm radius. Closable inlets were implemented for copper wires that are attached to the electrodes to complete the external circuit, addition of substrates and to gas the chambers (nitrogen for anode and oxygen for cathode chamber) (Figure 3.4b). Before MFC tests, all parts are autoclaved before bacterial inoculation, the anode chamber was purged with nitrogen gas and sealed tight. Oxygen was supplied to the cathodic chamber intermittently. Performance analyses were held in fed-batch mode of MFC at RT.

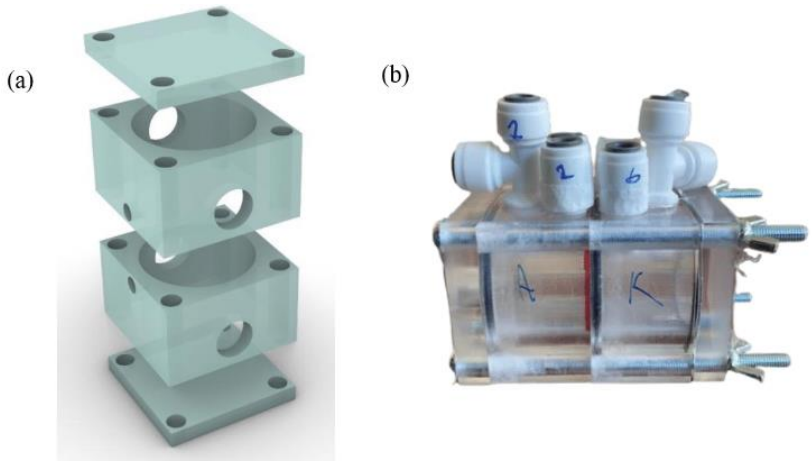


Figure 3.4. Image of the drawing (a) and constructed MFC (b).

E. Coli growth and inoculation was performed at Boğaziçi University Institute of Environmental Sciences, BIOMIG. E. Coli K-12 was initially cultivated in LB broth medium, that is composed of tryptone (10 gL^{-1}), yeast extract (5 gL^{-1}) and NaCl (5 gL^{-1}), aerobically at 37 °C on an incubator with shaker overnight and used to inoculate the fresh the anolyte, 30 mL M63B1 Medium (7.40 g/L K_2HPO_4, 3 g/L KH_2PO_4, 10 mL/L $(NH_4)_2SO_4$ (20%), 1 mL/L $MgSO_4.7H_2O$ (10%), 0.5 mL/L $FeSO_4.7H_2O$ (1%), 2 mL/L Thiamine (vitamin B1) (0.5%) and ultra-pure water), when it reaches the exponential phase. (OD_{600} between 0.5 to 0.8 nm). Before inoculating the bacteria to the medium, 5 mL of 10% by weight glucose solution was added to be used as substrate, carbon source for E. Coli K-12 cells. Before MFC was operation, the initial number of E. Coli K-12 in anolyte was (2.7 ± 0.7) x 10^7 CFU/mL *(n=3)*. On the other hand, 35 mL phosphate buffer (PB) solution (pH=6.92) was used as catholyte. Nafion 211 was placed in between two chambers and utilized as proton exchange membrane. Cathodes are cut into small dimensions. That is why the performance results are normalized with respect to cathode surface area.

3.5. Characterization Methods

SEM/EDX and XRD analysis are employed to characterize and evaluate the physicochemical properties of synthesized MOFs and/or composites. For electrochemical properties evaluation, cyclic voltammetry is employed and for conductivity measurements chronopotentiometry is used. The performances of the prepared novel electrodes are evaluated in MFCs by OCV, LSV and EIS.

3.5.1. X-Ray Diffraction Analysis (XRD)

Crystal structure, phase purity and crystallinity of the synthesized MOFs can be characterized by XRD. In principle, specific diffraction patterns give information on the crystalline substance by scattering of X-rays by the electron clouds around atoms [134]. Diffracted X-rays are reflected from planes within the crystal which occurs only when the following equation, Bragg's equation expressed as

$$n(\lambda) = 2dSin\theta, \tag{3.1}$$

where λ is the wavelength, n is an integer, d is the atomic interplanar distance, θ is the incident angle is satisfied [135]. XRD patterns of synthesized MOFs are collected with Rigaku D/MAX-Ultima+/PC Diffractometer with Cu-Kα radiation (λ=1.54 Å) in the XRD Facility of BU Advanced Technologies R&D Center.

3.5.2. Scanning Electron Microscopy/Energy Dispersive X-Ray Analysis (SEM/EDX)

Scanning electron microscopy (SEM) was used to gain topographic information of MOFs and coated SSMs through the obtained microscopic images. Morphology of samples and particle sizes are demonstrated by SEM imaging. Along with SEM, by employing EDS, semi-quantitative elemental analysis is performed to gain information on the elemental compositions of some of the MOFs within the control volume. SEM/EDX analysis for synthesized MOFs performed with FEI-Philips XL30 Environmental Scanning Electron Microscope with Field Emission Gun (Equipped with EDAX-Energy Dispersive X-ray

Analysis Unit) in the ESEM facility of BU Advanced Technologies R&D Center. Besides synthesized MOFs, SEM images of SSMs coated with MOFs and MOF composites are collected via Thermoscientific Quattro S in Boğaziçi University Center for Life Sciences & Technologies.

3.5.3. Chronopotentiometry

Chronopotentiometry is performed for four-probe conductivity measurements. Open-Circuit Potential can be obtained from chronopotentiometry measurements at zero current and with four-electrode setup (Figure 3.5). Accurate measurements of solution resistance or the resistance across the surface of the material can be obtained as well. Current of 0.01 A and 0.02 A and 1 A – 2 A were applied and the potential response with time was monitored and recorded by using GAMRY Interface Potentiostat to evaluate conductivities of the coated SSMs. Working and counter leads used for current application to carry the current and working sense and reference leads measure the voltage. Voltage across the inner probes is obtained by current flow through outer probes. All probes are placed with equal spacings through the SSM as shown in Figure 3.5.

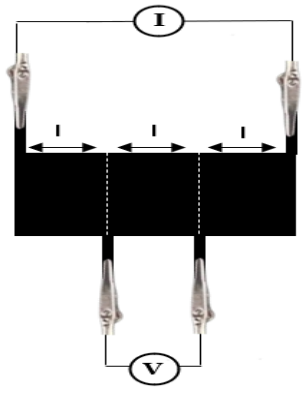


Figure 3.5. Schematic representation of physical chronopotentiometry measurements by four probes with equal spacing, shown as “l”.

Resultant plot of current vs. potential after application of two steps of current is displayed in Figure 3.6 as an example for an uncoated, bare mesh.

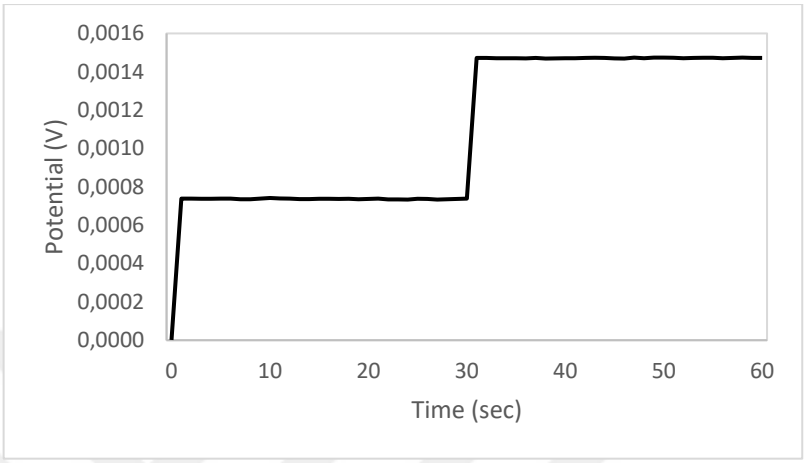


Figure 3.6. An example of a chronopotentiogram obtained from physical chronopotentiometry measurement.

Conductivities (σ) of bare and coated SSMs were calculated through the following equations

$$\rho = R * A/l \tag{3.2}$$

$$\sigma = 1/\rho, \tag{3.3}$$

where l is the distance between voltage probes, A is the cross-sectional area of the SSMs, and R is the resistance that is determined by R=dV/dI. Also, V is taken as the average of the recorded potentials at the corresponding current value. Resultant conductivities are reported as average as well.

3.5.4. Electrochemical Impedance Spectroscopy (EIS)

EIS which is non-intrusive or non-destructive electrochemical analysis method is commonly being used study performance of fuel cells since it makes measurements without affecting the fuel cell system's current-voltage characteristics [136]. It is an effective

characterization method for determining how various resistance parameters as electrolyte resistance, electrode resistance, charge transfer resistance etc., affect the fuel cells' total impedance [137]. EIS was performed on the MFCs containing carbon and/or MOF coated SSMs to analyse electrochemical behaviours and the performance of the MFC. GAMRY Interface Potentiostat was used to perform EIS analysis. Experimental setup parameters include AC Voltage (10 mV rms), initial frequency (Hz) of 10000 and final frequency of 0.1.

3.5.5. Cyclic Voltammetry (CV)

Current response of a redox active solution is measured by cycling the potential of the working electrode. It is utilized to understand and evaluate ORR kinetics of cathode used in MFCs under oxygen saturated medium [137]. While conducting cyclic voltammetry experiments, three electrode set-up was used. Counter and working electrodes are placed near to the reference electrode with equal distances. All electrodes are dipped in the electrolyte solution which is responsible of supplying the ions to the electrodes through oxidation and reduction reactions. The reference electrode maintains a constant potential whereas the working electrode's potential varies over time. Through CV experiments in this thesis study, Ag/AgCl was utilized as reference electrode, Pt wire was used as counter electrode and PB solution (pH=6,92) was used as the electrolyte medium. (Buffer solution was prepared from 0.2M Na_2HPO_4 and 0.2M KH_2PO_4 stock solutions.) Potential is applied by using GAMRY Interface Potentiostat, between the scan limits of 0.8V to -1.2 V and the resulting current is measured generating a cyclic voltammogram. Also, varying scan rates were applied as 50 mV/s and 100 mV/s to observe the effect of scan rate on the CV plot in terms of oxidation and reduction peak intensities.

3.5.6. Open Circuit Voltage Analysis (OCV)

OCP stands for open circuit potential, which is the potential that exists in an open circuit. It is the voltage recorded when there is no external load. The direction of the net current when the electrode is polarized in electrochemical cells is determined by the OCP,

which is dependent on the ions, charges present in the environment around the electrode. The highest possible cell voltage that can be obtained from a cell may be determined using the open circuit voltage which is determined by the difference between the anodic and cathodic OCPs when there is no external load [138].

3.5.7. Linear Sweep Voltammetry (LSV)

LSV is a commonly used voltametric method to evaluate the performance of a fuel cell. In contrast to CV, the voltage supplied to the working electrode is scanned linearly between initial and final potential, and the current produced is monitored. At the potentials where the species starts to be oxidized or reduced, a peak or dip in the current signal presence of a redox reaction [139]. Through LSV, measurements were taken at 20 mV/s scan rate. Obtained currents are further normalized with respect to cathode surface areas. Gamry potentiostat was employed for the LSV analysis with two-electrode configuration. Working sense lead was connected to working lead which was further connected to the anode electrode. On the other hand, reference lead was connected to counter sense and counter sense was connected to counter lead which was connected to the cathode electrode respectively.

4. RESULTS AND DISCUSSION

Characterization of Zn, Co, and Fe-MOFs are done through the SEM images and XRD patterns to reveal morphologic and crystallographic properties.

4.1. Characterization of Zn-MOFs

4.1.1. Zn^{II}(2-MeIm).H_2O (ZIF-L)

Leaf-like morphology of the synthesized Zn-MOFs are shown in Figure 4.1. ZIF-L-1 and ZIF-L-2 were synthesized from $Zn(NO_3)_2.6H_2O$ and $ZnCl_2$ metal salts respectively.

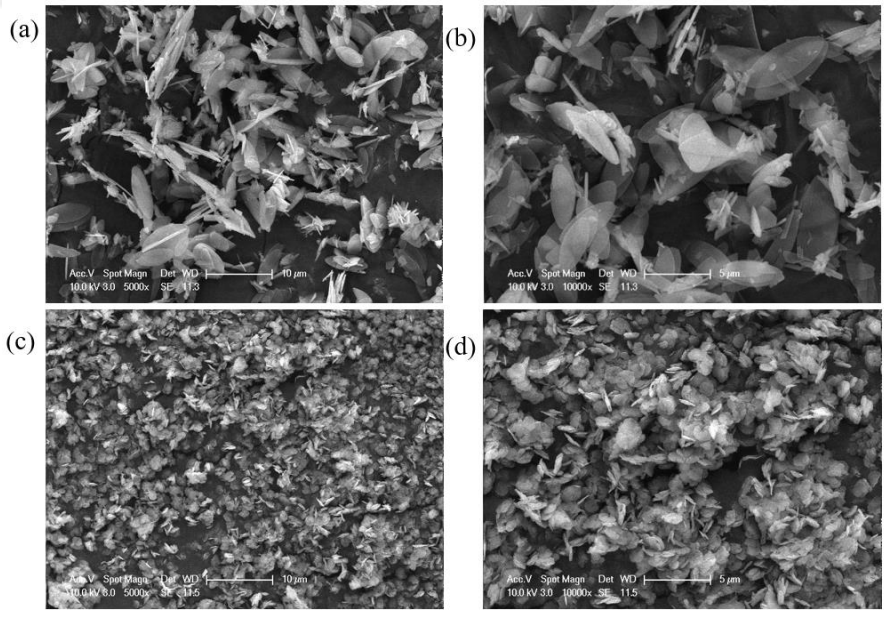


Figure 4.1. SEM images of ZIF-L-1 at (a) 5000x, (b) 10000x and ZIF-L-2 at (c) 5000x, (d) 10000x zoom level.

Even the metal to ligand ratio and amount of solvent was kept constant, the different metal ion source used for synthesis resulted in different particle sizes and slightly different morphology. SEM images of ZIF-L-2 demonstrated lower particle size than ZIF-L-1 (Figure 4.2). The length is approximately 3705 nm in average for ZIF-L-1 particles whereas the average length of ZIF-L-2 is approximately 938 nm.

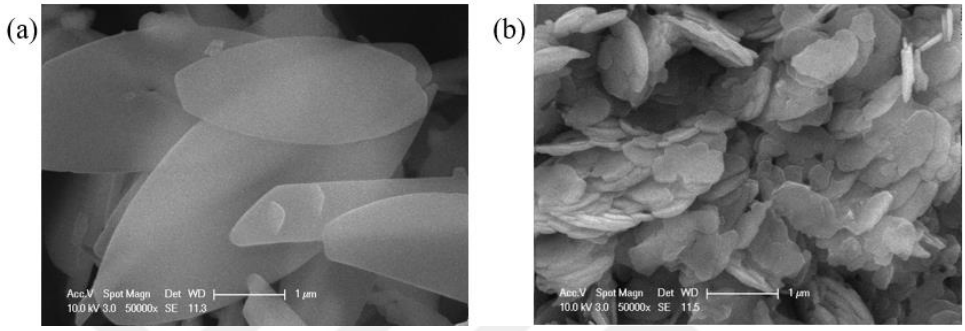


Figure 4.2. SEM images of (a) ZIF-L-1 and (b) ZIF-L-2.

The effect of metal ion precursor on the produced MOF was further evaluated with XRD patterns. As can be seen from the Figure 4.3, when $ZnCl_2$ was used as metal ion precursor, the resultant framework had different structure than the one synthesized from $Zn(NO_3)_2.6H_2O$ even the rest of the experimental conditions and procedure was same for both.

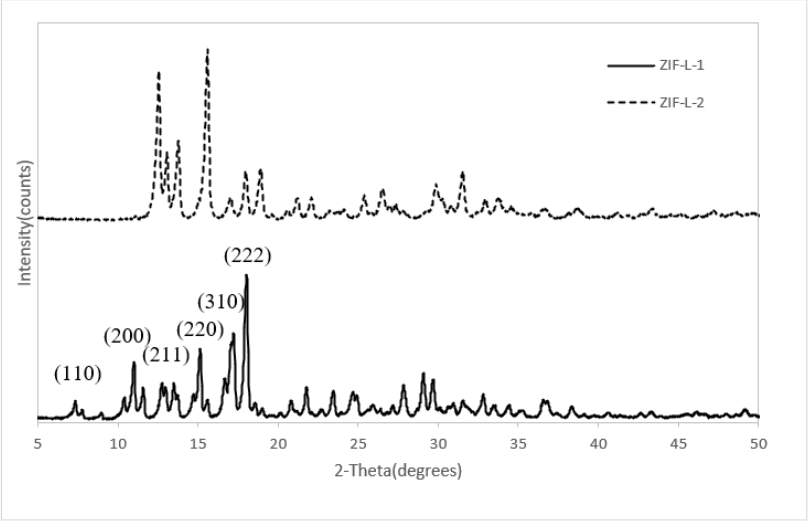


Figure 4.3. XRD pattern of ZIF-L-1 and ZIF-L-2.

Relative peak intensities and positions of the XRD pattern of ZIF-L-1 match well with the reference XRD pattern published in literature [140], which confirms successful synthesis of leaf-like shaped, highly crystalline and phase pure ZIF-L, a Zn-MOF. Peaks at 2θ values of 7.353°, 11.019°, 12.759°, 15.140°, 17.221°, 18.021° might be attributed to diffraction planes of (110), (200), (211), (220), (310), and (222) respectively accordingly with literature [141]. XRD pattern of ZIF-L-2 also exhibit some of the characteristic peaks but at shifted 2θ values with significantly changes in intensities. There were no exact matches for ZIF-L-2 particles when qualitative XRD analysis was performed. However, leaf-like structure formation is seen by SEM images (Figure 4.1c and Figure 4.1d). So, different phases might be formed for ZIF-L when $ZnCl_2$ was used as metal ion precursor. ZIF-L-1 particles were chosen as the Zn-MOF to be used as catalyst to create a coating to investigate its applicability as MFC cathode.

4.1.2. Zn^{II}(2-MeIm).MeOH (ZIF-8)

ZIF-8-1: Zinc ions (Zn^{2+}) and nitrogen atoms of 2-MeIm creates the structural units which further forms the framework of the ZIF-8, Zn-MOF. The morphology and average particle size, nearly as 68,34 nm, are obtained from SEM images (Figure 4.4).

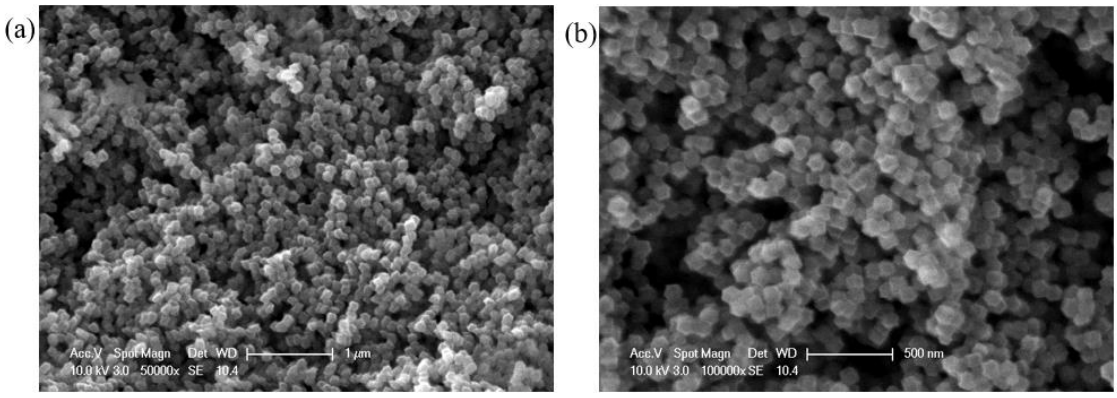


Figure 4.4. SEM images of ZIF-8-1 at (a) 50000x and (b) 100000x zoom level.

Peaks of the XRD pattern of ZIF-8-1 (Figure 4.5) appeared at 2θ values of 7.300°, 10.339°, 12.680°, 14.659°, 16.419°, 17.999°, 22.119°, 24.499°, 26.660°, 29.640°, 30.600°,

31.499°, 32.437° which can be attributed to diffraction planes of (011), (002) (112), (022), (013), (222), (114), (233), (134), (044), (334), (244), (235) [142].

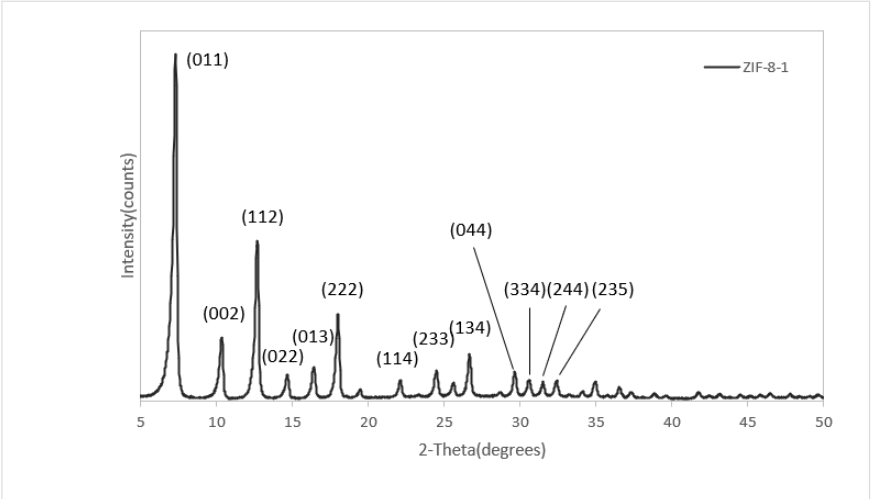


Figure 4.5. XRD pattern of ZIF-8-1.

ZIF-8-2: Synthesized ZIF-8-2 has shown to have the length of particles as 61.12nm from SEM images (Figure 4.6). Exact shape could not be identified due to low magnification since the particle sizes are very low. However, they look like rhombic dodecahedral which are the expected morphologies of ZIF-8 particles.

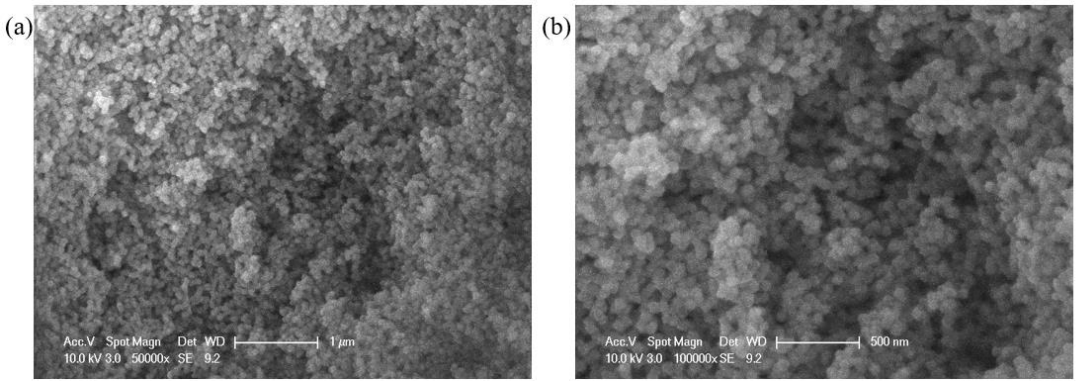


Figure 4.6. SEM images of ZIF-8-2 at (a) 50000x and (b) 100000x zoom level.

Through EDX analysis, C (42.28 w %), N (36.05 w %), O (3.44 w %) and Zn (18.23 w %) were detected in the ZIF-8-2 particles . Presence of oxygen might be because of oxidation of zinc ions since through the synthesis to the drying of the particles, whole process was exposed to air. However, amount of oxygen was reported as very little, and percentage of error is moderately high for it (32.98%).

XRD pattern displays the peaks at 2θ values of 7.360°, 10.419°, 12.740°, 14.700°, 16.460°, 18.060°, 24.539°, 26.720°, 29.739°, 30.641°, 31.580°, 32.421° degrees (Figure 4.7) which may correspond to the diffraction planes of (011), (002) (112), (022), (013), (222), (114), (233), (134), (044), (334), (244), (235) respectively as demonstrated in published XRD pattern [142].

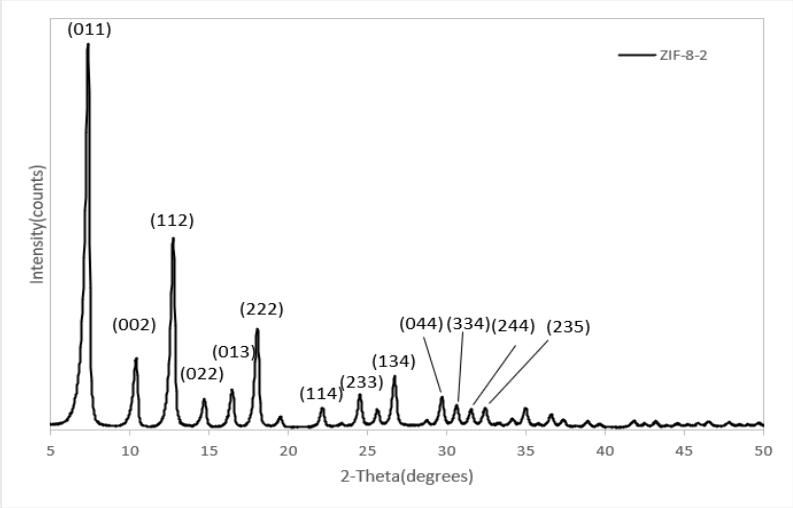


Figure 4.7. XRD pattern of ZIF-8-2.

ZIF-8-3: Morphology of ZIF-8-3 is displayed in Figure 4.8. From SEM images, the average length of particles is found as approximately 37,33 nm for ZIF-8-3 and particles looked like as if they have a rhombic dodecahedral like shape which is the expected form of ZIF-8.

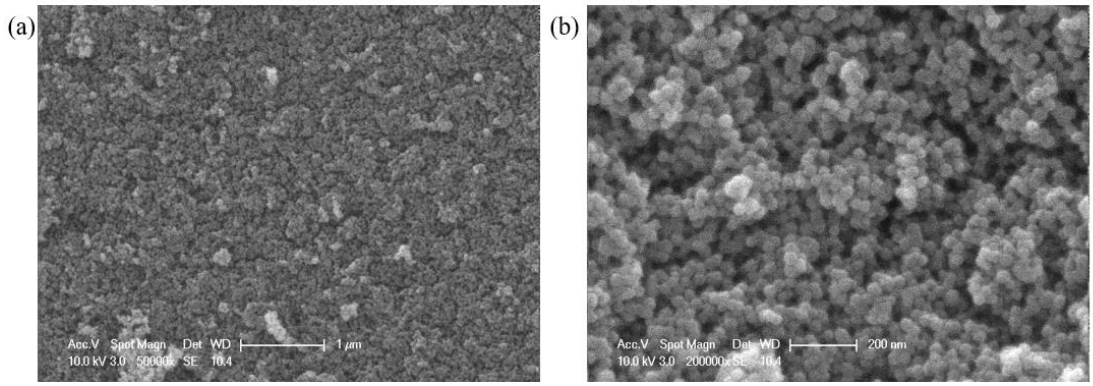


Figure 4.8. SEM images of ZIF-8-3 at (a) 50000x and (b) 200000x zoom level.

XRD pattern of the ZIF-8-3 is displayed in Figure 4.9. 2θ values of 7.340°, 10.400°, 12.720°, 14.759°, 16.440°, 18.001°, 22.179°, 24.560°, 26.681°, 29.699°, 30.660°, 31.522°, 32.459° might be attributed to the diffraction planes of (011), (002) (112), (022), (013), (222), (114), (233), (134), (044), (334), (244), and (235) similarly as published diffraction pattern of ZIF-8 [142].

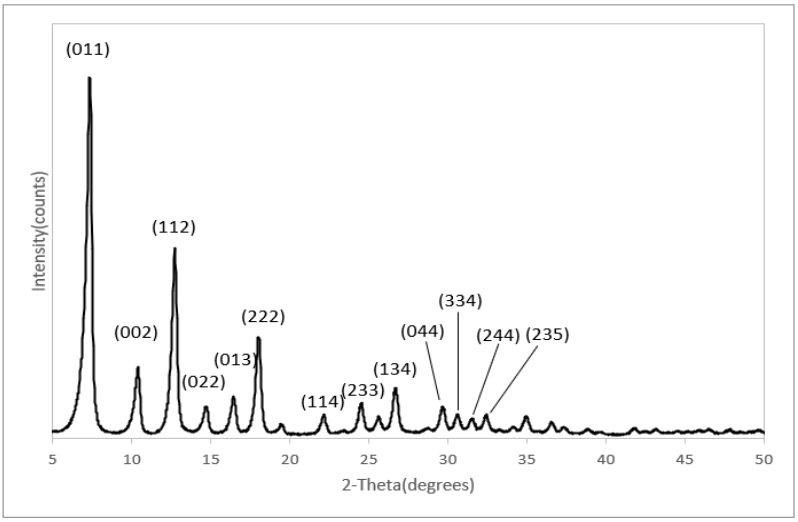


Figure 4.9. XRD pattern of ZIF-8-3.

As displayed in Figure 4.10, all the synthesized Zn-MOFs, ZIF-8-1, ZIF-8-2 and ZIF-8-3, have the diffraction patterns which overlap and exhibit similar diffraction patern with the published diffraction pattern of ZIF-8 [142]. Since the shifts in peak positions with

respect to this reference in the XRD patterns are so small and the obtained SEM images of the particles are consistent, it leads to the conclusion that all three synthesized ZIF-8s are phase pure.

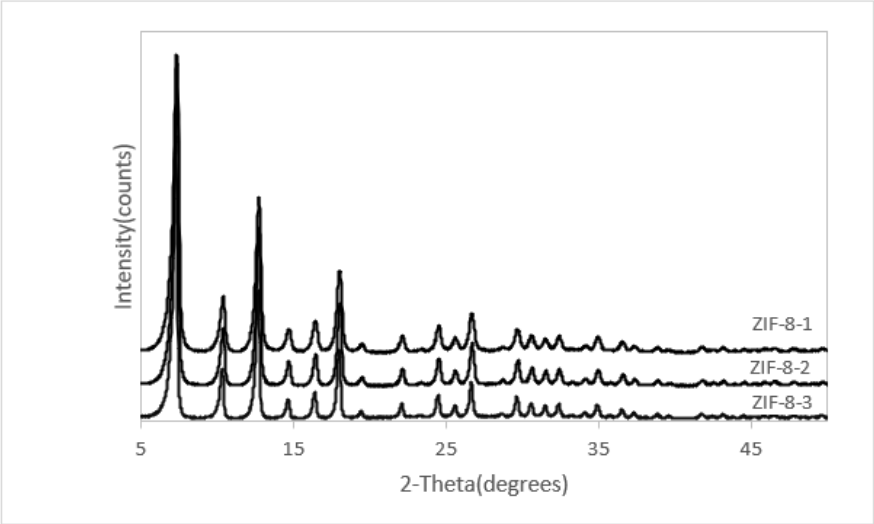


Figure 4.10. XRD pattern of all synthesized single metal ZIF-8s.

For the synthesis of ZIF-8-1, metal, ligand, and solvent ratio was 1:8:400 whereas it was 1:8:691.5 for ZIF-8-3 and average length of particles are 68,34 nm and 37,33 nm respectively. Higher molar ratio of solvent in the reaction media resulted in lower particle size.

Bimetallic ZIF-8s were synthesized with the same procedure and reactant ratios of ZIF-8-1, only the half of the amount of Zn metal ion precursors were replaced with another metal, Ni, Co, and Fe respectively. Figure 4.11 demonstrated the morphologies of the bimetallic ZIF-8s.

SEM images of Fe-doped ZIF-8-1 showed lower particle size and different morphology than of Ni and Co-doped ones which are very similar to single metal ZIF-8-1 showing a rhombic dodecahedral like shapes.

Obtained particles labelled as Fe-doped ZIF-8-1 might be iron and/or zinc oxide nanoparticles due to their very little particle sizes and morphology.

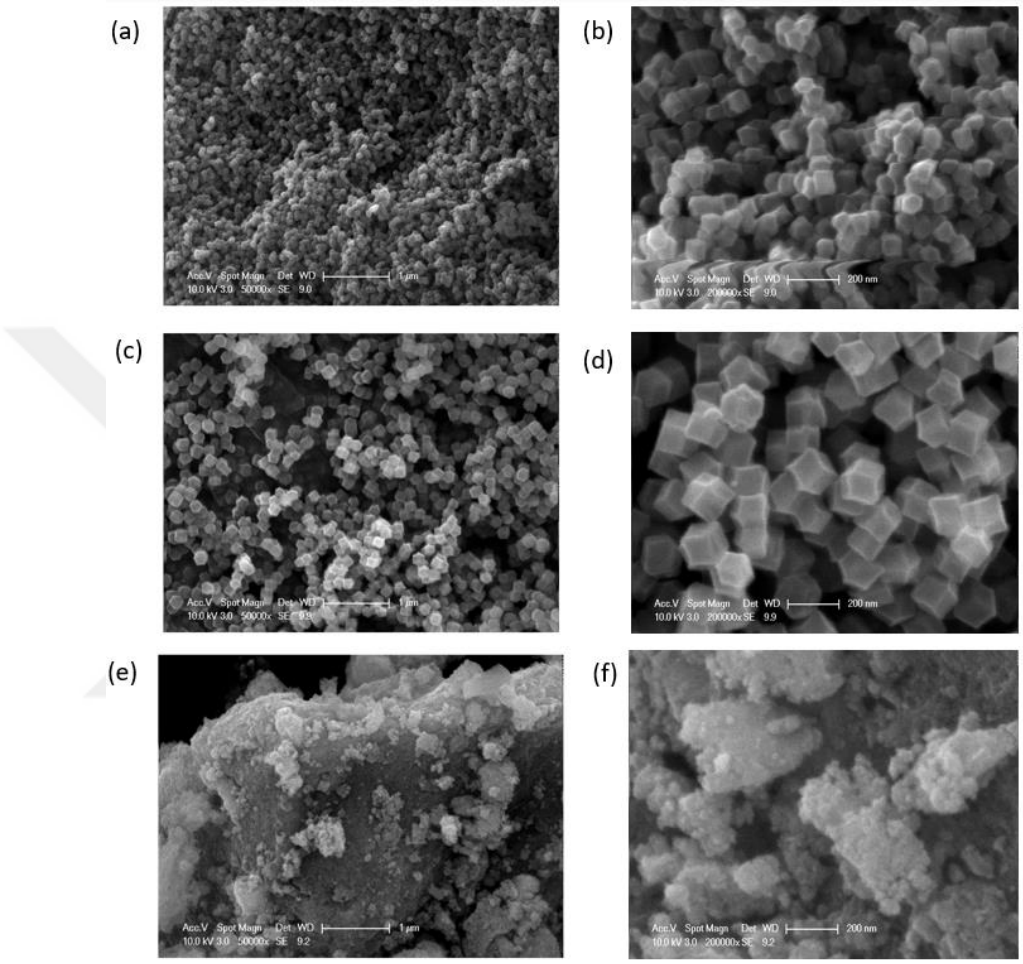


Figure 4.11. SEM images of (a) and (b) Ni-doped ZIF-8-1, (c) and (d) Co-doped ZIF-8-1, (e) and (f) Fe-doped ZIF-8-1 respectively.

The framework of ZIF-8-1 was not disrupted through replacement of half of the Zn metal ions with Ni and Co metal ions. Figure 4.12 shows that ZIF-8-1, and Ni and Co doped ZIF-8-1s display same XRD patterns. However, when Fe was used as dopant, XRD spectrum is different than single metal ZIF-8-1 which might be since presence of iron in the reaction media disrupted the framework formation. XRD pattern of the synthesized material labelled as Fe-doped ZIF-8 exhibited characteristic peaks of iron oxide similar to the published XRD pattern [143]. Very small and broad peaks at 2θ values of 32.410°, 34.394° and 61.514°

might be attributed to diffraction planes of (220), (311) and (440) respectively which leads to the conclusion that instead of a Fe-doped ZIF-8-1, iron oxide nanoparticles Fe_3O_4 were most probably obtained. Also, upon qualitative examination of XRD patterns, some of the characteristic peaks of Fe_3O_4 were matched with the synthesized compound.

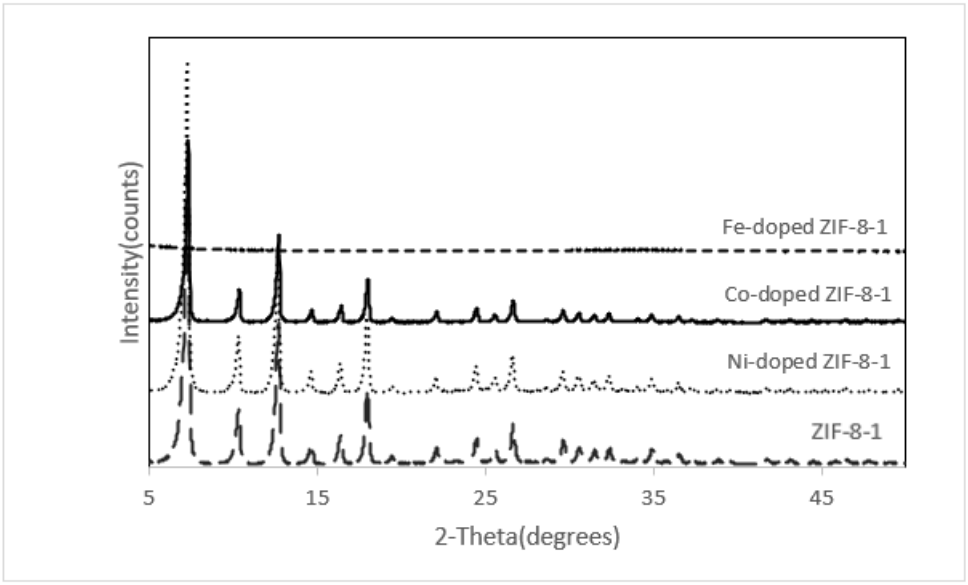


Figure 4.12. XRD pattern of ZIF-8-1 and bimetallic ZIF-8s.

4.2. Characterization of Co-MOFs

4.2.1. Co^{II}(2-MeIm).H_2O (ZIF-67-1) and M/Co^{II}(2-MeIm).H_2O

ZIF-67-1: SEM images showed polyhedron-liked shaped particles with average length of approximately 1.43μm with smooth surfaces (Figure 4.13).

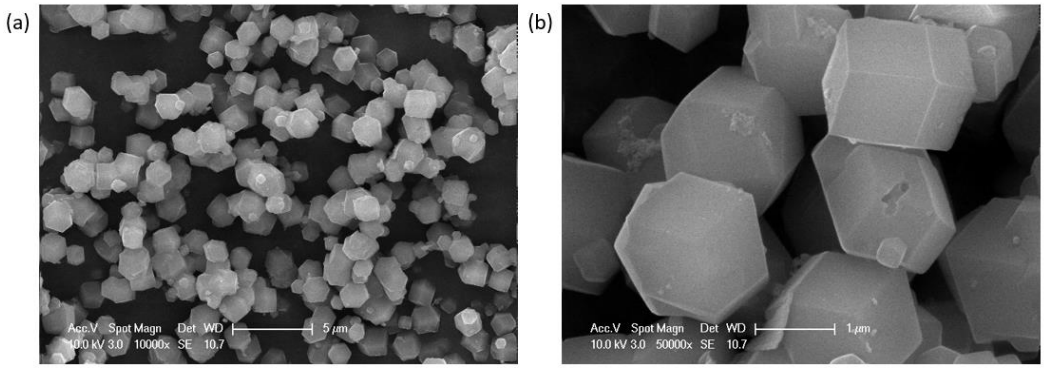


Figure 4.13. SEM images of ZIF-67-1 at (a) 10000x and (b) 50000x zoom level.

XRD pattern of ZIF-67-1 is displayed in Figure 4.14. Similar diffraction peaks as the published XRD pattern in literature [144] are observed. However, the intensities of diffraction peaks of the ZIF-67-1 differ from reported phase pure ZIF-67. Peaks with higher intensity than expected appeared at 2θ values of 16.480° and 18.060° which belong the ZIF-L phase of the Co-MOF. So, formation of a mixed phase with a very little characteristics of ZIF-L(Co) were obtained [144].

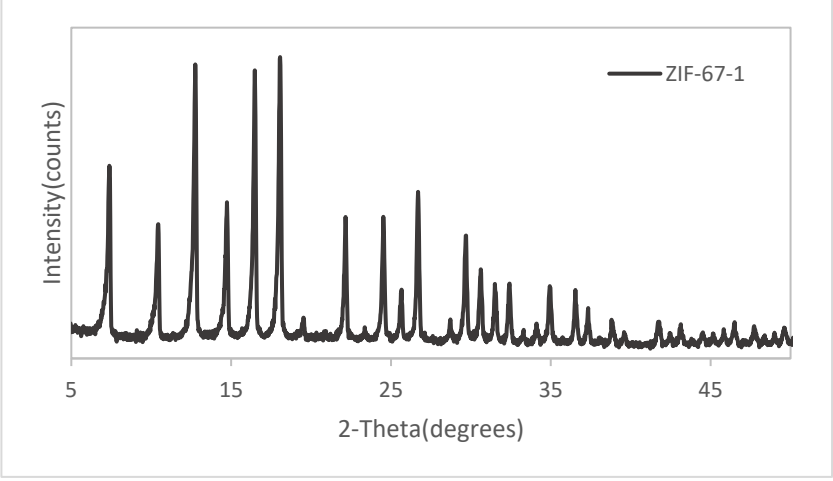


Figure 4.14. XRD pattern of ZIF-67-1.

Morphologies of Fe, Mn and Ni-doped ZIF-67-1 frameworks are displayed in Figure 4.15. Fe-doped ZIF-67-1 particles with rounded edges were obtained. When Mn was doped to ZIF-67-1, the SEM images look alike with single metal ZIF-67-1. However, the

morphology of the Ni-doped ZIF-67-1 is very much different than others (Figure 4.15e and f). It seems like polyhedron-like shaped particles could not formed.

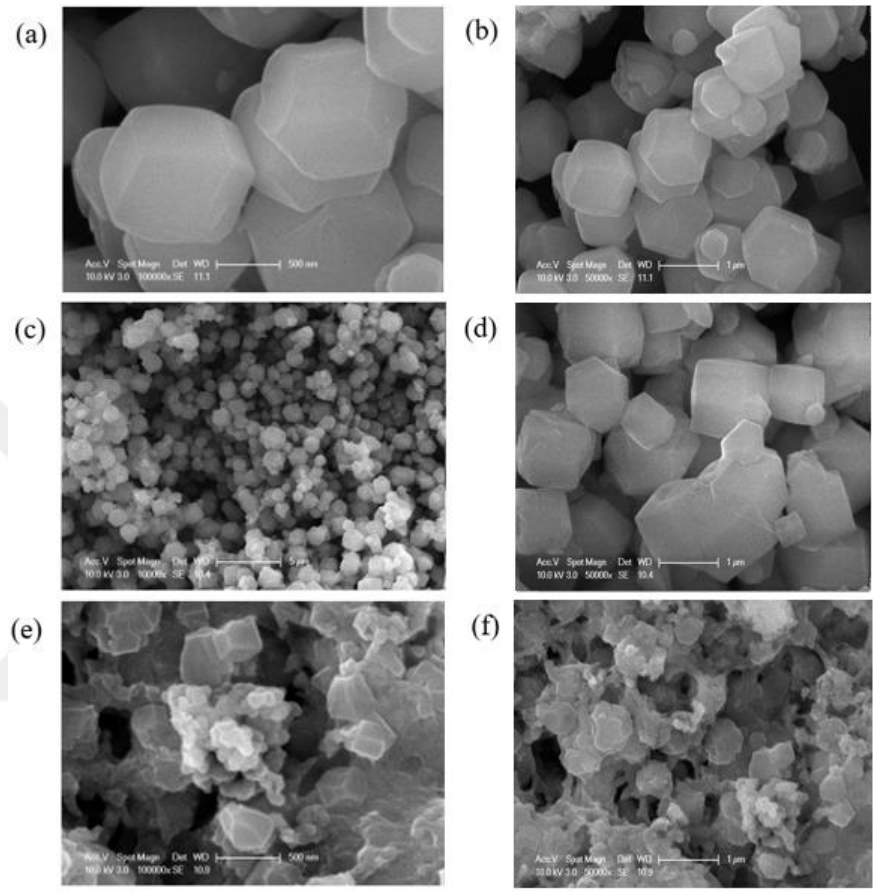


Figure 4.15. SEM images of (a) and (b) Fe-doped ZIF-67-1, (c) and (d) Mn-doped ZIF-67-1 (e) and (f) Ni-doped ZIF-67-1.

XRD patterns of ZIF-67-1 and ZIF-67-1 doped with different metals are shown in Figure 4.16. Except Ni-doped ZIF-67-1, all bimetallic frameworks exhibited diffraction peaks at same 2θ values with single metal ZIF-67-1 with different intensities. When nickel is doped, structure of ZIF-67-1 framework is totally disrupted. Both the SEM images and the XRD pattern indicate formation of another compound instead of bimetallic ZIF-67-1 (Ni/Co). There was no formation of ZIF-67 like particles and no exact match obtained through qualitative XRD analysis however, some of the peaks in the XRD pattern of this particle matched with characteristic peaks of CoO and the broad look of the peak might be due to amorphous structure instead of crystalline state. There were no matches indicating

presence of nickel-based compounds in the formed structure which might be due to cobalt ions in reaction medium having higher affinity towards formation of CoO particles and the remaining nickel ions are washed away upon washing the obtained particles to get rid of unreacted materials in reaction medium. Mn-doped ZIF-67-1 has higher ZIF-L(Co) characteristics within the structure than, Fe-doped ZIF-67-1 since the diffraction peak around 7.4° and 12.760° has lower intensity that is correlated with presence of ZIF-L(Co) phase of the framework [144].

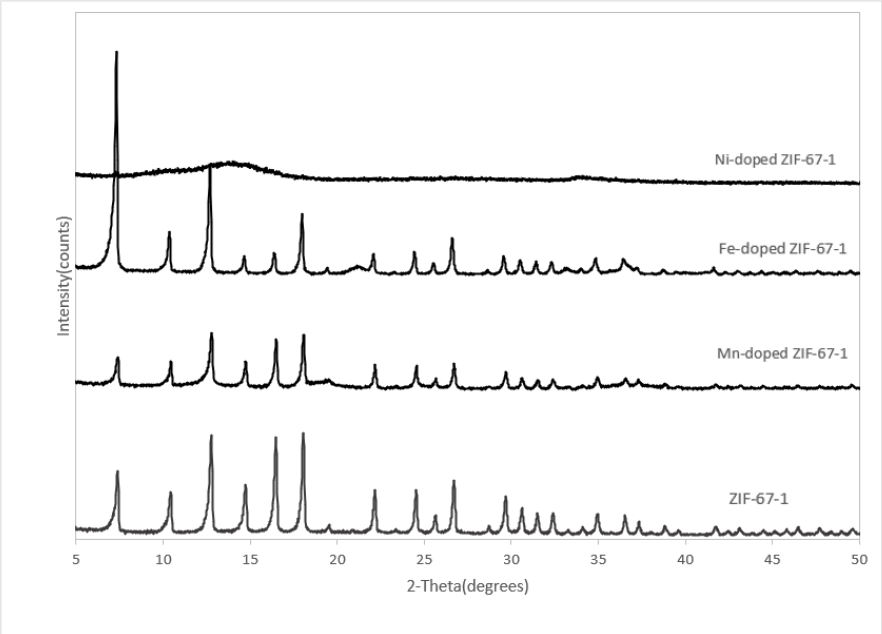


Figure 4.16. XRD pattern of ZIF-67 and Bimetallic ZIF-67s synthesized with NaOH.

4.2.2. Co^{II}(2-MeIm).MeOH/EtOH (ZIF-67-2) and M/Co^{II}(2-MeIm).MeOH/EtOH

Successful synthesis of ZIF-67, Co-MOF, which is made up of imidazolate ligands and divalent, tetrahedrally coordinated Co^{2+} metal ions demonstrated by SEM and XRD analysis results. Polyhedron-liked shaped particles are shown in Figure 4.17. From SEM images, the particle size of ZIF-67 was found as approximately 174 nm.

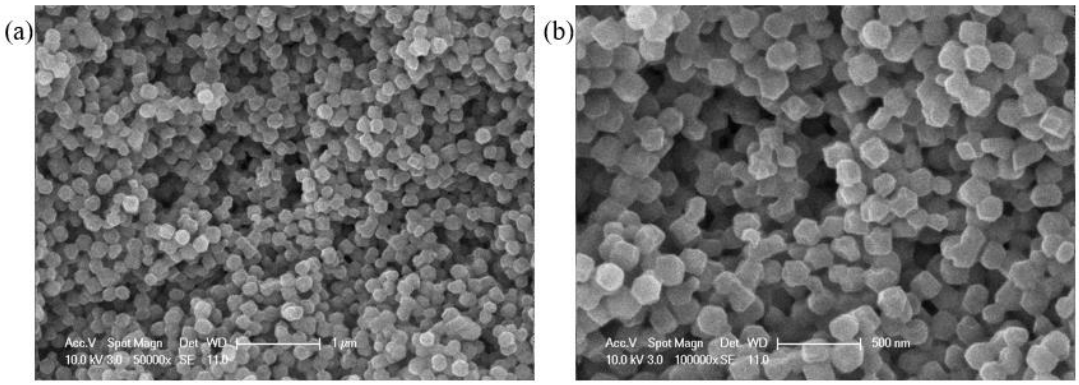


Figure 4.17. SEM images of ZIF-67-2 at (a) 50000x and (b) 100000x zoom level.

The phase purity of the synthesized ZIF-67 can be verified by the fact that the appeared peaks on the XRD spectrum strongly match those of the reported as-synthesized ZIF-67 and simulated ZIF-67. Based on the reference article, the peaks appeared at 2θ values of 7.36°, 10.40°, 12.74°, 14.72°, 16.46°, 18.02°, 22.12°, 24.59° and 26.66° (as can be seen from Figure 4.18) can be attributed to (011), (002), (112), (022), (013), (222), (114), (233) and (145) planes of the ZIF-67 crystal respectively as demonstrated similarly in published article [145].

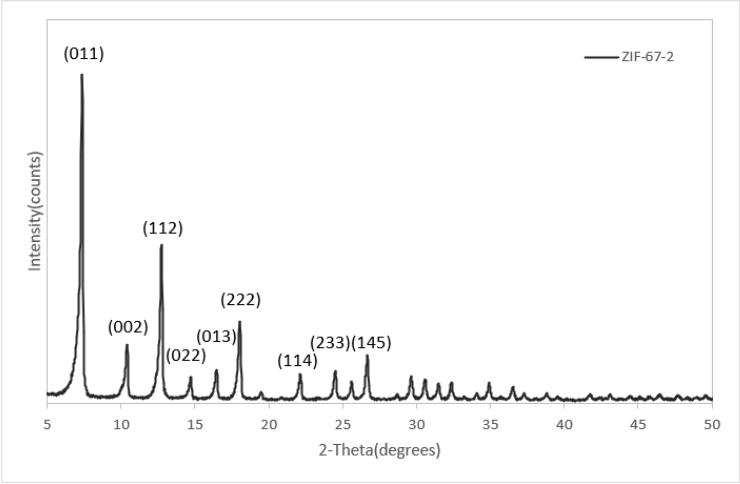


Figure 4.18. XRD pattern of ZIF-67-2.

Zn-doped ZIF-67-2: Zn-doped ZIF-67-2 particles are obtained by replacing half of the cobalt ion precursor in the reactant mixture with zinc ion precursors. SEM images are

displayed in Figure 4.19. Average particle size was found as 78,9 nm approximately from SEM images. Framework with lower particles size was obtained when mixed metal is used.

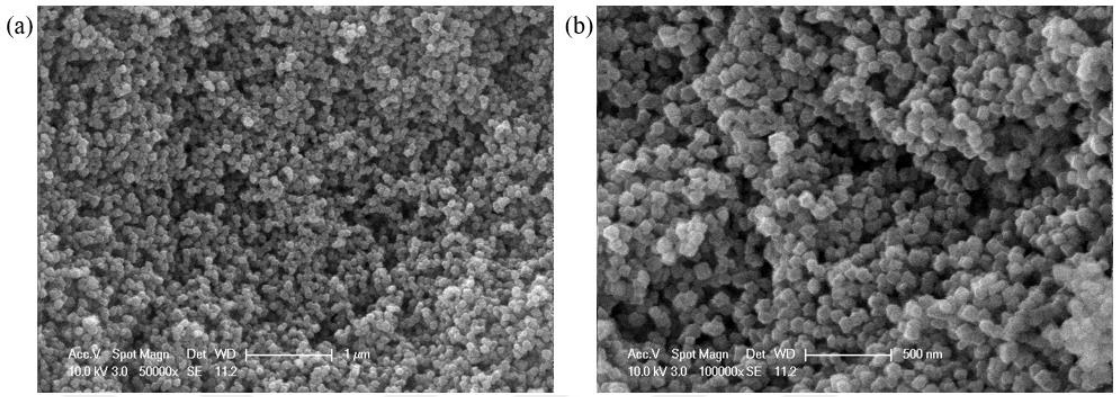


Figure 4.19. SEM images of Zn-doped ZIF-67-2 at (a) 50000x and (b) 100000x zoom level.

XRD pattern of Zn-doped ZIF-67-2 (Figure 4.20) is identical with single metal ZIF-67-2 particles. Peaks at 2θ values of 7.44°, 10.48°, 12.80°, 14.78°, 16.55°, 18.12°, 22.23°, 24.59° and 26.78° might correspond to (011), (002), (112), (022), (013), (222), (114), (233) and (145) planes of the crystal respectively as reported similarly in published article [145].

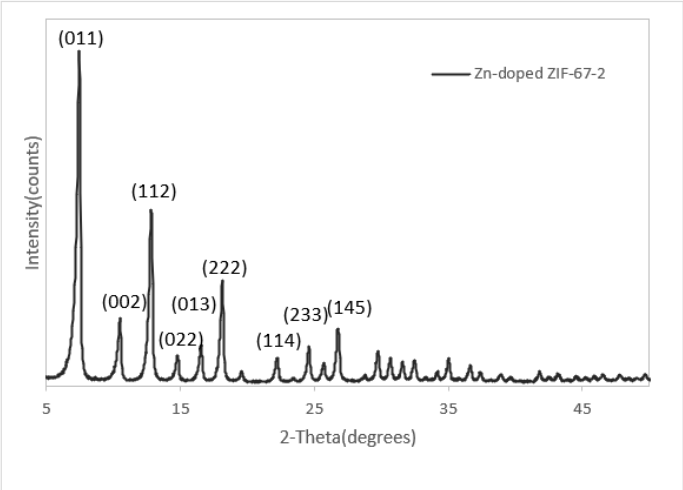


Figure 4.20. XRD pattern of Zn-doped ZIF-67-2.

As displayed in Figure 4.21, incorporation of Zn ions into the ZIF-67 framework did not disrupt the structure and single metal and bimetallic ZIF-67 exhibit same diffraction patterns. There are no additional peaks appeared for Zn-doped ZIF-67-2, and upon qualitative XRD analysis, there were not any match found for any zinc oxide, zinc hydroxide or any other materials that could possibly formed additionally. Even if there is some present, the weight percentage of those materials should be very low (like 3% by weight of the sample produced) so that there are no exact matches.

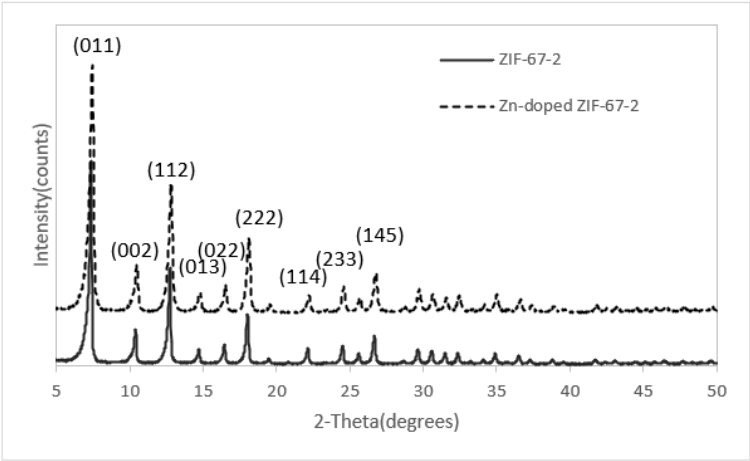


Figure 4.21. XRD patterns of ZIF-67-2 and Zn-doped ZIF-67-2.

Effect of NaOH as modulator on the formed framework is demonstrated in the XRD patterns in Figure 4.22. ZIF-67-2, the one synthesized without NaOH, displayed same diffraction pattern with phase pure ZIF-67 reported in literature [145–147]. That is why, ZIF-67-2 and Zn-doped ZIF-67-2 were used for preparing catalyst slurries to be test as cathode materials in MFC operation.

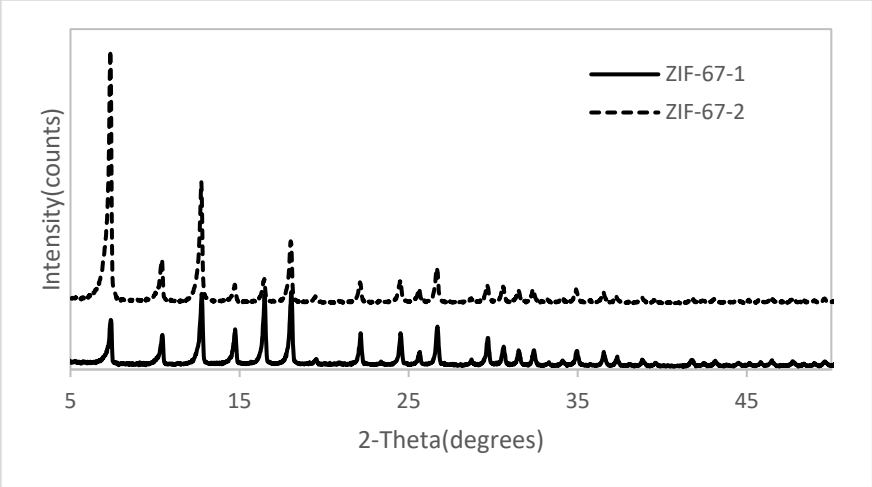


Figure 4.22. XRD patterns of ZIF-67-1 and ZIF-67-2.

4.3. Characterization of Fe-MOFs

4.3.1. $Fe^{III}(FA).H_2O$/EtOH (MIL-88A)

Fe-MOFs obtained from fumaric acid linker, ascribed as MIL-88A in literature, were synthesized with same procedure, only MIL-88A-1 was washed with only ethanol whereas MIL-88A-2 was washed with distilled water and ethanol respectively to observe the effect of guest molecules, washing solvents, on the framework.

As can be seen from SEM images in Figure 4.23, MIL-88A-1 and MIL-88A-2 both demonstrated a spindle-like morphology. However, the facets are more distinctive for MIL-88A-1 than MIL-88-2. Particle length for MIL-88A-1 was found as approximately 410 nm whereas it was found as 440 nm for MIL-88A-2 with respect to their SEM images.

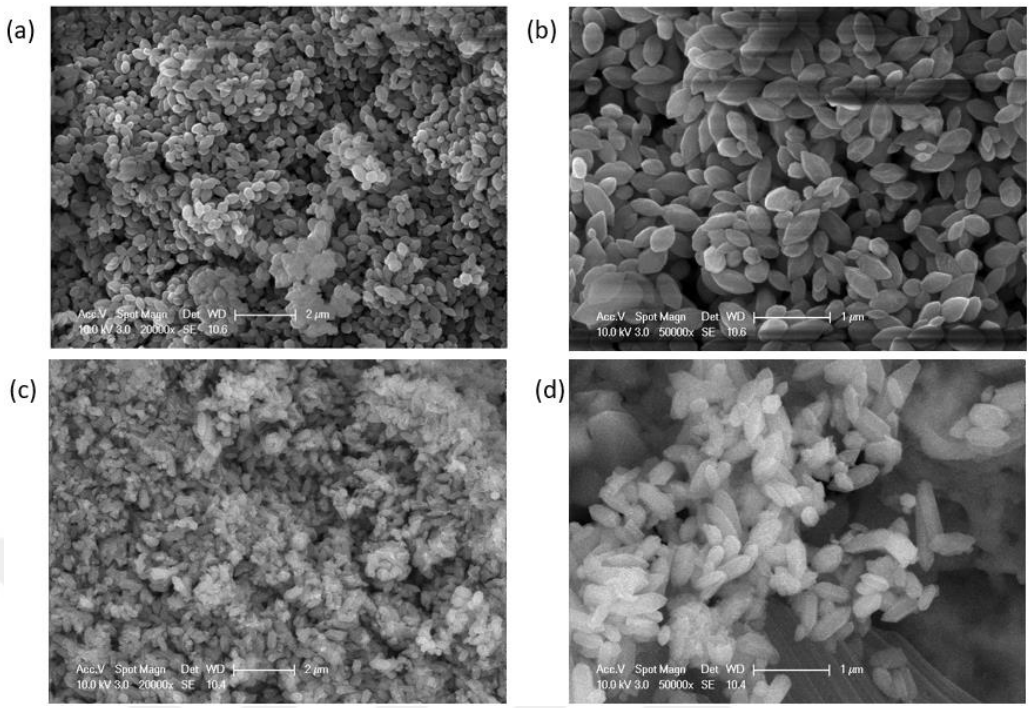


Figure 4.23. SEM images of (a) and (b) MIL-88A-1, (c) and (d) MIL-88A-2.

XRD pattern of MIL-88A particles are demonstrated in Figure 4.24. Characteristic peaks occurred in the diffraction pattern of MIL-88A-1 at 2θ values of 7.960°, 10.382° and 13.281°, 13.779°, 15.519°, 19.182°, 20.781° 22.085° 23.979° 24.982° 28.519° and 29.001° matched well with the reported spectra. Peaks are attributed to diffraction planes (010), (011), (110), (002), (012), (112), (022), (103), (030), (031), (130) and (004) respectively as demonstrated in the reference [148]. On the other hand, XRD pattern of MIL-88A-2, that is washed with ethanol and distilled water respectively differ significantly from MIL-88A-1's as expected which shows the effect of washing reagent, solvent, on the formed framework. Even tough peak positions have similar 2θ values, intensity of peaks is quite different. When qualitative XRD analysis were performed, there were no exact matches with the database, only some of the peaks in the pattern match with Fe_2O_3 indicating possibility of presence of very small amounts of iron oxide. So, some other phase of MIL-88A particles with presence of iron oxide could be formed.

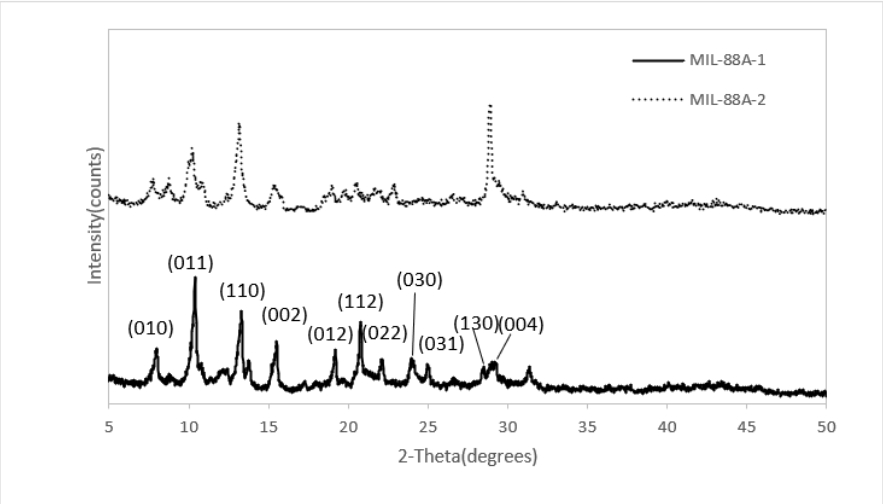


Figure 4.24. XRD patterns of MIL-88A-1 and MIL-88A-2.

Since MIL-88A-1 displayed lower average particle size, which may enhance its catalytic activity due to increased surface area, with respect to MIL-88A-2 and showed similar XRD pattern to reported frameworks in the literature, it was selected to be used in SSM coating as the catalyst.

4.3.2. Fe^{III}(TPA).DMF

Fe^{III}(TPA).DMF-1: SEM images of Fe^{III}(TPA).DMF-1 framework with its octahedral diamond-like shape is shown in Figure 4.25. From SEM images, the average length of particles was found to be around 902 nm.

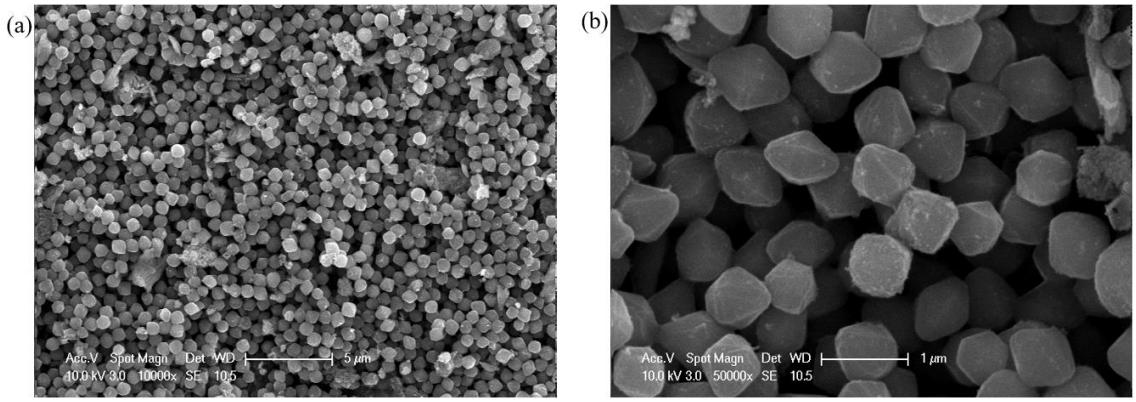


Figure 4.25. SEM images of Fe^{III}(TPA).DMF-1 at (a) 10000x and (b) 50000x zoom level.

XRD pattern of Fe^{III}(TPA).DMF-1 (Figure 4.26), match well with the reported version of MIL-53(Fe) [149] that is produced solvothermally and objected to sulfonation (Sulfuric acid and trifluoromethanesulfonic anhydride were added to solvent) even though there were no such treatments in this procedure.

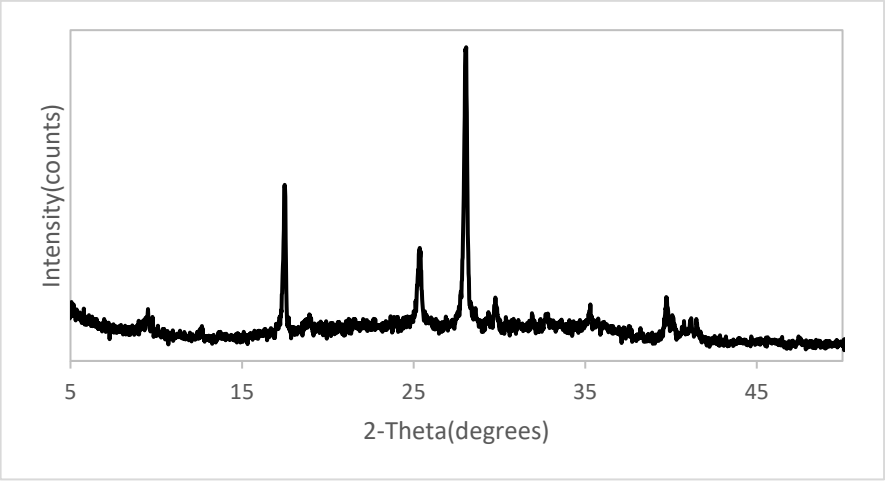


Figure 4.26. XRD Pattern of Fe^{III}(TPA).DMF-1.

Through EDX analysis, C (42.19 w %), O (30.55 w %), Fe(16.55 w %), Cl(7.22 w %) and Pt (3.49 w %) were detected in the Fe^{III}(TPA).DMF-1. Presence of very little amounts

of Pt is because of the Pt coating done for measurements and the Cl detected might be the traces of $FeCl_2.6H_2O$ precursor. This might be due to insufficient washing process through the synthesis.

Fe^{III}(TPA).DMF-2: SEM images of Fe^{III}(TPA).DMF-2 framework with its octahedral diamond-like shape is shown in Figure 4.27. SEM images showed the average length of particles as 429 nm approximately. However, as shown in Figure 4.27a, the particle sizes are non-uniform and presence of very small particles might be due of insufficient reaction time.

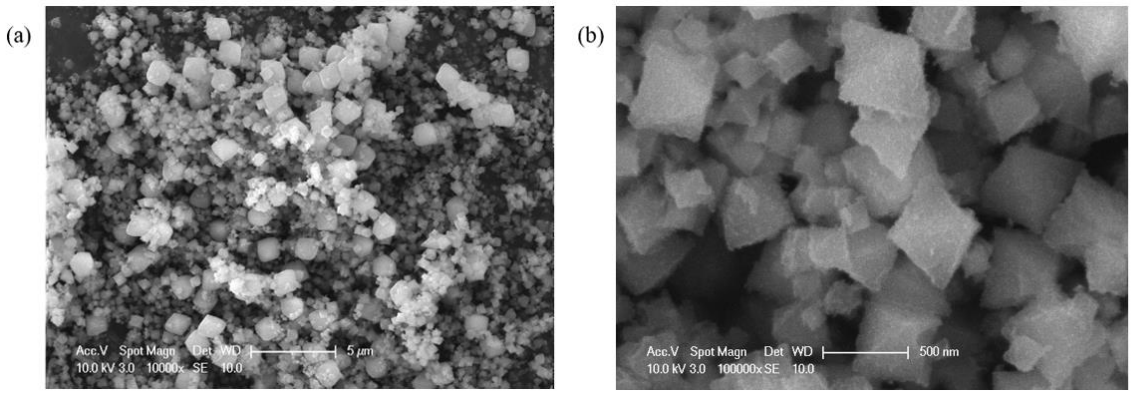


Figure 4.27. SEM images of Fe^{III}(TPA).DMF-2 at (a) 10000x and (b) 100000x zoom level.

Through EDX analysis, C (39.33 w %), O (28.4 w %), Fe (26.65 w %) and Cl (5.62 w %) were detected in the Fe^{III}(TPA).DMF-2 particles. Presence of very little amounts of Cl might be resulted from traces of the $FeCl_3.6H_2O$ precursor due to insufficient washing process through the synthesis.

XRD pattern of Fe^{III}(TPA).DMF-2 is displayed in Figure 4.28. The XRD pattern match well with the pattern of Fe-MOF, MIL-101(Fe), reported in literature [150] which confirms that crystals are well-formed.

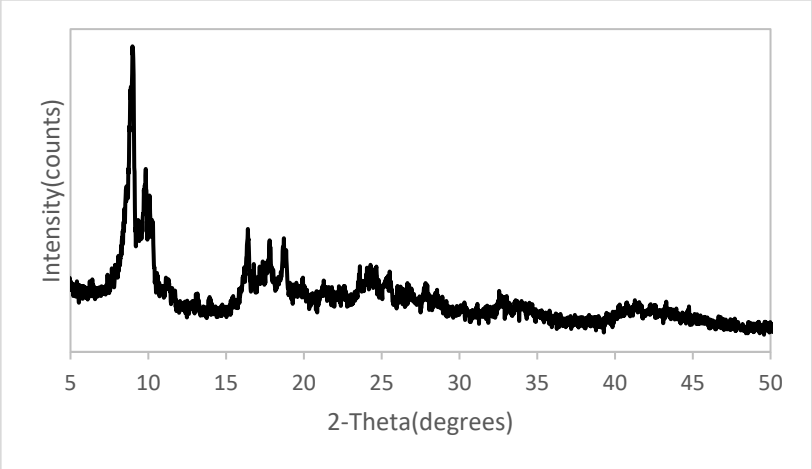


Figure 4.28. XRD Pattern of Fe^{III}(TPA).DMF-2.

Upon increased concentrations of reactants in the same amount of solvent, Fe^{III}(TPA).DMF-1 was expected to yield particles with smaller size. However, Fe^{III}(TPA).DMF-2 particles demonstrated lower particle sizes in average which might be due to the insufficient reaction time for its synthesis procedure since the particle size distribution was non-uniform as can be seen form SEM images. Also, highly different XRD patterns (Figure 4.29) demonstrates formation of different frameworks with different phases are obtained due to the changes in molar ratio and reaction conditions.

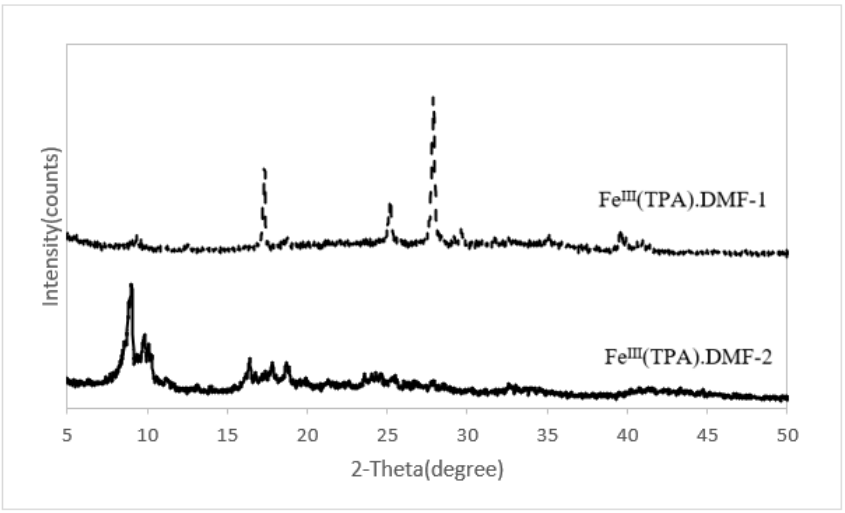


Figure 4.29. XRD Pattern of Fe^{III}(TPA).DMF-1 and Fe^{III}(TPA).DMF-2.

4.3.3. $Fe^{III}(NH_2\text{-}TPA)$.DMF (Fe-MIL-88B) and Co^{II}/ $Fe^{III}(NH_2\text{-}TPA)$.DMF:

$Fe^{III}(NH_2\text{-}TPA)$.DMF: Spindle-shaped, rod like particles of the obtained framework is displayed in Figure 4.30 via SEM imaging. Average particle size of the synthesized $Fe^{III}(NH_2\text{-}TPA)$.DMF was found as 902 nm approximately through SEM images.

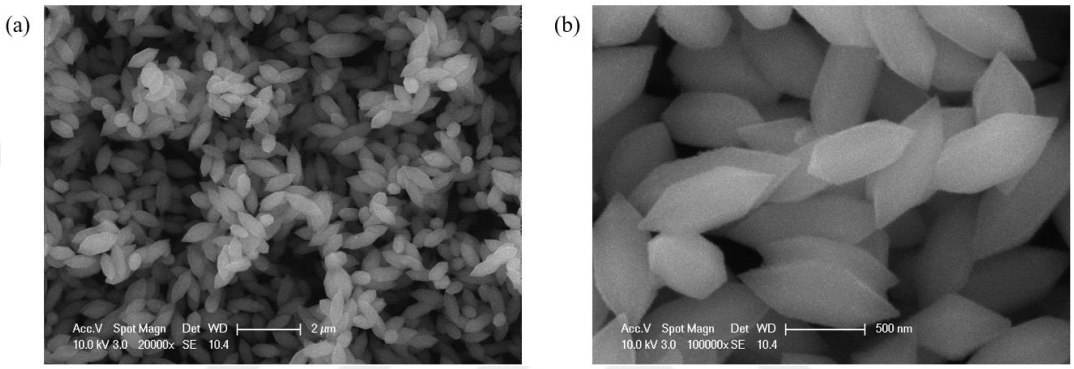


Figure 4.30. SEM images of $Fe^{III}(NH_2\text{-}TPA)$.DMF at (a) 20000x and (b) 100000x zoom level.

C (33.65 w %), O (54.14 w %), Fe (17.49 w %), Zn (9.62 w%), K (0.33 w%), Si (0.43 w%), Cu (0.71 w%) and Cl (14.11 w %) were detected in the Fe^{III}(TPA).DMF-2 particles through EDX analysis. EDX analysis shows that the obtained framework contains impurities such as Si, Cl, K, Cu and Zn which may resulted from the insufficient washing process and the glass equipment used to store the obtained framework.

Crystallographic properties of the Fe-MOF are characterized by XRD analysis of the Fe-MOF (Figure 4.31). Peaks at 2θ values of 9.078°, 10.161°, 12.956°, 16.580°, 18.240°, 20.443°, 24.660°, 29.063° can be attributed to (002), (101), (102), (103), (200), (202), (105), (302) diffraction planes of the framework which match perfectly with peaks of a Fe-MOF, denoted as Fe-MIL-88B according to the literature. Diffraction planes are assigned to the peaks according to the reported Fe-MIL-88B XRD patterns [151–153].

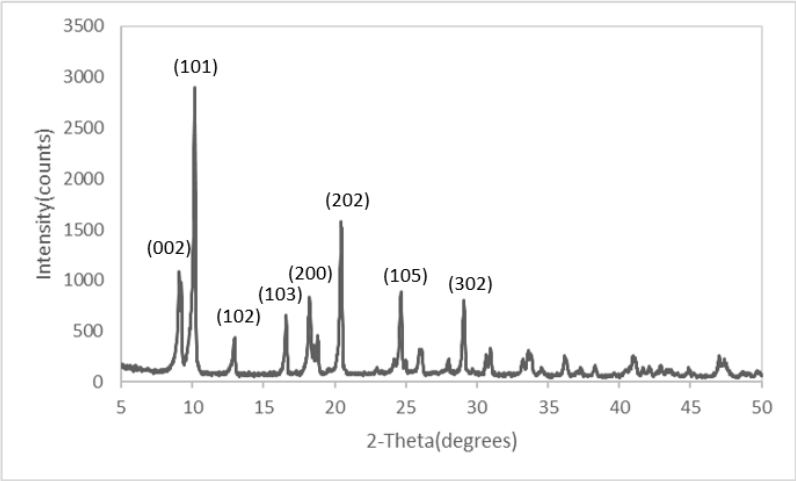


Figure 4.31. XRD pattern of $Fe^{III}(NH_2\text{-TPA}).DMF$.

Co^{II}/ $Fe^{III}(NH_2\text{-TPA}).DMF$-1: Spindle-shaped particles (Figure 4.32) were again obtained through replacement of half of the iron metal ion precursors in $Fe^{III}(NH_2\text{-TPA}).DMF$-1 synthesis procedure with cobalt metal ion precursor.

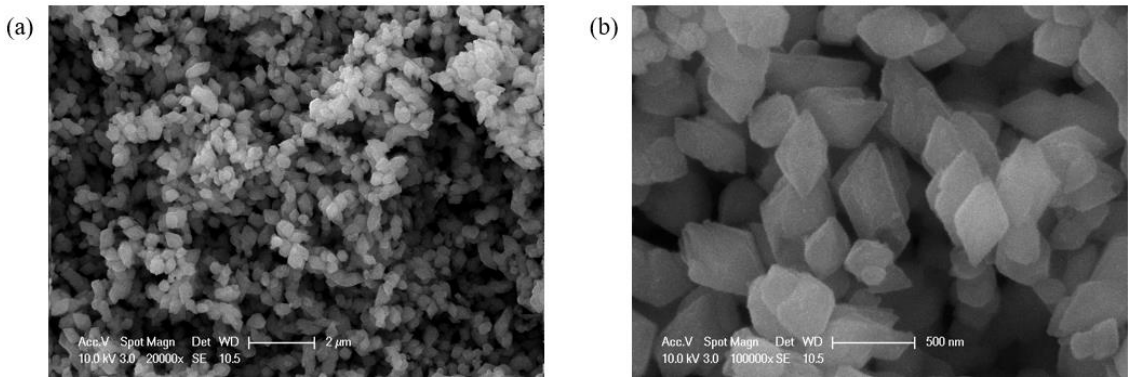


Figure 4.32. SEM images of Co^{II}/ $Fe^{III}(NH_2\text{-TPA}).DMF$-1 at (a) 20000x and (b) 100000x zoom level.

Through the EDX analysis, C (45.27 w %), O (42.21 w %), Fe(10.89 w %), Co (0.77 w%) and Cl (0.86 w %) were detected in the $Co^{II}/Fe^{III}(NH_2\text{-TPA}).DMF$-1 framework. Presence of very little amounts of Cl might be resulted from traces of the $FeCl_2.6H_2O$ precursor due to insufficient washing process through the synthesis. Also, due to high

affinity of carboxylates in NH_2-TPA or Fe (III) and the strength of the Fe-O bonds formed, EDX analysis demonstrates that a relatively little amount of Co was integrated into the bimetallic MOF than intended [151].

XRD pattern of the synthesized framework is demonstrated in Figure 4.33. Characteristic peaks appeared around 2θ values of 9.297°, 10.199°, 13.015°, 16.641°, 18.201°, 18.623°, 20.458°, 24.580°, 25.901°, 26.157°, 27.923°, 28.982°, 30.896°, 33.064°, 33.760°, 36.060°, 38.200°, 41.156°, 46.900°, 47.318°, 47.657° again. These peaks can be attributed to diffraction planes of (002), (101), (102), (103), (200), (202), (105), (302) respectively just like Fe^{III}(NH_2-TPA).DMF [151–153].

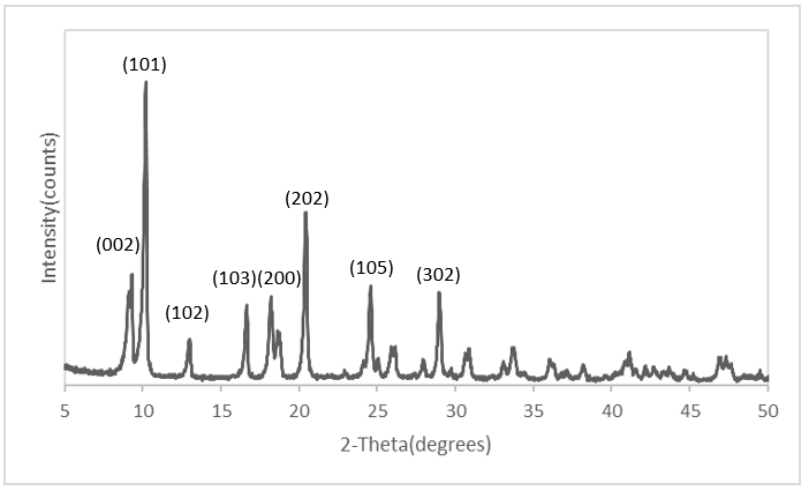


Figure 4.33. XRD pattern of Co^{II}/ Fe^{III}(NH_2-TPA).DMF.

Also, as can been seen from the XRD pattern of single metal and Co-doped Fe^{III}(NH_2-TPA).DMF frameworks in Figure 4.34, replacement of half of the iron metal ion source with cobalt did not disrupt the framework and the XRD pattern confirms that the Fe^{III}(NH_2-TPA).DMF structure is retained through addition of second metal ion.

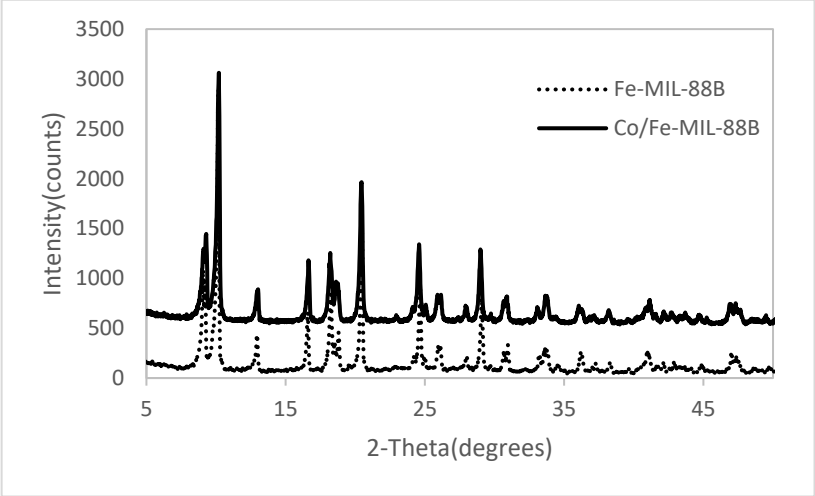


Figure 4.34. XRD patterns of $Fe^{III}(NH_2\text{-TPA})$.DMF (Fe-MIL-88B) an Co^{II}/ $Fe^{III}(NH_2\text{-TPA})$.DMF (Co/Fe-MIL-88B).

4.4. Characterization of Prepared Electrodes

4.4.1. SSMs Coated with Carbon Slurries

4.4.1.1. SSMs Coated with Binder-Free Coating. SSMs are coated with carbon materials without any addition of polymer binders only using ethanol as solvent. However, due to absence of a binder material, the coating did not cover the SSM surface and most of the coatings were peeled off. Conductivities of the bare mesh and the mesh with the CB coating is displayed in Table 4.1.

Table 4.1. Conductivities of SSM before and after coating with binder- free carbon slurry.

SSM	Uncoated SSM (S/m)	Coated SSM (S/m)
SSM #1	1.89×10^4	1.99×10^4

CV plot of the SSM #1, coated with CB without a binder, demonstrates no distinctive peaks when purged with oxygen that could have been interpreted as an oxygen reduction peak (Figure 4.35).

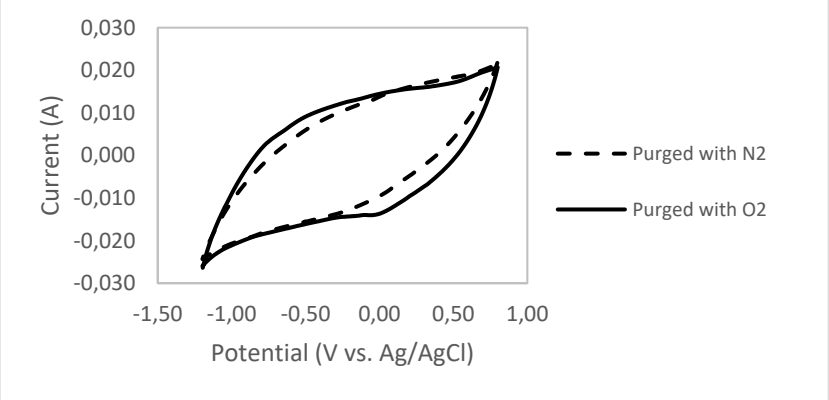


Figure 4.35. CV of coated SSM #1 in N_2 and O_2 purged PB medium at mV/s scan rate.

4.4.1.2. SSMs Coated with PVA Binder Containing Carbon Slurries. Electrochemical characterization for SSMs that are coated with CB or GO with use of PVA as binder polymer are done by chronopotentiometry and cyclic voltammetry measurements. Calculated conductivity values are listed in Table 4.2.

Table 4.2. Conductivities of SSMs before and after coating with carbon and PVA binder containing slurries.

SSMs	Uncoated SSM (S/m)	Coated SSM (S/m)
SSM #2	1.17×10^5	1.95×10^5
SSM #3	9.14×10^4	1.50×10^5
SSM #4	1.60×10^4	9.05×10^4

SSM #2 (90% CB / 10% PVA): SEM images showing the morphology of the coating is displayed in Figure 4.36.

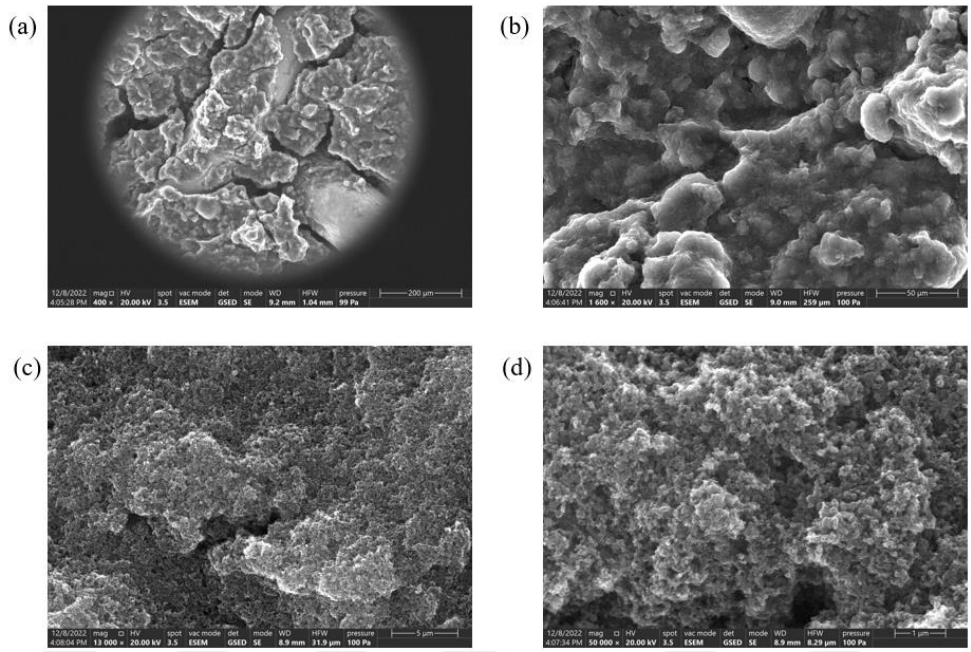


Figure 4.36. SEM images of the coated SSM, SSM #2, at (a) 400x, (b) 1600x, (c) 13000x and (d) 50000x zoom level.

CV plot of SSM #2 in Figure 4.37 displays oxidation and reduction peaks whose intensity is higher when the PB medium is purged with oxygen rather than nitrogen gas. However, peak intensities are low which might be due to poor electrocatalytic activity of the coating towards ORR.

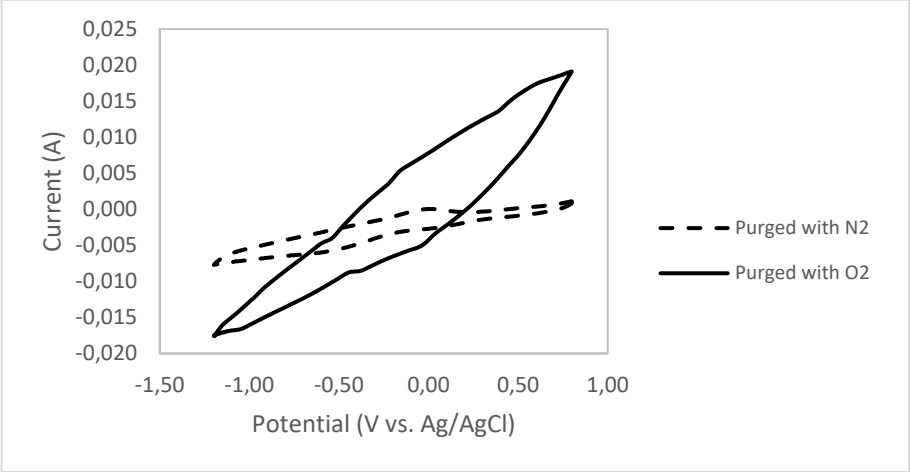


Figure 4.37. CV plot of the coated SSM, SSM #2, in N_2 and O_2 purged PB medium at 100 mV/s scan rate.

SSM #3 (90% CB / 10% PVA): CV plot of SSM #3, SSM coated with 90% CB / 10% PVA by solid weights, is displayed in Figure 4.38. There are no distinctive oxidation and reduction peaks observed for both experiments when the medium was purged with nitrogen and oxygen.

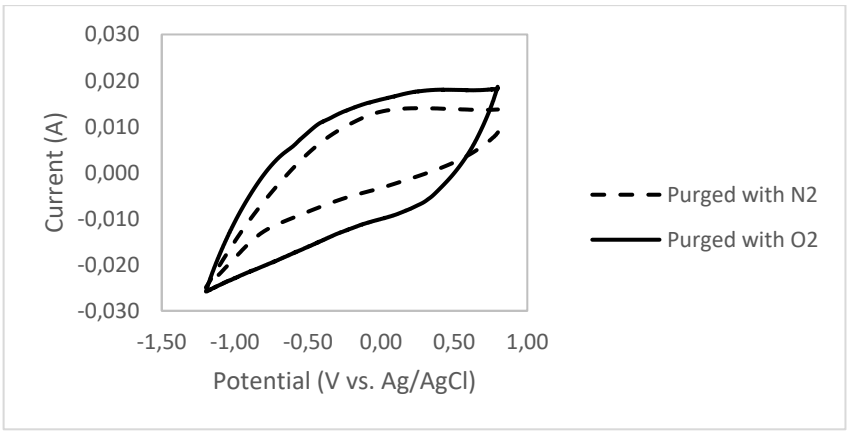


Figure 4.38. CV plot of the coated SSM, SSM #3, in N_2 and O_2 purged PB medium at 50 mV/s scan rate.

SSM #4 (90% GO /10% PVA): CV plot shows a very slight increase in the intensities of reduction and oxidation peaks when the electrolyte solution is purged with oxygen than

nitrogen (Figure 4.39).There are still redox peaks present even the solution is purged with nitrogen which might be due to insufficient N_2 purging to the system and presence of oxygen in the medium still.

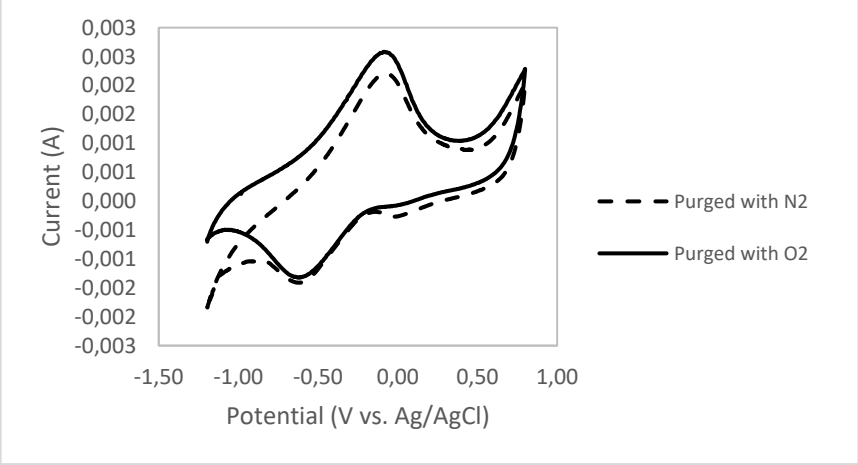


Figure 4.39. CV plot of the coated SSM, SSM #4, in N_2 and O_2 purged PB medium at 100 mV/s scan rate.

The oxidation and reduction peak intensities are increased with increasing scan rates through the CV experiments (Figure 4.40) as expected since the current generated is proportional to the scan rate.

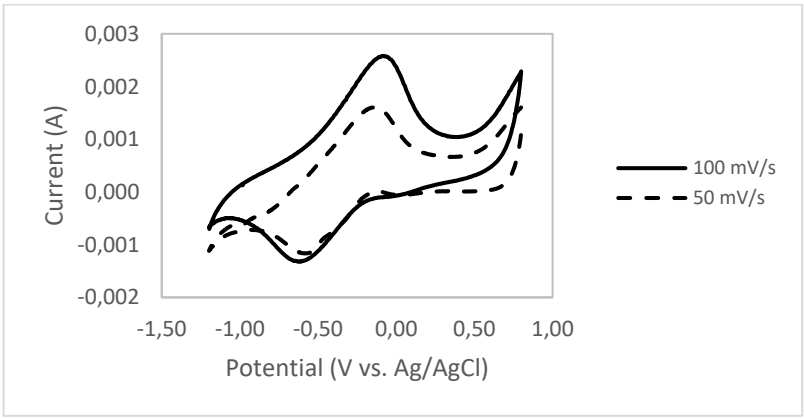


Figure 4.40. CV plot of the coated SSM, SSM #4, in O_2 purged PB medium at 50 and 100 mV/s scan rates.

Effect of carbon source in the slurry used for coating the SSM is examined between SSM #2 (CB-PVA) and SSM #4 (GO-PVA) as well as with SSM #3 (CB-PVA) and SSM #4 (GO-PVA) (Figure 4.41 and Figure 4.42). Each sample only contain carbon source as active material and show small oxygen reduction peak. The reduction peak is more distinctive in SSM #4, the one containing GO, compared to the ones prepared with CB. However, the current response for the coating done with GO containing slurry is very much smaller than of the ones created with CB containing slurries which might be due to increased resistance in the GO coated electrode, SSM #4.

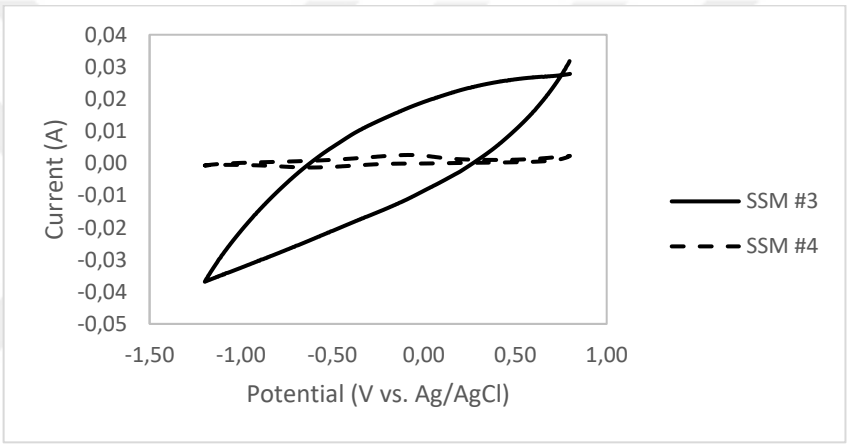


Figure 4.41. CV plot of the coated SSMs, SSM #3 and SSM #4, in oxygen purged PB medium at 100 mV/s scan rate.

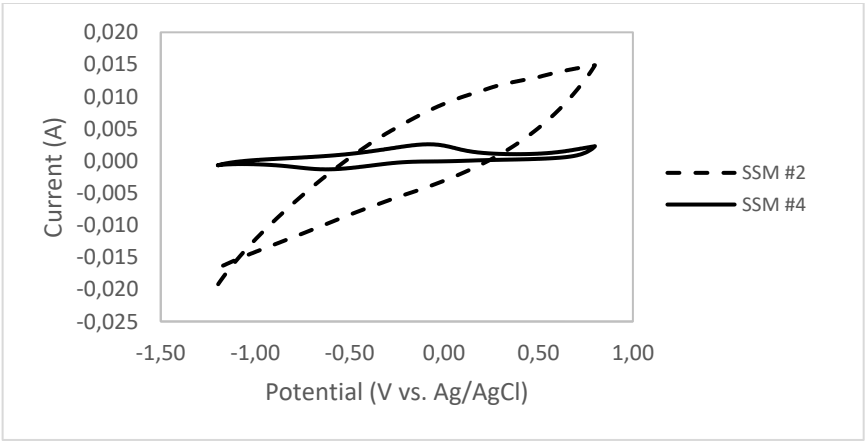


Figure 4.42. CV plot of the coated SSM, SSM #2 and SSM #4, in oxygen purged PB medium at 100 mV/s scan rate.

4.4.4. SSMs Coated with MOF Containing Slurries

Electrochemical characterizations are done by chronopotentiometry and CV experiments. Calculated conductivity values of the MOF and MOF-carbon composite coated SSMs are listed in Table 4.3.

Table 4.3. Conductivities of the SSMs before and after coating with MOF-containing slurries.

SSMs	Uncoated SS Mesh (S/m)	Coated SS Mesh (S/m)
SSM#5	4.31×10^4	9.36×10^4
SSM #6	8.42×10^4	1.27×10^5
SSM #7	8.38×10^4	1.28×10^5
SSM #8	8.38×10^4	1.28×10^5
SSM #9	9.46×10^3	1.09×10^4
SSM#10	1.62×10^4	7.48×10^4
SSM#11	8.59×10^4	1.25×10^5
SSM #12	9.46×10^3	1.08×10^5
SSM#13	1.28×10^5	1.65×10^5
SSM#14	8.25×10^4	1.29×10^5
SSM #15	8.38×10^4	1.28×10^5

SSM #5 (75% ZIF-8-3 / 15% CB / 10%PVA): SEM images of the SSM coated with ZIF-8-3 / CB composite is displayed in Figure 4.44. As can be seen from the Figure 4.43a, amount of the coating on the mesh is very little.

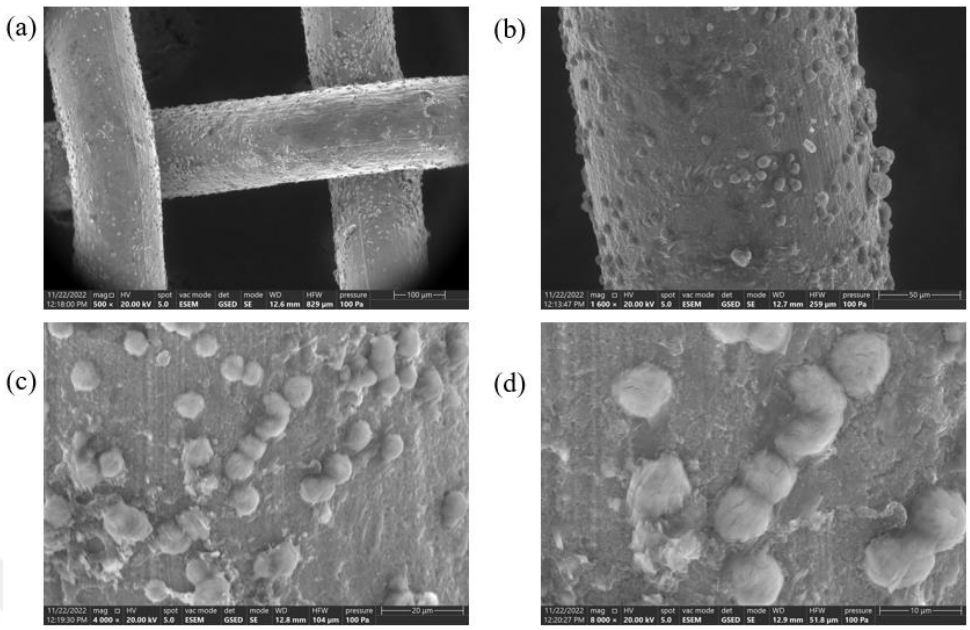


Figure 4.43. SEM images of the coated SSM, SSM #5, at (a) 500x, (b) 1600x, (c) 4000x and (d) 8000x zoom level.

CV plot shows the increased oxygen reduction peak intensity around -0.5 V (Figure 4.44) when the PB medium in which the CV experiment is held is purged with oxygen gas instead of nitrogen.

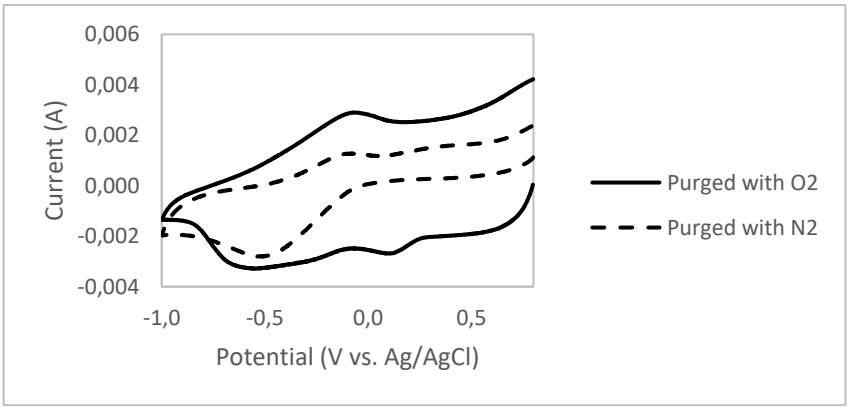


Figure 4.44. CV of the coated SSM, SSM #5, at 100 mV/s scan rate in N_2 and O_2 purged PB medium.

SSM #6 (60% ZIF-L-1 / 30% CB / 10%PVA): SEM images of SSM #6 are displayed in Figure 4.45. As can be seen from the images, the ZIF-L particles with leaf like morphologies stacked together.

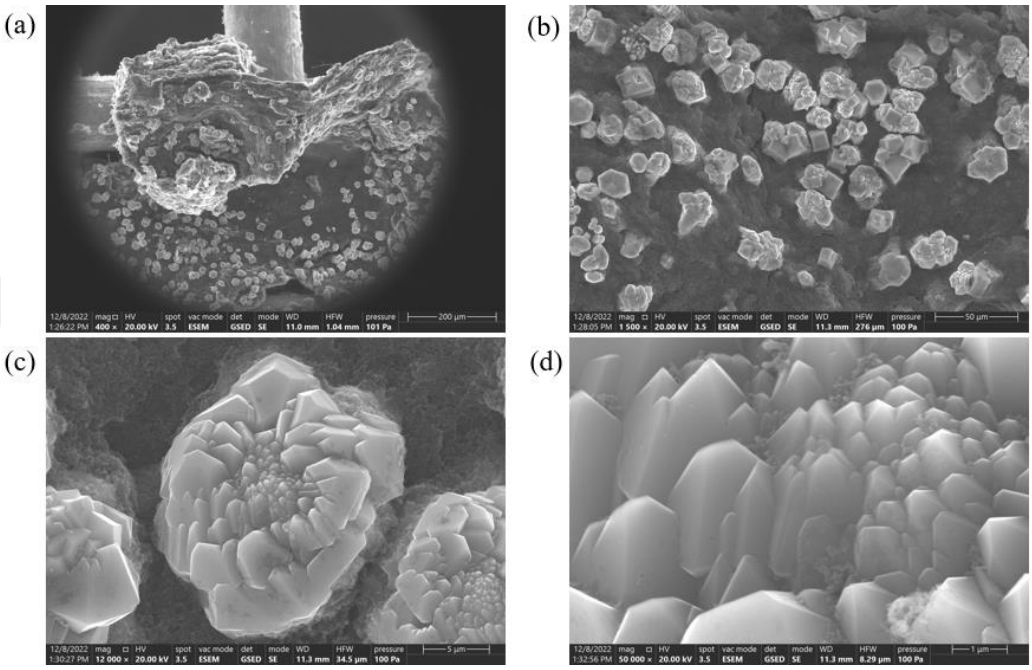


Figure 4.45. SEM images of the coated SSM, SSM #6, at (a) 400x, (b) 1500x, (c) 12000x and (d) 50000x zoom level.

CV plot of SSM #6 shows the highly increased reduction peak intensities at around -0.5V when electrolyte medium is purged with oxygen gas. There is a small peak present as well for the one that is purged with nitrogen gas which might be due to presence of some oxygen in the medium still (Figure 4.46).

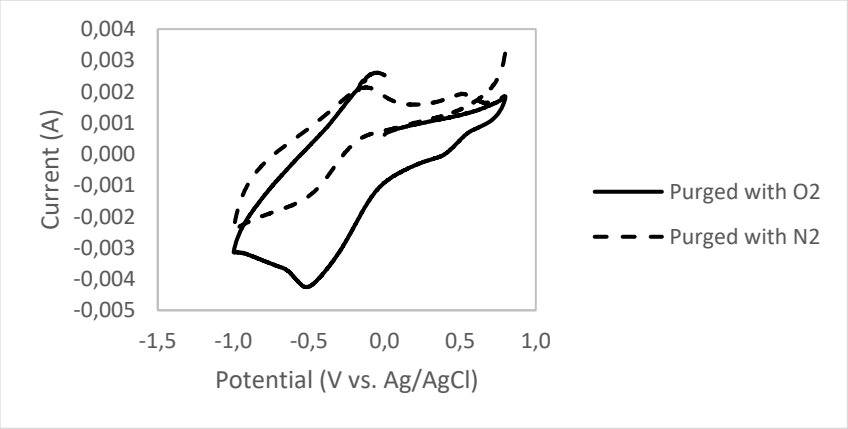


Figure 4.46. CV of the coated SSM, SSM #6, at 100mV/s scan rate in N_2 and O_2 purged PB medium.

As expected, the oxygen reduction peak intensity is increased with increasing scan rate through CV measurements (Figure 4.47) since the current responses in CV is proportional to the scan rate.

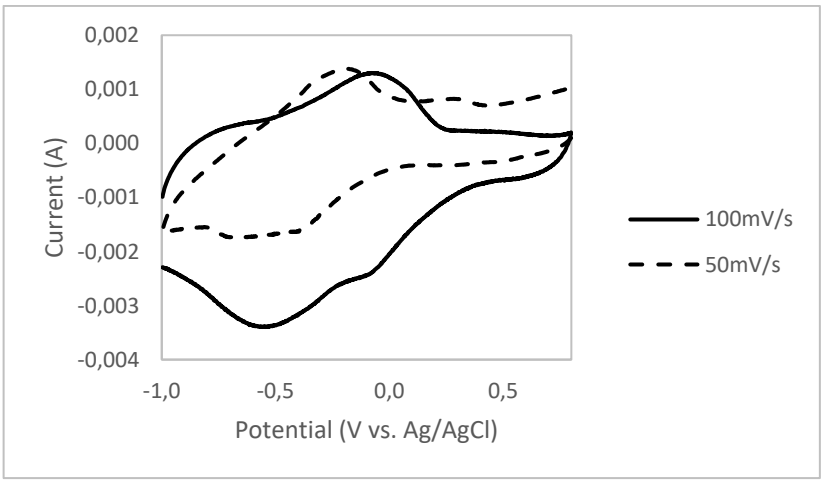


Figure 4.47. CV of the coated SSM, SSM #6, at 50 and 100 mV/s scan rates in PB medium.

SSM #7 (80% ZIF-L / 10% CB / 10% PVA): SEM images showing the morphology of the coating and ZIF-L particles stacked together are displayed in Figure 4.48.

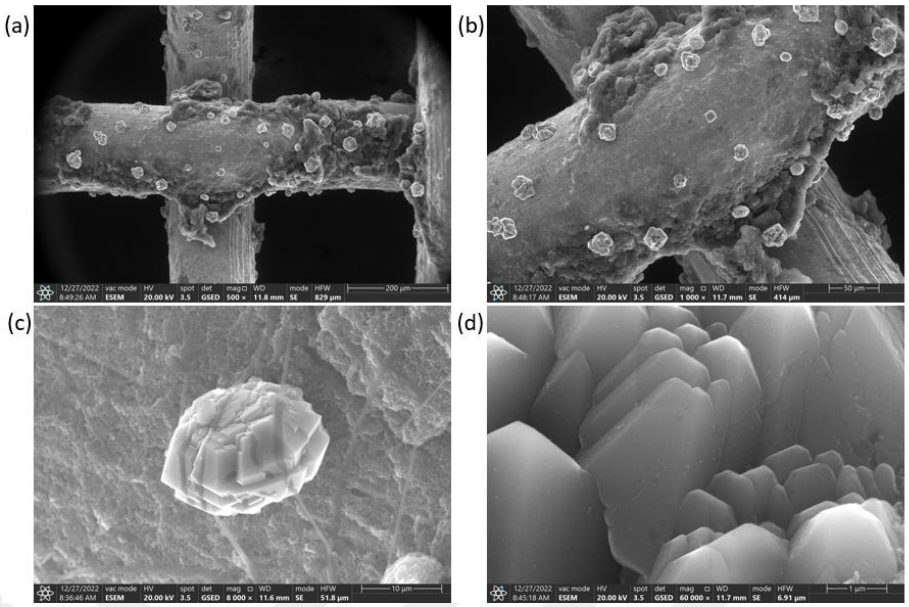


Figure 4.48. SEM images of the coated SSM, SSM #7, at (a) 500x, (b) 1000x, (c) 8000x and (d) 60000x zoom level.

CV plot of current vs. potential is displayed in Figure 4.49 for the SSM #7 that is the mesh coated with ZIF-L /CB composite slurry. When the buffer medium is purged with oxygen instead of nitrogen gas, reduction peak is observed which is the oxygen reduction peak since when the buffer is purged with nitrogen there is not any peak present.

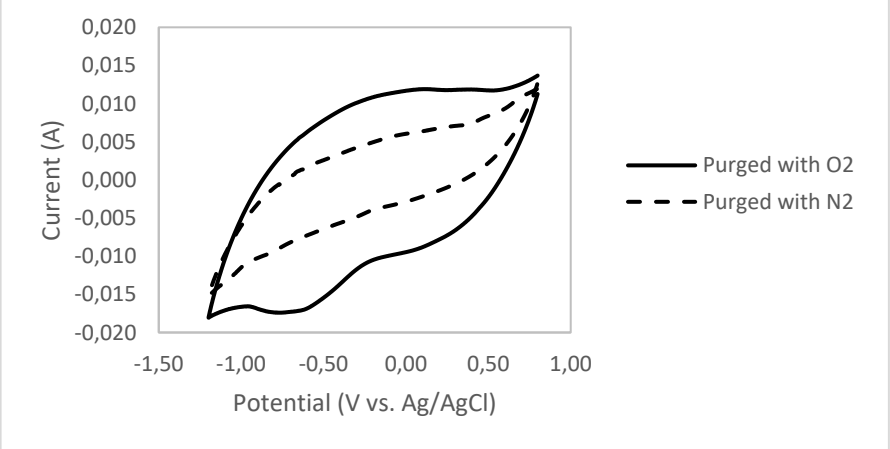


Figure 4.49. CV plot of the coated SSM, SSM #7, at 50mV/s scan rate in N_2 and O_2 purged PB medium.

CV plot of SSM #7 shows increased oxygen reduction peak intensity around -0.65V which is due to presence of Zn-MOF in the coating composition. Whereas SSM #2, SSM coated only with CB demonstrates no distinctive reduction peak (Figure 4.50).

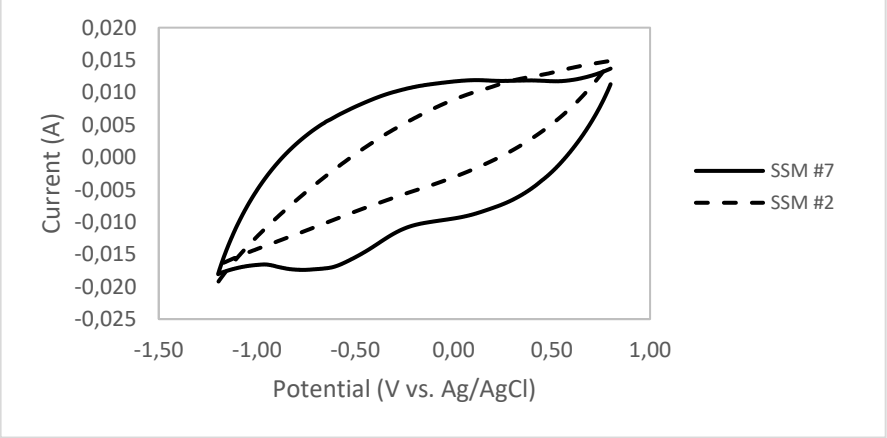


Figure 4.50. CV of the coated SSMs, SSM #7 and SSM #2, at 100mV/s scan rate in N_2 and O_2 purged PB medium.

CV plots of SSM #6 and SSM #7 are displayed in Figure 4.51. SSM #7 shows better electrocatalytic activity than SSM #6 which might be due to higher ratio of ZIF-L-1 in the coated slurry for SSM #7 which enhances the ORR.

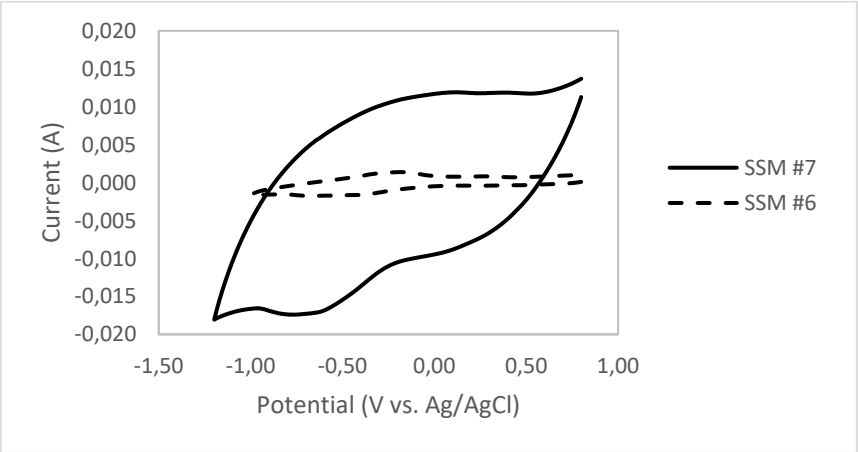


Figure 4.51. CV plot of the coated SSMs, SSM #6 and SSM #7, at 50mV/s scan rate in oxygen purged PB medium.

SSM #8 (ZIF-L-1): SEM images showing the morphology of the coating created by ZIF-L without any addition of binder and CB on SSM is given in Figure 4.52.

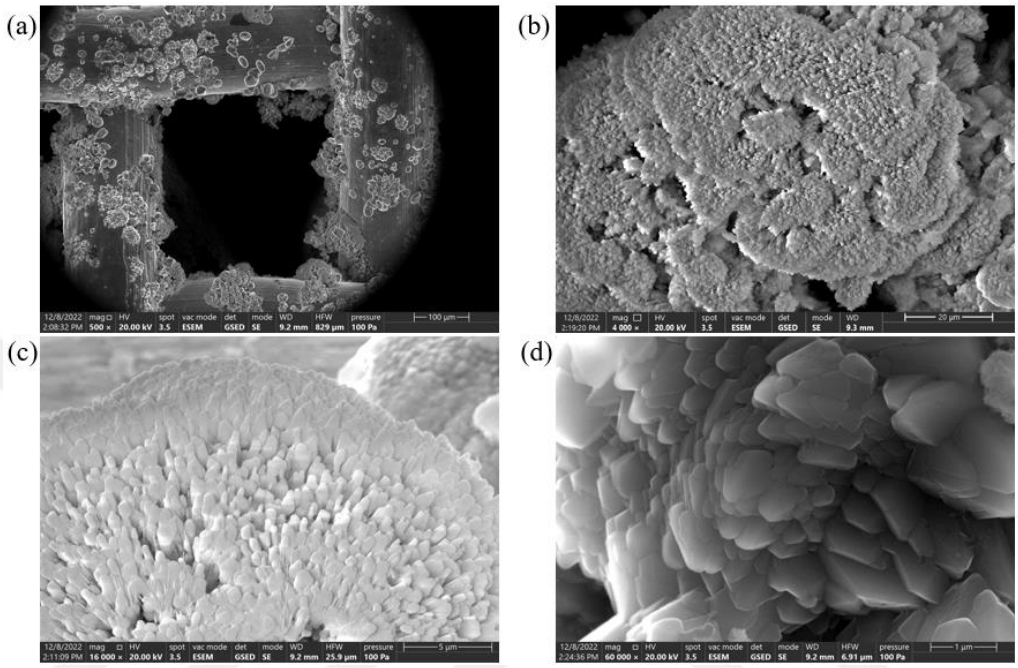


Figure 4.52. SEM images of the coated SSM, SSM #8, at (a) 500x, (b) 4000x, (c) 16000x and (d) 60000x zoom level.

CV plot of SSM #8 demonstrates very small reduction peak intensities for both nitrogen and oxygen purged medium experiments (Figure 4.53). So, the SSM coated with Zn-MOF without any carbon source and binder did not exhibit efficient ORR performance. Presence of terpineol in the coating slurry may hindered the catalytic activity of the coating towards ORR as well as the resistivity of the coated mesh would be higher due to absence of carbon source and addition of terpineol.

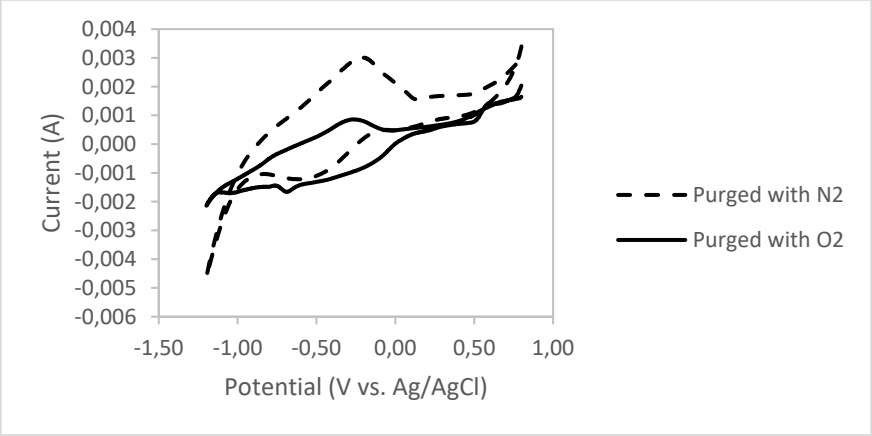


Figure 4.53. CV plot of the coated SSM, SSM #8, at 50mV/s scan rate in N_2 and O_2 purged PB medium.

SSM #9 (80% ZIF-8-1 / 10% CB / 10% PVA): SEM image showing the morphology of SSM coated with ZIF-8 MOF and CB composite is displayed in Figure 4.54.

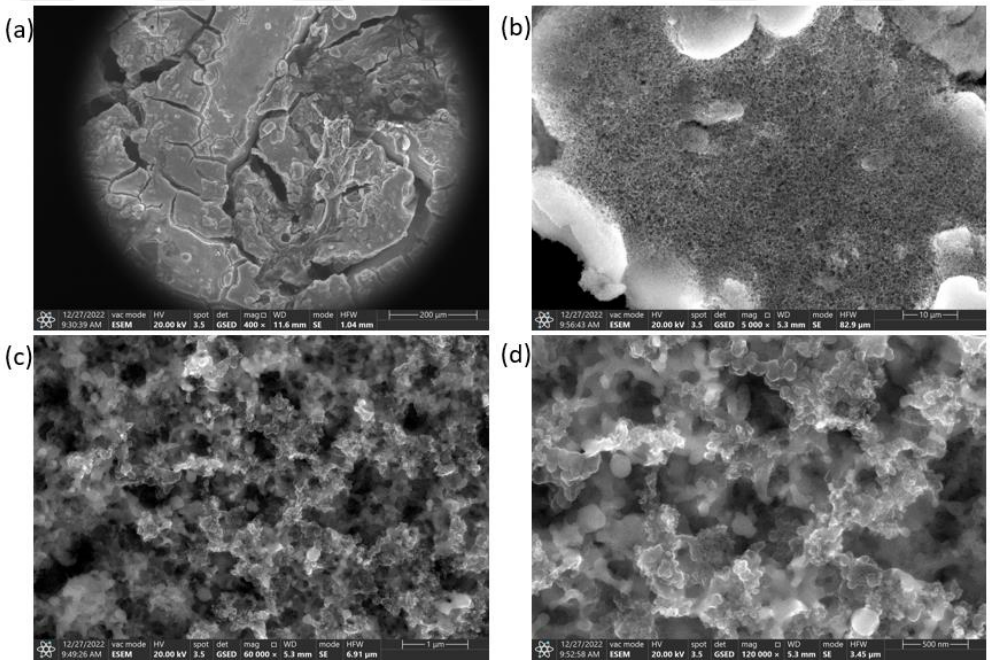


Figure 4.54. SEM image of the coated SSM, SSM #9, at (a) 400x, (b) 5000x, (c) 60000x and (d) 120000x zoom level.

As seen in Figure 4.55, when the electrolyte was purged with oxygen through CV experiment, the reduction peak intensity is highly enhanced for SSM coated with 80% ZIF-8-1 / 10% CB /10%PVA composite. Nitrogen purged medium still exhibits reduction peaks which might be mainly due to presence of remaining oxygen in the electrolyte medium.

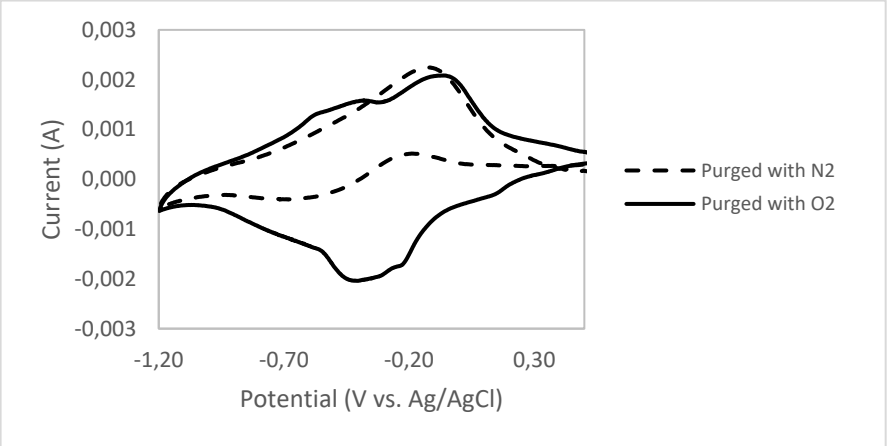


Figure 4.55. CV plot of the coated SSM, SSM #9, at 50mV/s scan rate in N_2 and O_2 purged PB medium.

Current responses in CV plots of SSMs with various Zn-MOFs coatings are normalized with respect to their surface areas and compared in terms of current density vs. potential plot shown in Figure 4.56. SSM #7 (80% ZIF-L-1 / 10% CB / 10% PVA based on weight of solids) showed higher current densities than rest and better electrochemical performance towards ORR.

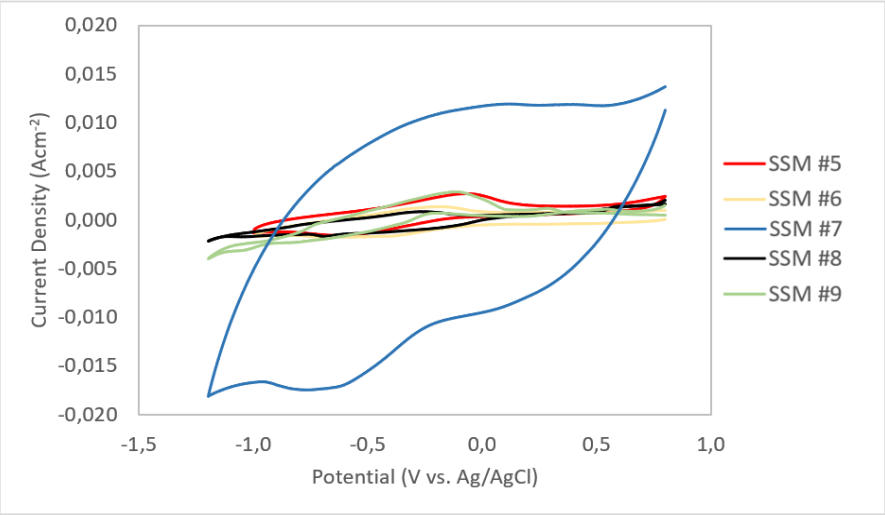


Figure 4.56. CV plot of the SSMs coated with Zn-MOF containing slurries at 50 mV/s scan rate.

SSM #10 (60% Zn-doped ZIF-67-2 / 30% CB / 10% PVA): SEM images of the Zn-doped ZIF-67-2/CB coated SSM is displayed in Figure 4.57.

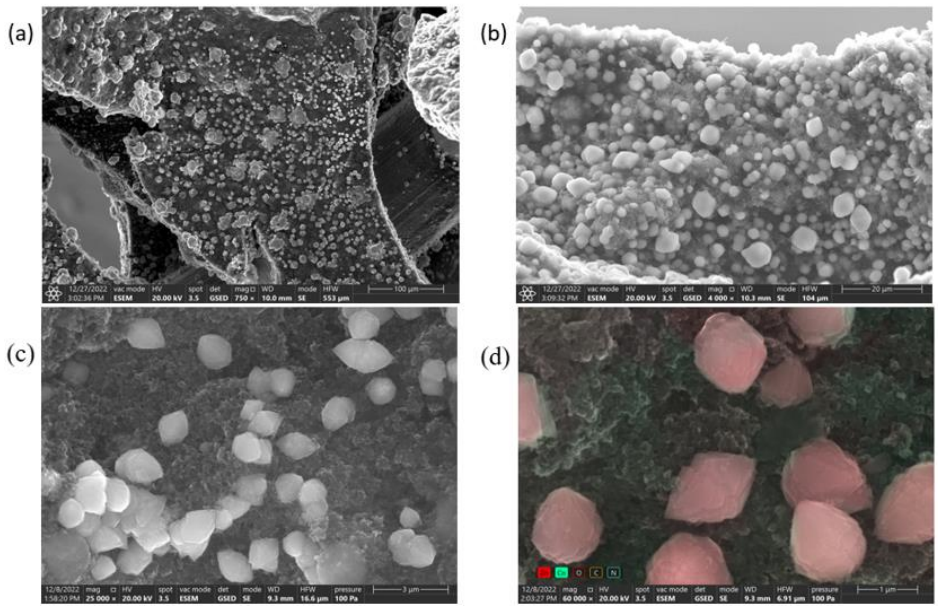


Figure 4.57. SEM images of the coated SSM, SSM #10, (a) 750x, (b) 4000x, (c) 25000x and (d) 60000x zoom level.

CV plot of Zn-doped ZIF-67-2/CB composite coated mesh, SSM #10 is shown in Figure 4.58. The reduction peak appeared around -0.800 V is very little when the electrolyte is purged with N_2 compared to the one that is measured with oxygen purged electrolyte which shows the catalytic activity of the coated mesh towards ORR.

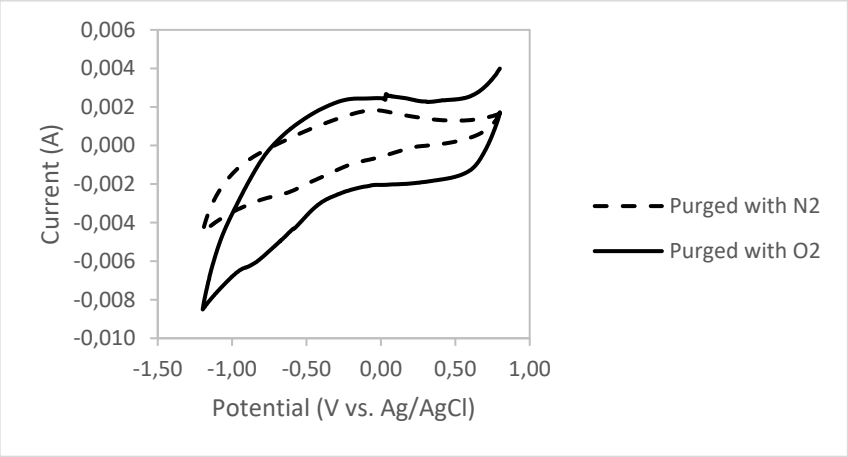


Figure 4.58. CV plot of the coated SSM, SSM #10, at 50 mV/s scan rate in N_2 and O_2 purged PB medium.

SSM #11 (75% Zn-doped ZIF-67-2 / 15% CB 10% PVA): SEM images of the SSM #11 that was prepared with coating of Zn-doped ZIF-67-2/CB composite are displayed in Figure 4.59.

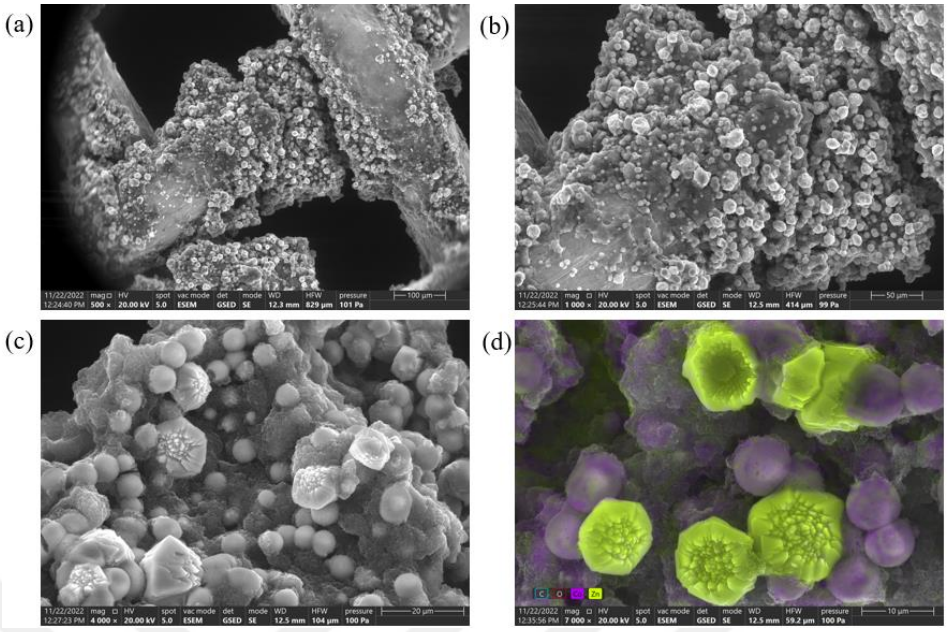


Figure 4.59. SEM images of the coated SSM, SSM #11, at (a) 500x, (b) 1000x, (c) 4000x and (d) 7000x zoom level.

When the electrolyte medium is purged with oxygen, enhanced oxygen reduction peak is observed at -0.60V compared to the medium purged with nitrogen gas (Figure 4.60). Smaller reduction peak for the SSM #11 in nitrogen purged medium displayed very small reduction peak which is due to presence of little amounts of oxygen in the medium.

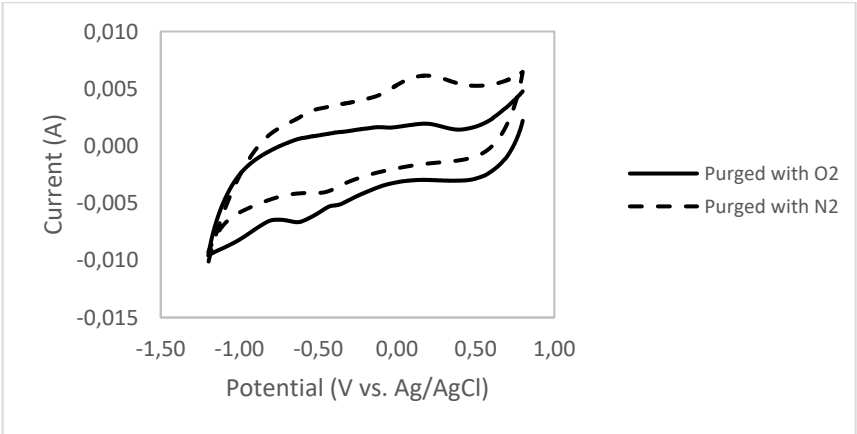


Figure 4.60. CV plot of the coated SSM, SSM #11, at 50 mV/s scan rate in N_2 and O_2 purged PB medium.

When SSM #11 is compared with uncoated SSM and a SSM coated only with CB (SSM #2), it showed better catalytic activity towards ORR as can be seen from Figure 4.61.

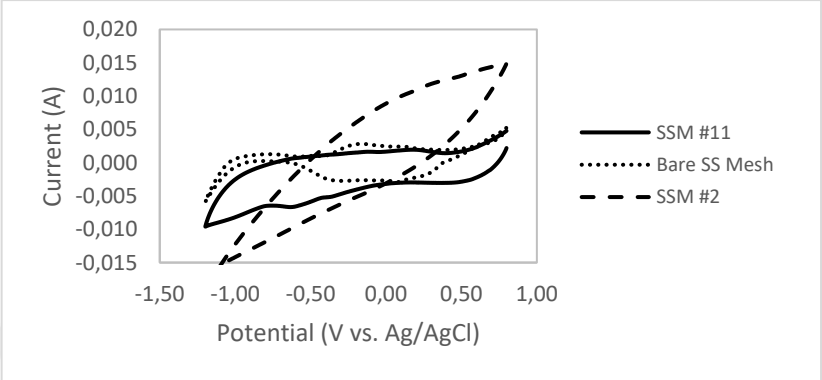


Figure 4.61. CV of the coated SSMs, SSM #11 and SSM #2, and bare SSM at 50 mV/s in oxygen purged PB medium.

SSM #12 (80% ZIF-67-2 / 10% CB / 10% PVA): SEM images of the SSM coated with Co-MOF, ZIF-67 and carbon black composite is shown in Figure 4.62.

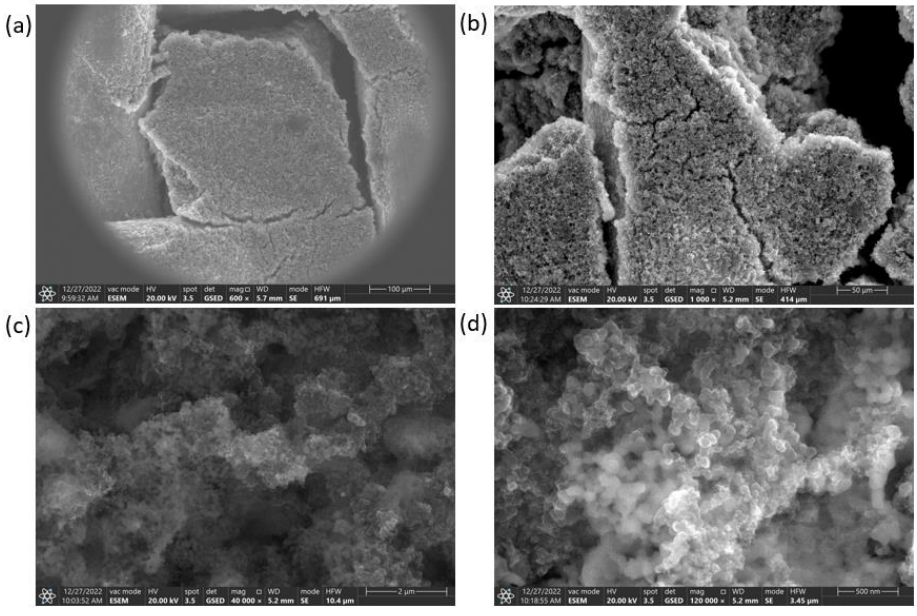


Figure 4.62. SEM images of the coated SSM, SSM #12, at (a) 600x, (b) 1000x, (c) 40000x and (d) 120000x zoom level.

CV plot of SSM #12 demonstrated the oxygen reduction peak around -0.55V which diminishes when the electrolyte medium is purged with nitrogen (Figure 4.63).

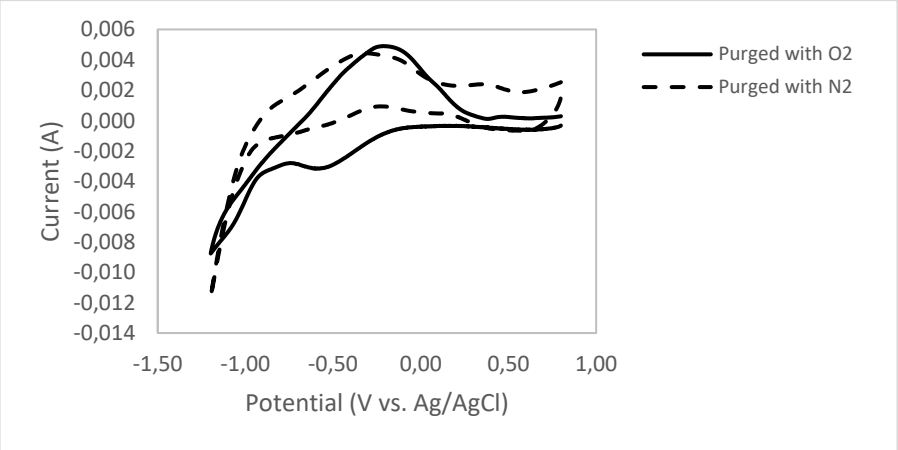


Figure 4.63. CV plot of the coated SSM, SSM #12, at 100mV/s scan rate in N_2 and O_2 purged PB medium.

Current responses in CV plots of SSMs with various Co-MOFs coatings are normalized with respect to their surface areas and compared in terms of current density vs. potential plot as shown in Figure 4.64. SSM #10 and SSM #11 showed better electrochemical performance and increased reduction peak intensities compared to SSM #12. SSM #12 had lower current responses compared to other two, which also correlates with their conductivities reported in Table 3.4. SSM #10 has increased current responses, current densities which is most probably due to synergetic effect created with incorporation of second metal compared to SSM #12, coating with single metallic Co-MOF, ZIF-67-2, and higher amount of conductive CB compared to SSM #11.

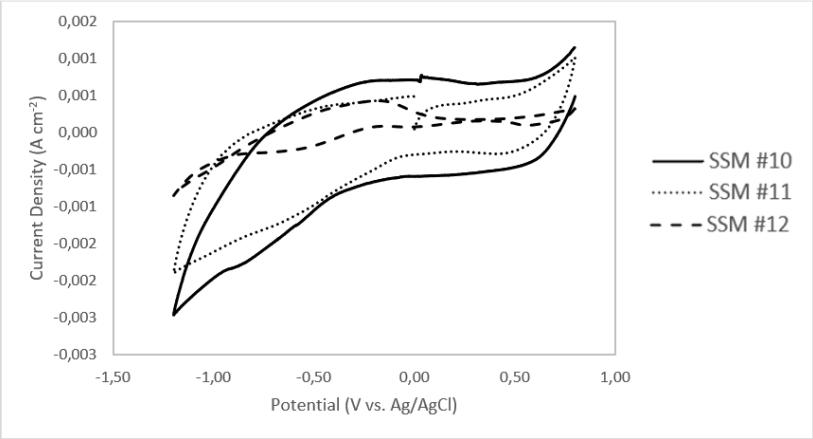


Figure 4.64. CV plot of SSMs coated with Co-MOFs at 50 mV/s scan rate.

SSM #13 (80% MIL-88A-1 / 10% CB / 10% PVA): Morphology of the SSM coated with Fe-MOF composite (80% MIL-88A-1 /10% CB / 10% PVA by weight of solids) is shown in SEM images in Figure 4.65.

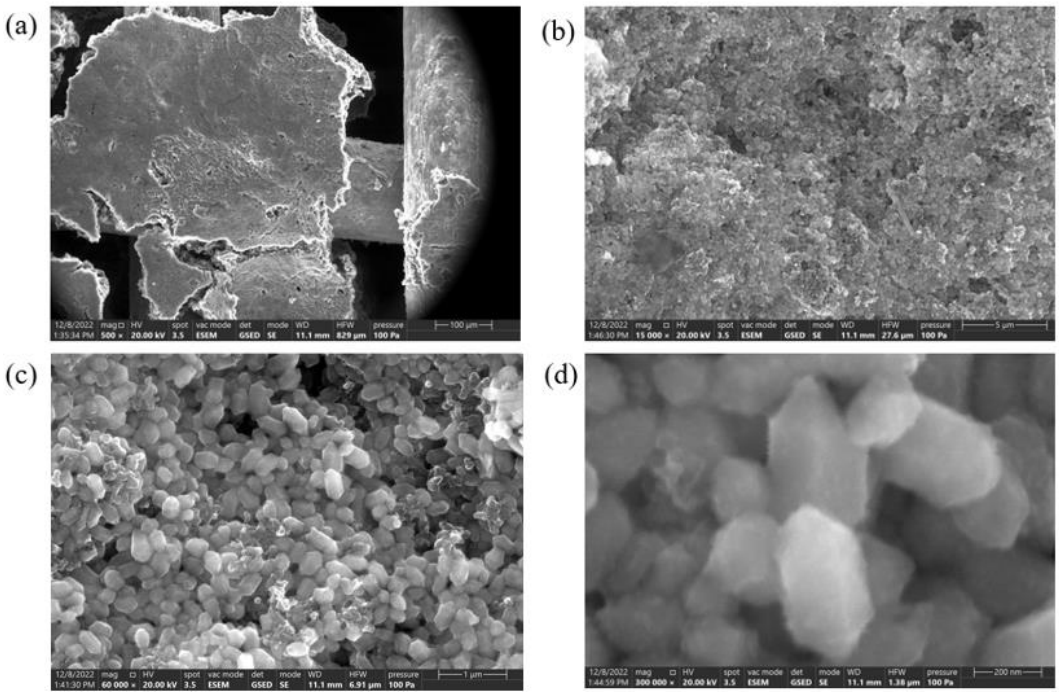


Figure 4.65. SEM images of the coated SSM, SSM #13, (a) 500x, (b) 15000x, (c) 60000x and (d) 300000x zoom level.

CV plot is shown in Figure 4.66 for the SSM #13. When electrolyte was purged with oxygen, the intensity of the reduction peak at -0.47 V is increased compared to the one purged with nitrogen. Oxygen reduction peak is still present in the CV plot of SSM #9 that CV is performed with nitrogen purged electrolyte which is due to presence of oxygen in the medium because of insufficient N_2 purging.

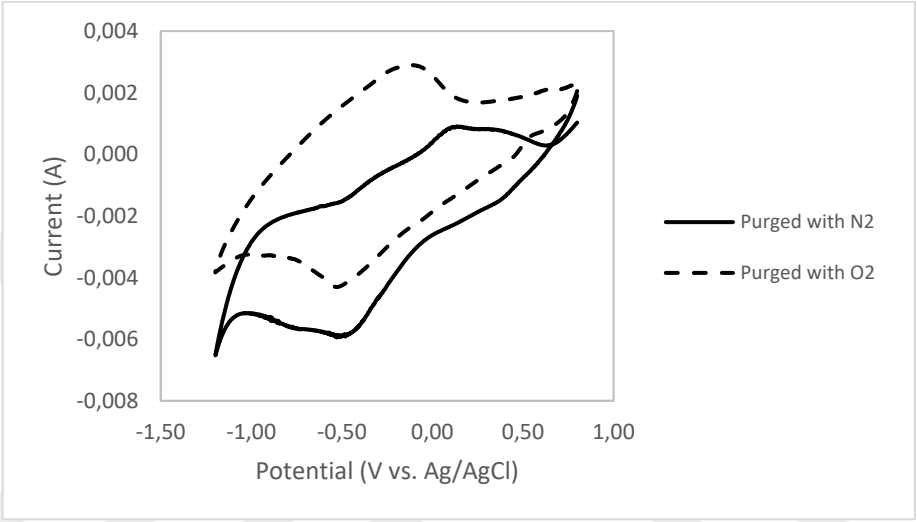


Figure 4.66. CV plot of the coated SSM, SSM #13, at 50mV/s scan rate in PB medium.

To demonstrate the effect of Fe-MOF's presence in the coating, CV plots of SSM #2 (with the coating of 90%CB/10% PVA by weight) and SSM #13 (with the coating of 80% MIL-88A-1/10% CB/10%PVA by weight) were compared in Figure 4.67. Integration of Fe-MOF in the coating slurry resulted in oxygen reduction peak.

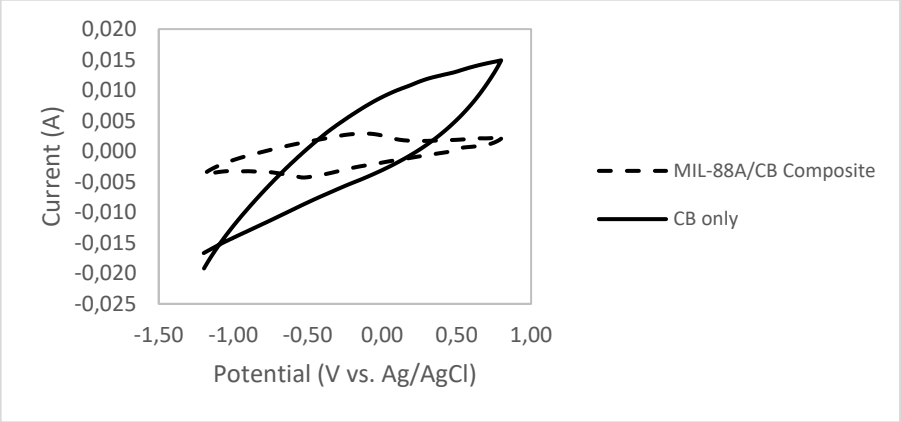


Figure 4.67. CV plot of the coated SSMs, SSM #13 (MIL-88A/ and SSM #2, at 50mV/s scan rate in oxygen purged PB medium.

SSM #14 (32.25% MIL-88A-1 / 68.75% PVA): SEM images showing the morphology of the coating, Fe-MOF (MIL-88A-1) is displayed in Figure 4.68.

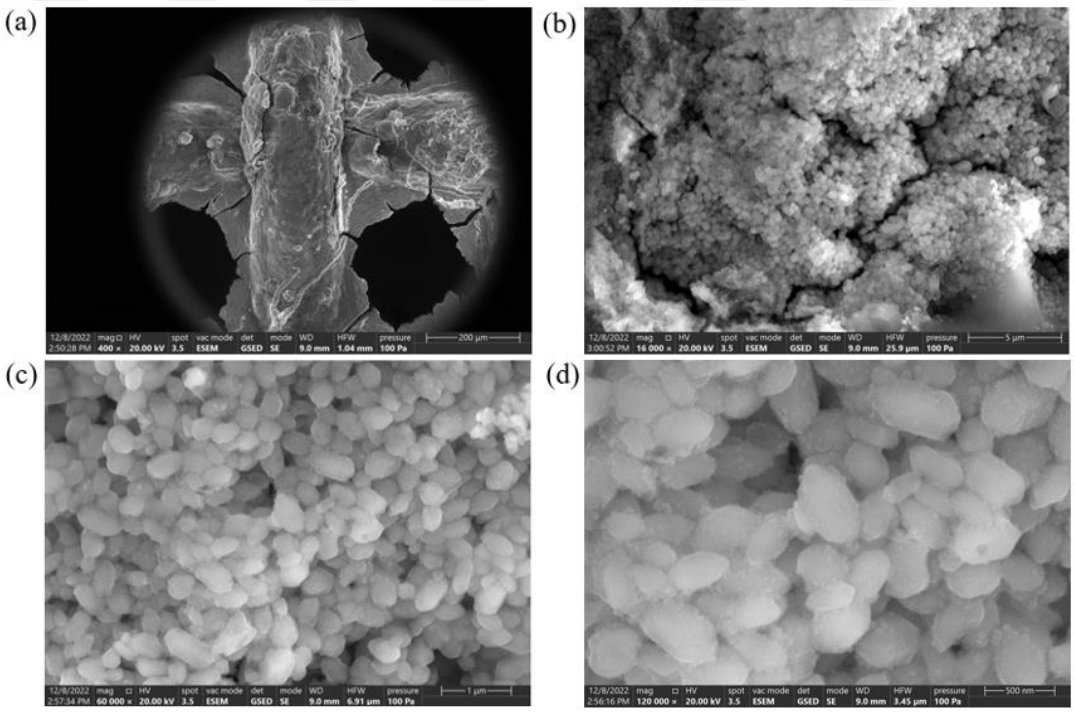


Figure 4.68. SEM images of the coated SSM, SSM #14, at (a) 400x, (b) 16000x, (c) 60000x and (d) 120000x zoom level.

CV plot of SSM #14 shows the good performance of the coated mesh for ORR. As seen in Figure 4.69, when the electrolyte purged with oxygen, the reduction peak intensity is very much higher than the one when the electrolyte is purged with nitrogen. There is still a small reduction when the medium is purged with nitrogen which is mainly due to remaining oxygen in the electrolyte.

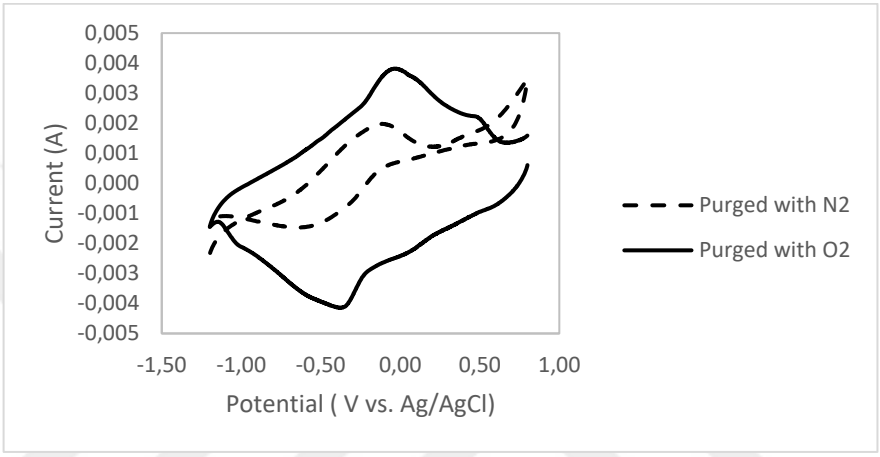


Figure 4.69. CV plot of the coated SSM, SSM #14, at 100 mV/s scan rate in N_2 and O_2 purged PB medium.

SSM #15 (80% Fe-MIL-88B / 10%CB / 10% PVA): SEM images of SSM #15 (SSM with coating of 80% Fe-MIL-88B /10%CB /10% PVA based on weight of solids) is shown in Figure 4.73. Spindle-like shaped Fe-MIL-88B particles retained its morphology upon the coating as well with presence of CB particles as can be seen from Figure 4.70c and d.

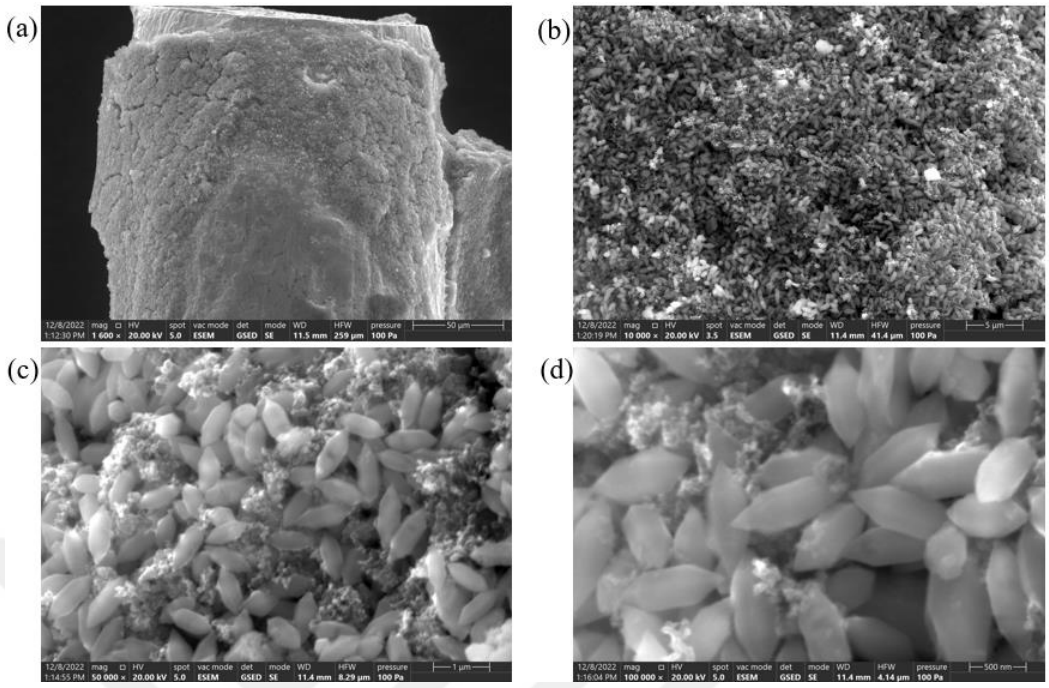


Figure 4.70. SEM images of the coated SSM, SSM #15, at (a) 1600x, (b) 10000x, (c) 50000x and (d) 100000x zoom level.

CV plot of SSM #15 is displayed in Figure 4.71. Upon purging the electrolyte with oxygen, no reduction peak with increased current density is observed and demonstrated reduction peaks are very small which might be due to poor performance of this coated SSM.

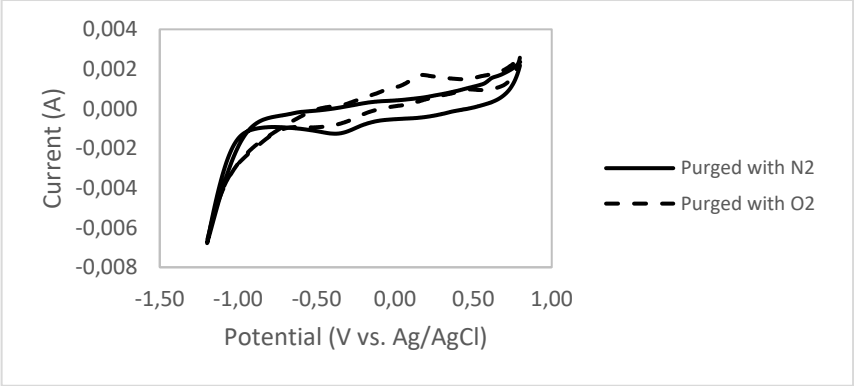


Figure 4.71. CV plot of the coated SSM, SSM #15, at 50mV/s scan rate in N_2 and O_2 purged PB medium.

Current is normalized with respect to the surface areas of SSM cathodes coated with Fe-MOFs and the following CV plot as current density vs. potential is displayed in Figure 4.72. SSM #13 (coating with 80% MIL-88A-1 / 10% CB / 10% PVA by solid weights) showed higher electrochemical activity than SSM #14 (coating with 90% MIL-88A-1 /10% PVA by solid weights) which is due to decreased electrical conductivity of SSM #14 in the absence of CB. Lower current density responses and peak intensities are observed for SSM #15 (coating prepared with 80% Fe-MIL88-B / 10% CB / 10% PVA by solid weights).

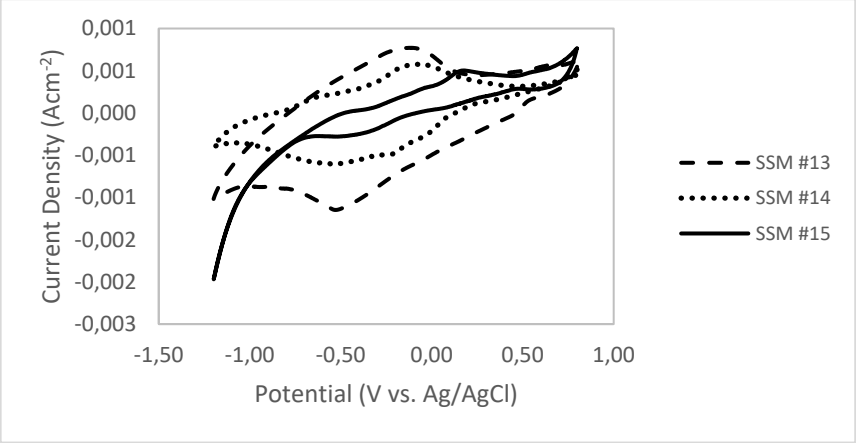


Figure 4.72. CV plots of the SSMs containing Fe-MOFs at 50 mV/s scan rate.

4.5. Performance of SSM Electrodes in MFCs

SSM #2 (90% CB / 10% PVA) was employed as anode due to its conductive nature, electrochemical activity, and physical integrity in terms of coating whereas various MOF and MOF-carbon composite coated SSMs were employed and analysed as cathode electrodes in the constructed MFC. Performance of the cathodes with SSM #2 anode, was evaluated with OCV, LSV and EIS. Both biotic (E. Coli K-12 inoculated) and abiotic (blank, only buffer medium of E.Coli) MFCs were tested to evaluate the E. Coli K-12 catalyzed performance. Current-potential curves obtained from LSV are normalized with respect to cathode surface area.

Images of the Zn-MOF coated SSMs that are employed in MFCs as cathodes are shown in Figure 4.73.

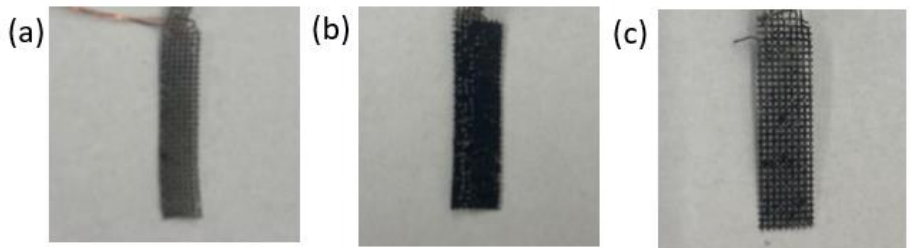


Figure 4.73. Images of the SSM #5, SSM #6 and SSM #7, SSMs coated with Zn-MOFs, employed in MFC analysis.

MFC with SSM #5 (75% ZIF-8-3 / 15% CB / 10% PVA) Cathode: OCV analysis was performed before LSV measurements until stable voltages were obtained. Current density (normalized to cathode surface area) vs. potential curves are displayed in Figure 4.74. As can be seen, through LSV measurements, the higher current density obtained from E.Coli catalyzed MFC using SSM #5 cathode at around -0.8 V. OCV for biotic MFC (E.Coli K-12 inoculated MFC) was obtained around 550 mV, whereas it was around 415 mV for abiotic MFC (MFC without bacteria).

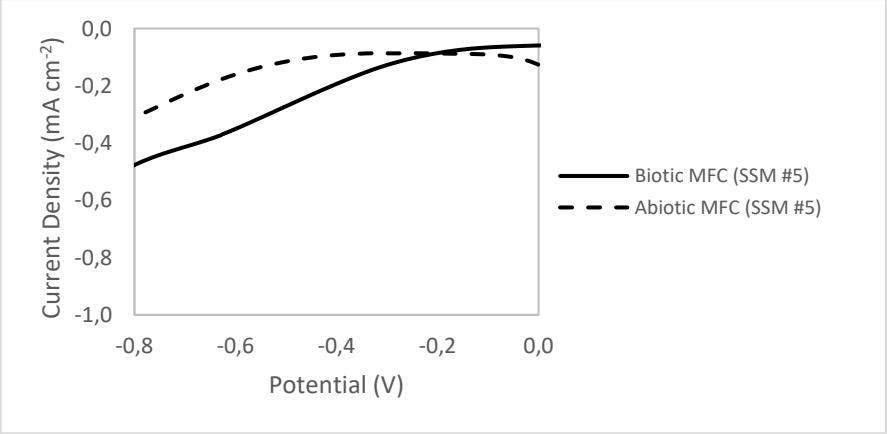


Figure 4.74. Current density vs. potential plot obtained from LSV of MFC with SSM #5.

Nyquist plot obtained from EIS is shown in Figure 4.75. As seen in the inset of the Figure 4.75, MFC with SSM#5 cathode displayed ohmic resistance of 144 ohms and very high charge transfer resistance which is represented via the semicircle of the Nyquist plot.

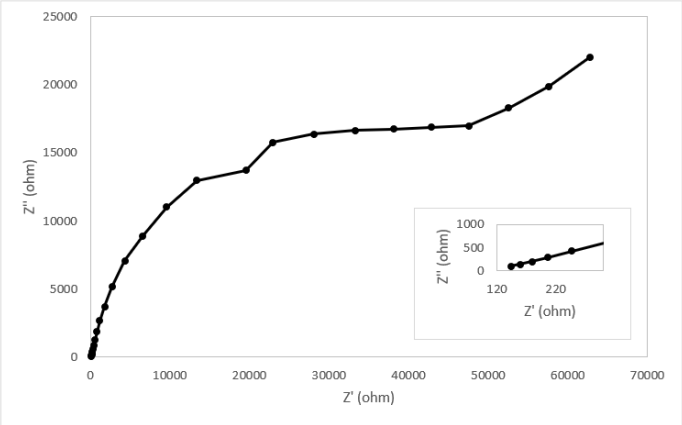


Figure 4.75. Nyquist plot of the MFC with SSM #5 cathode.

Morphology of the SSM #5 before and after MFC application is shown in Figure 4.76. The coating on SSM is retained upon MFC operation and MOF particles retained their structure.

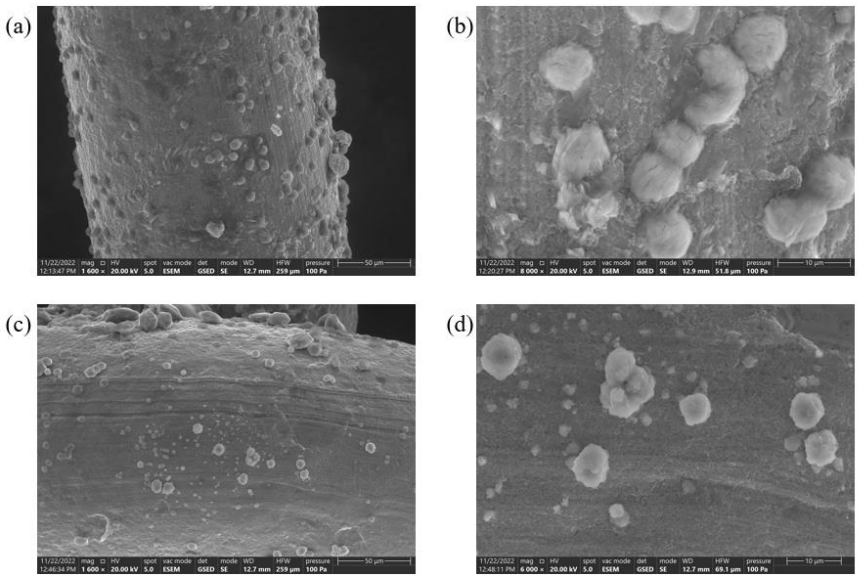


Figure 4.76. SEM images of SSM #5 (a) and (b) before, (c) and (d) after MFC tests.

MFC with SSM #6 (60% ZIF-L-1 / 30% CB / 10%PVA): When Steady potentials were obtained through OCV analysis, LSV measurements were performed. Current density vs. potential curve obtained from LSV is displayed in Figure 4.77. Biotic MFC demonstrated higher current density around -0.7 V than the abiotic MFC with SSM #7 cathode due to E. Coli catalyzed current generation. OCV was 364 mV for biotic MFC and 325 mV for abiotic MFC with SSM #6 cathode.

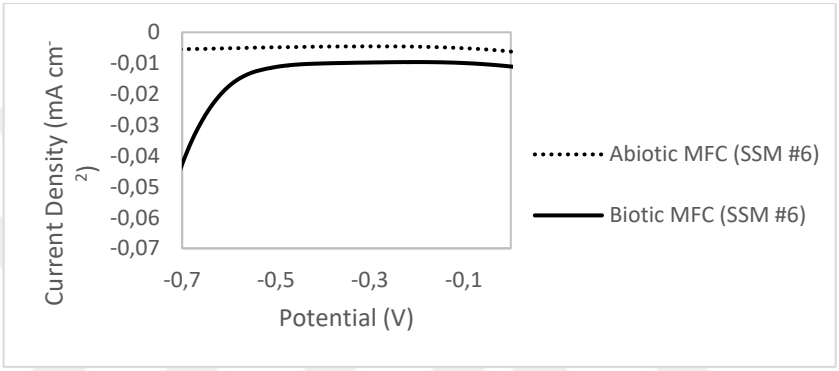


Figure 4.77. Current density vs. potential plot obtained from LSV of MFC with SSM #6.

Nyquist plot obtained from EIS analysis of MFC with SSM #6 cathode is displayed in Figure 4.78. As shown in the inset of the Figure 4.77 below, ohmic resistance is 120 ohms and the charge transfer resistance is very high, approximately 2600 ohm which is seen as the semicircle in the Nyquist plot.

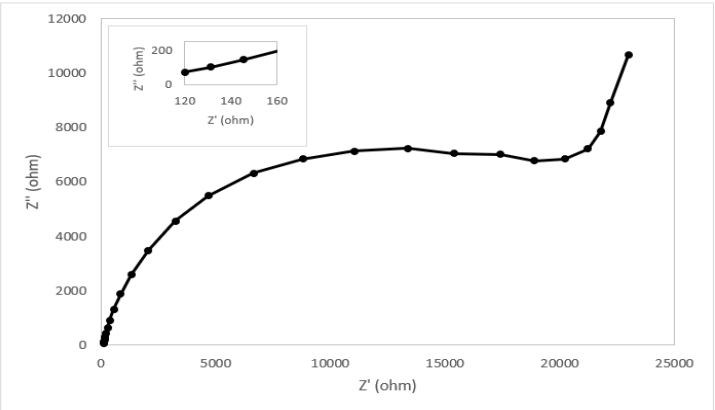


Figure 4.78. Nyquist plot of the MFC with SSM #6 cathode.

SEM images showing the morphology of the coated SSM, SSM #6, is given in Figure 4.79. MOF coating is retained, and structures are not disrupted through the MFC tests.

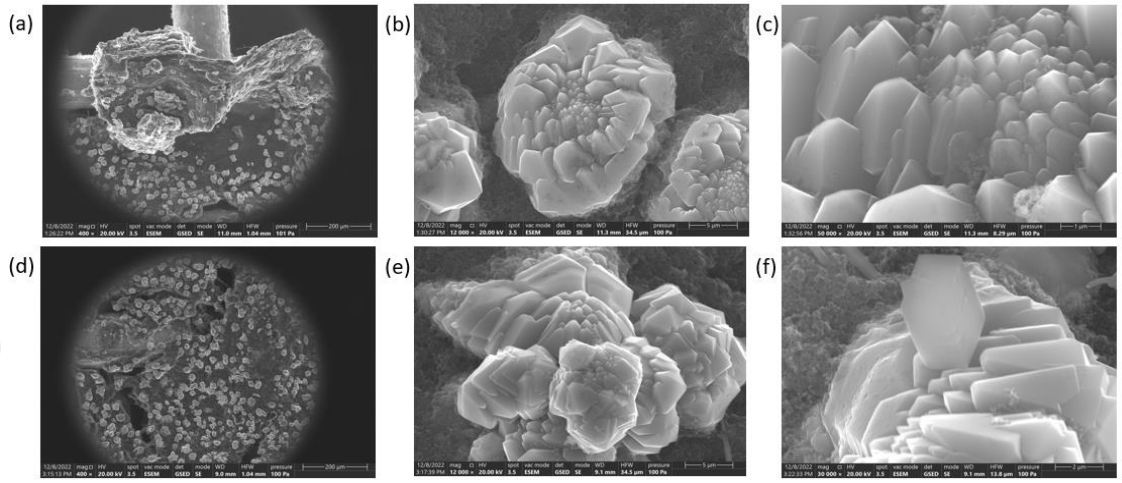


Figure 4.79. SEM images of SSM #6 before (a), (b), (c) and after (d), (e), (f) MFC tests.

MFC with SSM #7 (80% ZIF-L / 10% CB / 10% PVA) Cathode: Current density vs. potential plot obtained from LSV analysis is displayed in Figure 4.80. Higher current density is obtained around -1 V, as can be seen from the Figure 4.80, when E. Coli K-12 was inoculated anodic chamber, showing E. Coli catalyzed current generation. OCV for biotic MFC (E.Coli K-12 inoculated MFC) was obtained as 670 mV and around 800 mV for abiotic MFC (MFC without bacteria) from LSV plot.

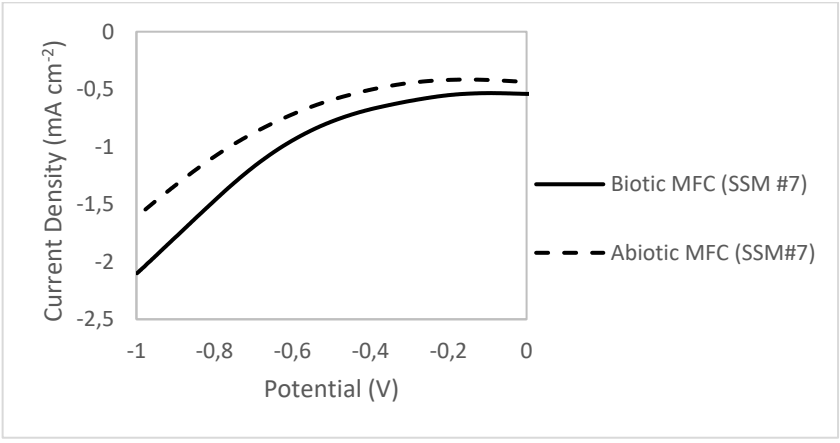


Figure 4.80. Current density vs. potential plot obtained from LSV of MFC with SSM #7.

Nyquist plot obtained from EIS analysis is displayed in Figure 4.81 revealing different resistance parameters regarding the MFC. Ohmic resistance is observed as 41 ohms and the charge transfer resistance, which is represented as the semicircle in the Nyquist plot, is approximately 210 ohms.

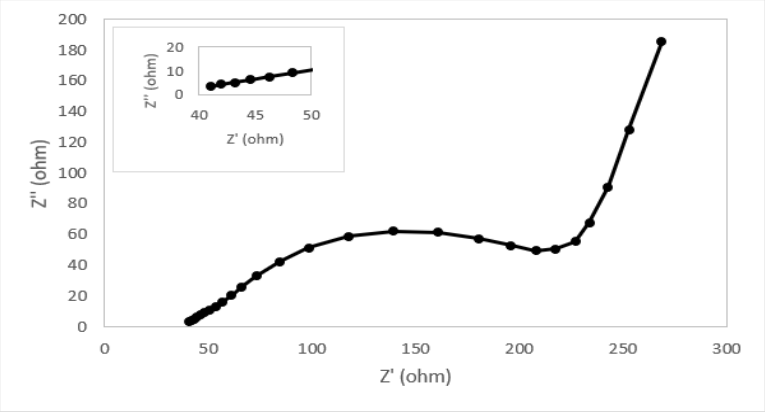


Figure 4.81. Nyquist plot of the MFC with SSM#7 cathode.

SEM images showing the morphology of the coating before and after MFC performance analysis are displayed in Figure 4.82.

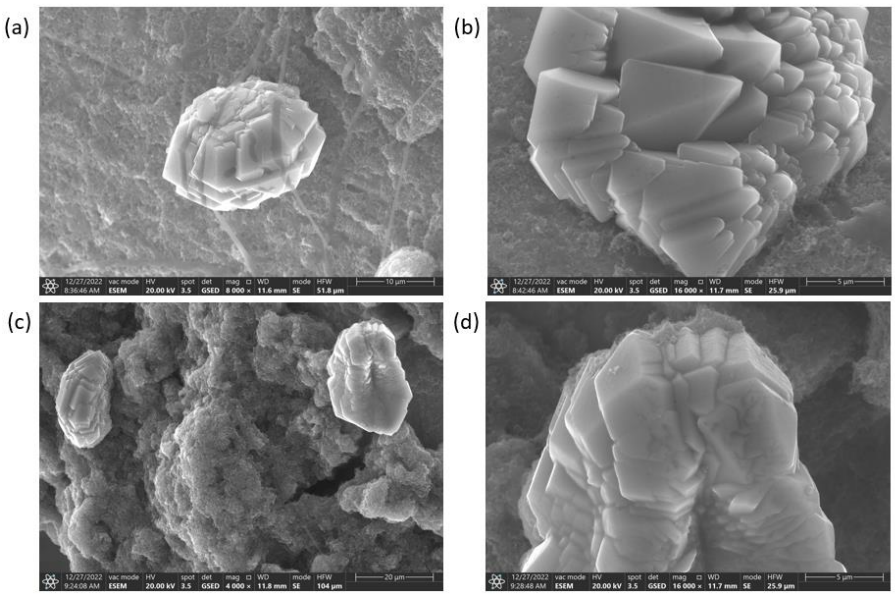


Figure 4.82. SEM images of the SSM #7 (a) and (b) before, (c) and (d) after MFC tests.

Images of the Co-MOF coated SSMs that are utilized in MFCs are shown in Figure 4.83.

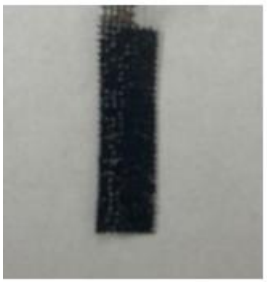


Figure 4.83. Image of the SSM #10, SSM coated with Co-MOF, employed in MFC analysis.

MFC with SSM #10 (60% Zn-doped ZIF-67-2 / 30% CB / 10% PVA) Cathode: After obtaining steady potentials through OCV analysis, LSV measurements were performed. Current density vs. potential plot obtained from LSV is displayed in Figure 4.84. E-Coli K-12 catalyzed current densities are also demonstrated by subtracting the current densities of abiotic MFC from biotic MFC. OCV for biotic MFC (E.Coli K-12 inoculated MFC) was around 670 mV and 186 mV for abiotic MFC (MFC without bacteria).

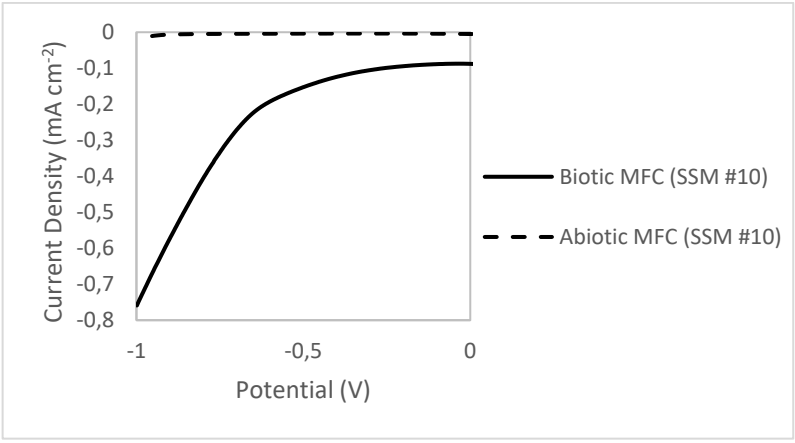


Figure 4.84. Current density vs. potential plot obtained from LSV of the MFC with SSM #10.

Nyquist plot for MFC utilizing SSM #10 cathode was obtained from EIS. The inset of the Figure 4.85 demonstrates the ohmic resistance of the MFC with SSM #10 cathode around 42.3 ohms and by the semicircle of the Nyquist plot, charge transfer resistance is obtained as approximately 450 ohms.

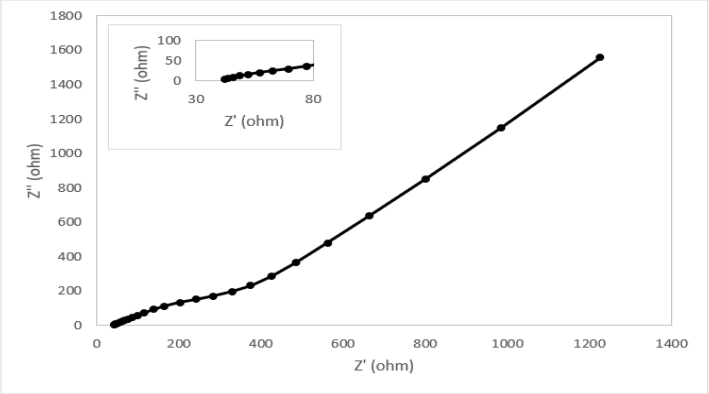


Figure 4.85. Nyquist plot MFC with SSM #10 cathode.

SEM images demonstrating the morphologies of SSM #10 before and after the electrochemical analysis in MFCs are shown in Figure 4.86.

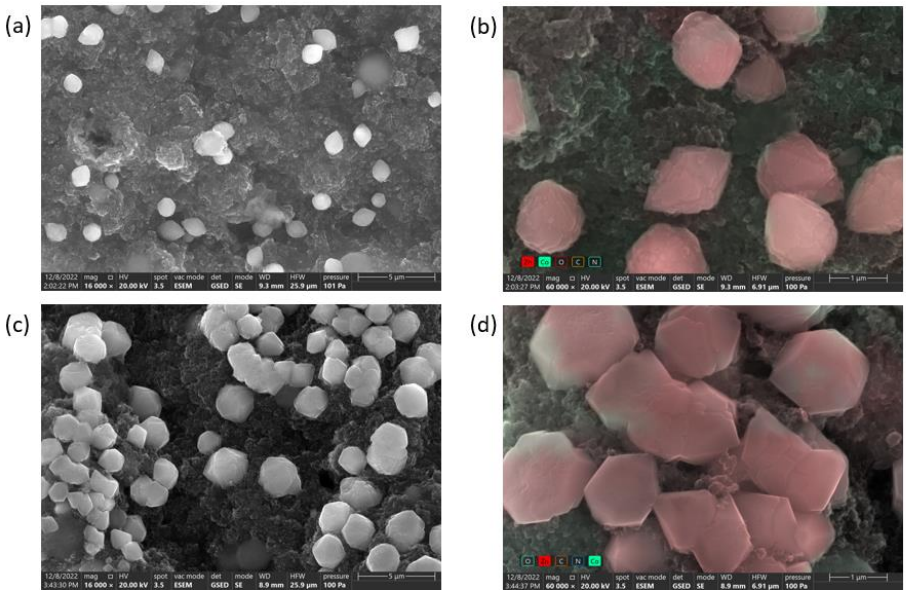


Figure 4.86. SEM images of SSM #10 (a) and (b) before, (c) and (d) after MFC tests.

Image of the Fe-MOF coated SSM, SSM #13 that is utilized in MFC study due to its conductivity and good ORR performance revealed with CV is shown in Figure 4.87.

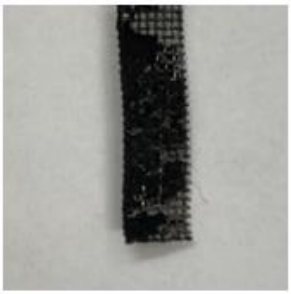


Figure 4.87. Image of the SSM #13, SSM coated with Fe-MOF, employed in MFC analysis.

MFC with SSM #13 (80% MIL-88A-1 / 10% CB / 10%) Cathode: After OCV analysis, LSV measurements are performed. Current density vs. potential plot (Figure 4.88) is obtained from LSV analysis and at around -1 V, biotic MFC showed higher current density compared to abiotic MFC with SSM #13 cathode due to E. Coli K-12 catalyzed current generation. OCV for biotic MFC (E.Coli K-12 inoculated MFC) was around 610 mV and 600 mV for abiotic MFC (MFC without bacteria).

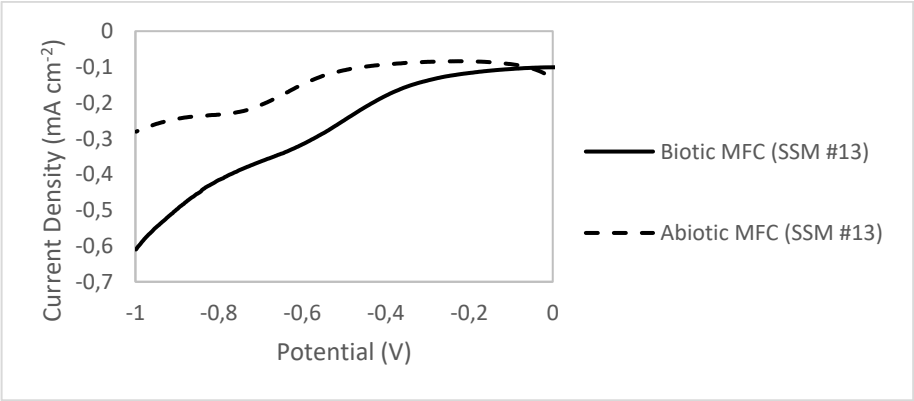


Figure 4.88. Current density vs. potential curve obtained from LSV of the MFC with SSM #13.

Nyquist plot obtained from EIS analysis revealing different resistance parameters is given in Figure 4.89. The inset shows the ohmic resistance of MFC with SSM #13 cathode as 39.7 ohms. The charge transfer resistance that is observed as the semicircle of the plot is approximately 550 ohms.

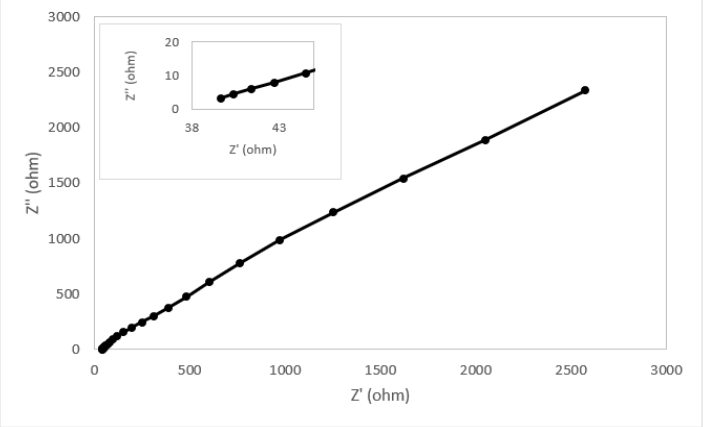


Figure 4.89. Nyquist plot of the MFC with SSM #13 cathode.

SEM images of SSM #13 cathode before and after being utilized in MFC are displayed in Figure 4.90 revealing the morphology of the coated SSM.

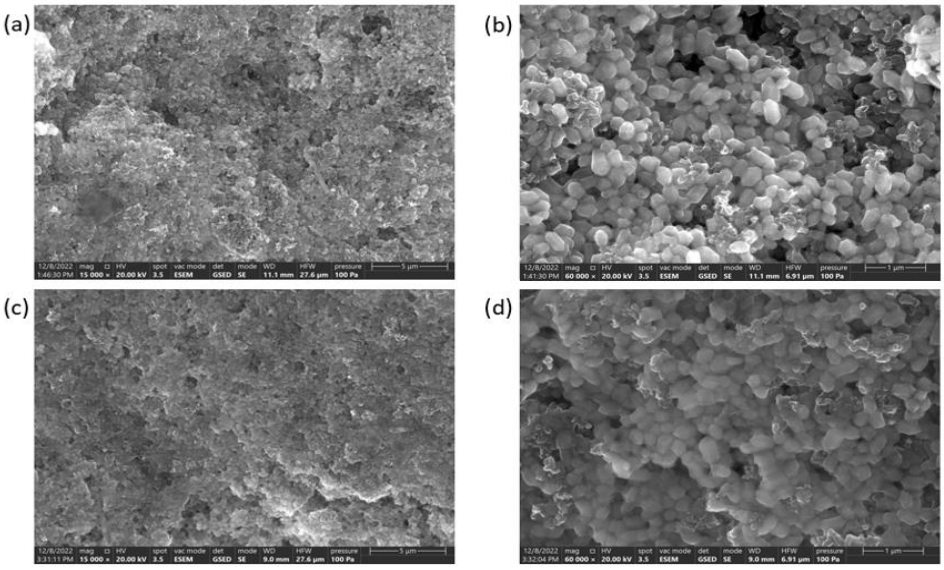


Figure 4.90. SEM images of SSM #9 (a) and (b) before, (c) and (d) after MFC tests.

Current density vs. potential plots of the MFC with various cathodes prepared through this study are obtained by LSV and displayed in Figure 4.91. SSM #7 (80% ZIF-L-1 / 10% CB / 10% PVA) showed highest current density than rest of the coated SSMs when employed in E.Coli K-12 inoculated MFC.

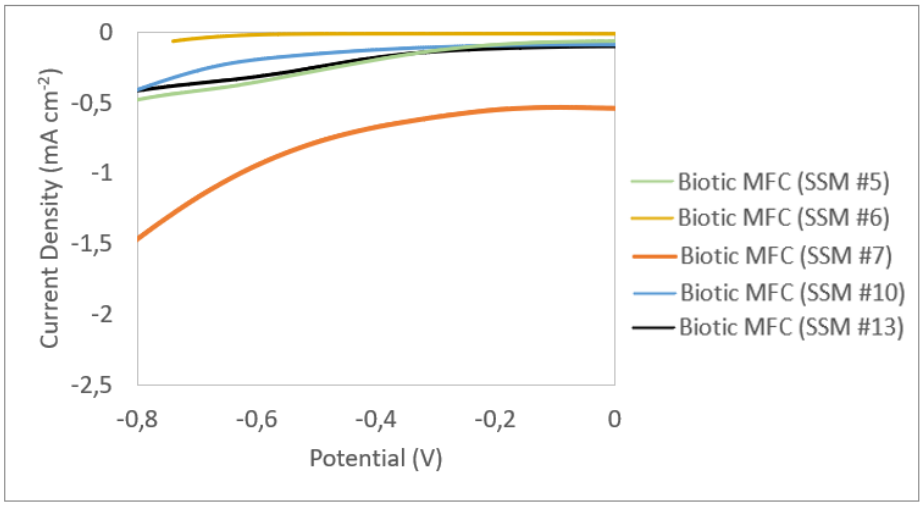


Figure 4.91. Current density vs. potential plot of MFCs with various cathodes.

Nyquist plots that are obtained from EIS are normalized with respect to cathode areas are displayed in Figure 4.92. MFC with SSM #7 (80% ZIF-L / 10% CB / 10% PVA) and SSM #13 (SSM coated with 80% MIL-88A-1 / 10% CB / 10%) displayed lowest ohmic resistances. On the other hand, since the semicircles represent the charge transfer resistance, it is demonstrated that MFC with SSM #7 (SSM coated with 80% ZIF-L / 10% CB / 10% PVA) cathode demonstrated the lowest charge transfer resistance as shown in the inset in Figure 4.92.

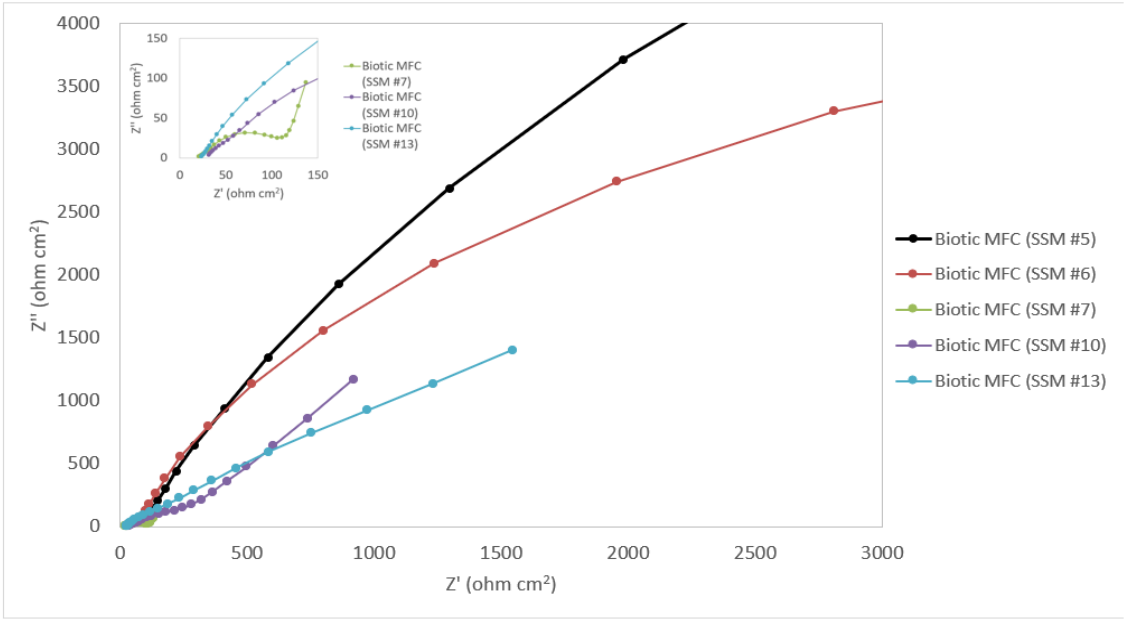


Figure 4.92. Nyquist plots of MFCs with various cathodes.

EIS results of the MFCs with the studied cathodes correlate with both LSV measurements and previous CV results of individual cathodes given below as current density vs. potential plot. SSM #7 showed better catalytic activity towards ORR with higher current responses than others. SSM #13 and SSM #10 also demonstrated higher reduction peak current densities (Figure 4.93).

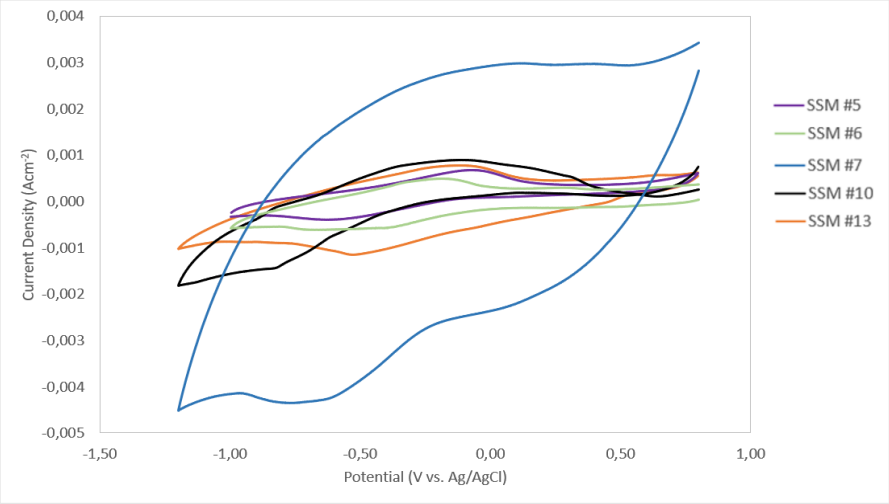


Figure 4.93. Current density vs. potential plots of the coated SSMs obtained from CV.

SEM images of the anode used, SSM #2, are displayed in Figure 4.93 before and after the MFC experimentation. After biotic MFC experiments, even though the anode is washed with distilled water there are remaining microorganisms, E.Coli K-12 cells, attached to the electrode showing the biofilm formation on the SSM #2 (Figure 4.94c and d).

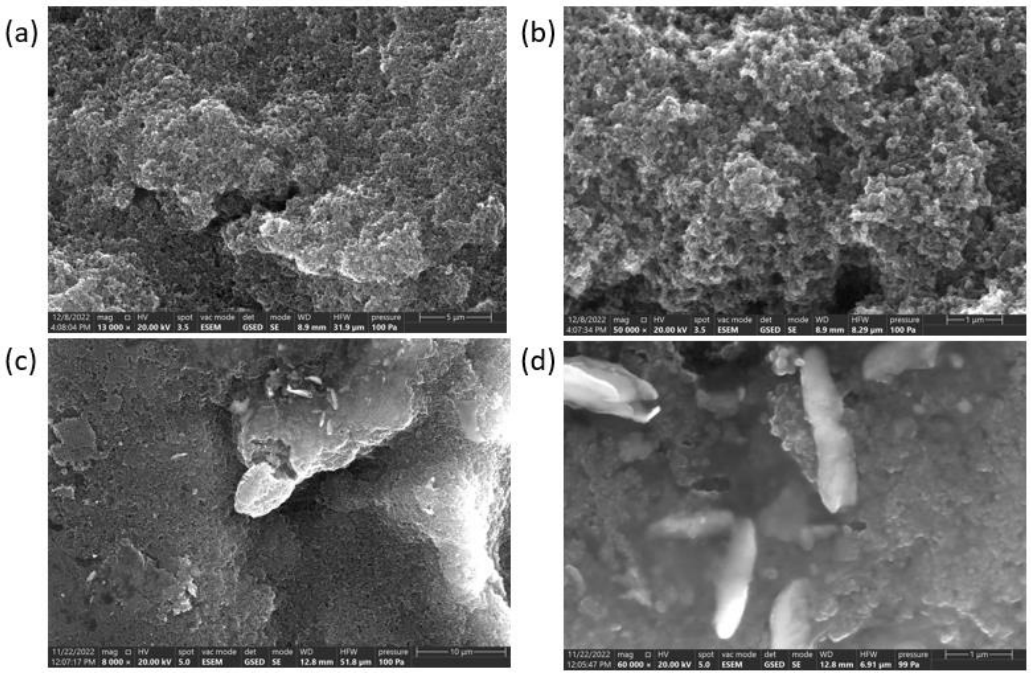


Figure 4.94. SEM images of the anode, SSM #2, (a) and (b) before, (c) and (d) after MFC tests.

5. CONCLUSION

Throughout this thesis study, synthesis of Zn, Co, and Fe metal organic frameworks (MOFs) with organic linkers as 2-methylimidazole, terephthalic acid and 2-aminoterephatlic via energy efficient room temperature and sonochemical synthesis methods is aimed in order to employ them as ORR catalysts for MFC cathodes. Synthesized frameworks are characterized by SEM and XRD analysis and effects of concentrations, molar ratios of reactants, solvent, metal ion precursor and second metal doping on the obtained compounds were also examined.

Obtained pristine MOFs' applicability as Microbial Fuel Cell (MFC) cathode catalysts are investigated by preparing slurries with carbon black and PVA (as binder polymer) and coating them on stainless-steel mesh (SSM) current collectors for the first time. Morphologies of the SSMs coated with MOF containing slurries are demonstrated by SEM. Conductivities of these coated SSMs are calculated from Chronopotentiometry analysis results and electrochemical characterization of the composites were done by CV for the first time for the prepared MOF-Carbon Black composite coated SSMs in this thesis study.

Current density vs. potential plots, obtained from CV after normalizing current with respect to area of the coated SSMs, revealed superior performance of SSM #7 (80% ZIF-L-1 / 10% CB / 10% PVA) among Zn-MOF composite coated SSMs, SSM #10 (60% Zn-doped ZIF-67-2 / 30% CB / 10% PVA) among Co-MOF composite coated SSMs and SSM #13 (80% MIL-88A-1 / 10% CB / 10% PVA) among Fe-MOF composite coated SSMs towards ORR. Overall, SSM coated with 80% ZIF-L-1 / 10% CB / 10% PVA containing slurry (SSM #7) demonstrated highest oxygen reduction peak current density through CV analysis.

Among the SSMs coated with MOF-Carbon Black composites, ones showing higher catalytic activity towards ORR further utilized in MFCs as cathode and their performances are analyzed through OCV, LSV and EIS for the first time in a two-chamber MFC utilizing

SSM #2 (SSM coated with 90% CB / 10% PVA containing slurry) as the novel anode electrode prepared through this thesis study as well. E. Coli K-12 was inoculated in the anodic chamber of the MFC, and glucose was employed as fuel, substrate. MFC analysis held in a fed-batch mode at RT.

.

MFCs with SSM #2 (90% CB / 10% PVA slurry) anode and SSM #5 (75% ZIF-8-3 / 15% CB / 10%PVA), SSM #6 (60% ZIF-L-1 / 30% CB / 10%PVA), SSM #7 (80% ZIF-L / 10% CB / 10% PVA), SSM #10 (60% Zn-doped ZIF-67-2 / 30% CB / 10% PVA) and SSM #13 (80% MIL-88A-1 / 10% CB / 10% PVA) cathodes demonstrated E. Coli catalyzed current generation which shows the composites of the pristine Zn, Co and Fe-MOFs applicability as MFC cathode catalysts.

MFC with the SSM #7 cathode containing coating of 80% ZIF-L / 10% CB / 10% PVA, demonstrated the lowest charge transfer resistance through EIS analysis and highest current density through LSV analalysis than others. However, obtained current densities are the range of -0.5 to -1.5 mA cm^{2-} which is most probably due to poor exoelectrogenic nature of E. Coli K-12.

In conclusion, ZIF-L, ZIF-8, Zn-doped ZIF-67 and MIL-88A MOFs that are synthesized through this thesis study with energy efficient room temperature and sonochemical synthesis methods, demonstrated to be applicable as MFC cathode catalysts for ORR by creating composites with carbon black and PVA, coating this composite slurries on SSM current collectors for the first time. All the characterizations and performance studies are completed on the SSMs coated with MOF composites are demonstrated for the first time whose results would be helpfull for future works.

6. FUTURE WORK

XRD patterns of synthesized MOFs for this study were analyzed by the XRD analysis database of the Advanced Technologies Research and Development Center. However, there were very few records for the XRD patterns of MOFs in general. So, exact matches through qualitative XRD analysis could not be obtained for the synthesized frameworks. In addition to that, most of the published research papers did not include the JCPDS or PDF file numbers for relevant MOFs. That is why the XRD patterns could be compared manually only with the published articles that give detail information about the diffraction peaks and planes. More information is required on the frameworks' XRD patterns, and a thorough XRD analysis of these compounds should be obtained.

Since the nature of the binders used through this study is electrically insulator, their content in the slurries kept minimum to prevent conductivity decrease. Instead of PVA, conductive polymeric binders may be studied for preparing the MOF composite slurries.

The performances of the novel electrodes prepared by coating SSMs should be analyzed by employing them in MFCs with extended operation times such as several months for their stabilities to be tested as well. Also, MFC operations should be conducted by commercially available standard anode materials like carbon cloth, carbon felt etc. for better reproducibility and comparability with the reported studies in the literature and between the cathode materials in interest with well-established, stable anode electrode.

Even though E.Coli catalyzed current production is observed through this study, the amount was very low which might be due to the poor exoelectorgenic nature of E. Coli K-12. That is why, further tests should be done by utilizing more exoelectorgenic bacteria.

After long-term MFC operations, stable and well performing cathodes should be selected and further used as bio-cathodes in MFCs since SSMs coated with MOFs might

present a hosting environment with their porous structure and formation of biofilm on these MOF coated SSMs may be enhanced due to presence of hydrophilic PVA binder for specific bacteria with hydrophilic extracellular structure. Also, due to different functionalities of the organic linkers present in these coatings makes the pristine MOFs promising candidate as biocathode materials since these structural functionalities may increase the interaction with the bacterial cell surface.

REFERENCES

1. Dharmalingam, S., V Kugarajah, and M. Sugumar, “Membranes for Microbial Fuel Cells”, *Microbial Electrochemical Technology*, Elsevier, pp. 143–194, 2019.

2. Slate, A. J., K. A. Whitehead., D. A. C. Brownson, and C. E. Banks, “Microbial Fuel Cells: An Overview of Current Technology”, *Renewable and Sustainable Energy Reviews*, Vol. 101, pp. 60–81, 2019.

3. Flimban, S. G. A., I. M. I. Ismail, T. Kim, and S.-E. Oh, “Overview of Recent Advancements in the Microbial Fuel Cell from Fundamentals to Applications: Design, Major Elements, and Scalability”, *Energies (Basel)*, Vol. 12, No. 17, p. 3390, 2019.

4. Do, M. H., H. H. Ngo, W. S. Guo, Y.Liu, S.W. Chang, D.D Nguyen, L.D. Nghiem, and B.J. Ni, “Challenges in the Application of Microbial Fuel Cells to Wastewater Treatment and Energy Production: A Mini Review”, *Science of The Total Environment*, Vol. 639, pp. 910–920, 2018.

5. Pant, D., G. van Bogaert, L. Diels, and K. Vanbroekhoven, “A Review of the Substrates Used in Microbial Fuel Cells (MFCs) for Sustainable Energy Production”, *Bioresource Technology*, Vol. 101, No. 6, pp. 1533–1543, 2010.

6. Rinaldi, A., B. Mecheri, V. Garavaglia, S. Licoccia, P. di Nardo, and E. Traversa, “Engineering Materials and Biology to Boost Performance of Microbial Fuel Cells: A Critical Review”, *Energy & Environmental Science*, Vol. 1, No. 4, p. 417, 2008.

7. Liu, H. and B. E. Logan, “Electricity Generation Using an Air-Cathode Single Chamber Microbial Fuel Cell in the Presence and Absence of a Proton Exchange Membrane”, *Environmental Science & Technology*, Vol. 38, No. 14, pp. 4040–4046, 2004.

8. Kim, J. R., S. Cheng, S.-E. Oh, and B. E. Logan, “Power Generation Using Different Cation, Anion, and Ultrafiltration Membranes in Microbial Fuel Cells”, *Environmental Science & Technology*, Vol. 41, No. 3, pp. 1004–1009, 2007.

9. Oh, S., B. Min, and B. E. Logan, “Cathode Performance as a Factor in Electricity Generation in Microbial Fuel Cells”, *Environmental Science & Technology*, Vol. 38, No. 18, pp. 4900–4904, 2004.

10. You, S., Q. Zhao, J. Zhang, J. Jiang, and S. Zhao, “A Microbial Fuel Cell Using Permanganate as the Cathodic Electron Acceptor”, *Journal of Power Sources*, Vol. 162, No. 2, pp. 1409–1415, 2006.

11. Huang, L. and B. E. Logan, “Electricity Production from Xylose in Fed-batch and Continuous-flow Microbial Fuel Cells”, *Applied Microbiology and Biotechnology*, Vol. 80, No. 4, p. 655, 2008.

12. Pannell, T. C., R. K. Goud, D. J. Schell, and A. P. Borole, “Effect of Fed-batch vs. Continuous Mode of Operation on Microbial Fuel Cell Performance Treating Biorefinery Wastewater”, *Biochemical Engineering Journal*, Vol. 116, pp. 85–94, 2016.

13. Chen, G., B. Wei, Y. Luo, B. E. Logan, and M. A. Hickner, “Polymer Separators for High-Power, High-Efficiency Microbial Fuel Cells”, *ACS Applied Materials & Interfaces*, Vol. 4, No. 12, pp. 6454–6457, 2012.

14. Sedesheva, Y., V. Ivanov, A. Wozniak, and A. Yegorov, “Proton-Exchange Membranes Based on Sulfonated Polymers”, *Oriental Journal of Chemistry*, Vol. 32, No. 5, pp. 2283–2296, 2016.

15. Lovely, D. R., “Bug Juice: Harvesting Electricity with Microorganisms”, *Nature Reviews Microbiology*, Vol. 4, No. 7, pp. 497–508, 2006.

16. Fan, L. and S. Xue, “Overview on Electricigens for Microbial Fuel Cell”, *The Open Biotechnology Journal*, Vol. 10, No. 1, pp. 398–406, 2016.

17. Reiche, A. and K. M. Kirkwood, “Comparison of Escherichia Coli and Anaerobic Consortia Derived from Compost as Anodic Biocatalysts in a Glycerol-oxidizing Microbial Fuel Cell”, *Bioresource Technology*, Vol. 123, pp. 318–323, 2012.

18. Nandy, A., S. Jana, M. Khamrai, V. Kumar, S. Mukherjee, A. Bhattacharyya, and P. P. Kundu, “Cloning and Expression of α-amylase in *E. coli* : Genesis of a Superior Biocatalyst for Substrate-specific MFC”, *International Journal of Green Energy*, Vol. 16, No. 4, pp. 309–316, 2019.

19. Yong, Y.-C., Y.-Y. Yu, Y. Yang, C. M. Li, R. Jiang, X. Wang, J.-Y. Wang, and H. Song, “Increasing Intracellular Releasable Electrons Dramatically Enhances Bioelectricity Output in Microbial Fuel Cells”, *Electrochemistry Communications*, Vol. 19, pp. 13–16, 2012.

20. Gao, X., Y. Zhang, X. Li, and J. Ye, “Novel Graphite Sheet Used as an Anodic Material for High-Performance Microbial Fuel Cells”, *Materials Letters*, Vol. 105, pp. 24–27, 2013.

21. Rabaey, K., G. Lissens, S. D. SiciliaNo, and W. Verstraete, “A Microbial Fuel Cell Capable of Converting Glucose to Electricity at High Rate and Efficiency”, *Biotechnology Letters*, Vol. 25, No. 18, pp. 1531–1535, 2003.

22. Ringeisen, B. R., E. Henderson, P. K. Wu, J. Pietron, R. Ray, B. Little, J.C Biffinger, and J. M. Jones-Meehan, “High Power Density from a Miniature Microbial Fuel Cell Using *Shewanella Oneidensis* DSP10”, *Environmental Science & Technology*, Vol. 40, No. 8, pp. 2629–2634, 2006.

23. Liu, H., R. Ramnarayanan, and B. E. Logan, “Production of Electricity During Wastewater Treatment Using a Single Chamber Microbial Fuel Cell”, *Environmental Science & Technology*, Vol. 38, No. 7, pp. 2281–2285, 2004.

24. Kim, H. J., H. S. Park, M. S. Hyun, I. S. Chang, M. Kim, and B. H. Kim, “A Mediator-less Microbial Fuel Cell Using a Metal Reducing Bacterium, Shewanella Putrefaciens”, *Enzyme and Microbial Technology*, Vol. 30, No. 2, pp. 145–152, 2002.

25. Liu, L. and S. Choi, “Self-sustaining, Solar-driven Bioelectricity Generation in Micro-sized Microbial Fuel Cell Using Co-culture of Heterotrophic and Photosynthetic Bacteria”, *Journal of Power Sources*, Vol. 348, pp. 138–144, 2017.

26. Wang, X., S. Cheng, Y. Feng, M. D. Merrill, T. Saito, and B. E. Logan, “Use of Carbon Mesh Anodes and the Effect of Different Pretreatment Methods on Power Production in Microbial Fuel Cells”, *Environmental Science & Technology*, Vol. 43, No. 17, pp. 6870–6874, 2009.

27. Thepsuparungsikul, N., T. C. Ng, O. Lefebvre, and H. Y. Ng, “Different Types of Carbon Nanotube-based Anodes to Improve Microbial Fuel Cell Performance”, *Water Science and Technology,* Vol. 69, No. 9, pp. 1900–1910, 2014.

28. Fu, Y., Z. Lu, X. Zai, and J. Wang, “Carbon Foam Anode Modified by Urea and Its Higher Electrochemical Performance in Marine Benthic Microbial Fuel Cell”, *Journal of Ocean University of China,* Vol. 14, No. 4, pp. 663–668, 2015.

29. Ren, H., H. Tian, C. L. Gardner, T.-L. Ren, and J. Chae, “A Miniaturized Microbial Fuel Cell with Three-dimensional Graphene Macroporous Scaffold Anode Demonstrating a Record Power Density of Over 10 000 W m $^{-3}$”, *Nanoscale*, Vol. 8, No. 6, pp. 3539–3547, 2016.

30. Zhou, M., M. Chi, J. Luo, H. He, and T. Jin, “An Overview of Electrode Materials in Microbial Fuel Cells”, *Journal of Power Sources*, Vol. 196, No. 10, pp. 4427–4435, 2011.

31. Xie, X., C. Criddle, and Y. Cui, “Design and Fabrication of Bioelectrodes for Microbial Bioelectrochemical Systems”, *Energy and Environmental Science*, Vol. 8, No. 12, pp. 3418–3441, 2015

32. Gnana kumar, G., C. J. Kirubaharan, S. Udhayakumar, K. Ramachandran, C. Karthikeyan, R. Renganathan, and K. S. Nahm, "Synthesis, Structural, and Morphological Characterizations of Reduced Graphene Oxide-Supported Polypyrrole Anode Catalysts for Improved Microbial Fuel Cell Performances", *ACS Sustainable Chemistry & Engineering*, Vol. 2, No. 10, pp. 2283–2290, 2014.

33. Hou, J., Z. Liu, and P. Zhang, "A New Method for Fabrication of Graphene/Polyaniline Nanocomplex Modified Microbial Fuel Cell Anodes", *Journal of Power Sources*, Vol. 224, pp. 139–144, 2013.

34. Liu, X. and Z. Gu, "Application of Entangled Multi-Wall Carbon Nanotubes Doped Poly(3,4-ethylenedioxythiophene) Network on the Anode to Increase the Power Generation in a Microbial Fuel Cell", *Journal of Nanoscience and Nanotechnology*, Vol. 16, No. 12, pp. 12369–12373, 2016.

35. Guo, K., S. Freguia, P. G. Dennis, X. Chen, B. C. Donose, J. J. Gooding, and K.Rabaey, "Effects of Surface Charge and Hydrophobicity on Anodic Biofilm Formation, Community Composition, and Current Generation in Bioelectrochemical Systems", *Environmental Science & Technology*, Vol. 47, No. 13, pp. 7563–7570, 2013.

36. Chen, X. F., X. S. Wang, K. T. Liao, L. Z. Zeng, L. D. Xing, X. W. Zhou, X. W. Zhenga, and W. S. Li, "Improved Power Output by Incorporating Polyvinyl Alcohol into the Anode of a Microbial Fuel Cell", *Journal of Materials Chemistry A*, Vol. 3, No. 38, pp. 19402–19409, 2015.

37. Tahir, K., W. Miran, J. Jang, N. Maile, A. Shahzad, M. Moztahida, A. A. Ghani, B. Kim, and D. S. Lee "$MnCo_2O_4$ Coated Carbon Felt Anode for Enhanced Microbial Fuel Cell Performance", *Chemosphere*, Vol. 265, p. 129098, 2021.

38. Baudler, A., I. Schmidt, M. Langner, A. Greiner, and U. Schröder, "Does It Have To Be Carbon? Metal Anodes in Microbial Fuel Cells and Related Bioelectrochemical Systems", *Energy and Environmental Science*, Vol. 8, No. 7, pp. 2048–2055, 2015.

39. Kalathil, S., S. A. Patil, and D. Pant, “Microbial Fuel Cells: Electrode Materials”, *Encyclopedia of Interfacial Chemistry*, Elsevier, pp. 309–318, 2018.

40. Pocaznoi, D., A. Calmet, L. Etcheverry, B. Erable, and A. Bergel, “Stainless Steel Is A Promising Electrode Material for Anodes of Microbial Fuel Cells”, *Energy and Environmental Science*, Vol. 5, No. 11, p. 9645, 2012.

41. Liang, Y., H. Feng, D. Shen, Na Li, K. Guo, Y. Zho, J. Xu, W. Chen, Y. Jia, and B. Huan, “Enhancement of Anodic Biofilm Formation and Current Output in Microbial Fuel Cells by Composite Modification of Stainless Steel Electrodes”, *Journal of Power Sources*, Vol. 342, pp. 98–104, 2017.

42. Zheng, S., F. Yanga, S. Chen, L. Liu, Q. Xionga, T. Yu, F. Zhao, U. Schröder, and H. Hou, “Binder-free Carbon Black/Stainless Steel Mesh Composite Electrode for High-Performance Anode in Microbial Fuel Cells”, *Journal of Power Sources*, Vol. 284, pp. 252–257, 2015,

43. Song, C. and J. Zhang, “Electrocatalytic Oxygen Reduction Reaction”, *PEM Fuel Cell Electrocatalysts and Catalyst Layers*, Springer London, pp. 89–134, 2008.

44. Costa de Oliveira, M. A., A. D’Epifanio, H. Ohnuki, and B. Mecheri, “Platinum Group Metal-Free Catalysts for Oxygen Reduction Reaction: Applications in Microbial Fuel Cells”, *Catalysts*, Vol. 10, No. 5, p. 475, 2020.

45. Hansen, H. A., V. Viswanathan, and J. K. Nørskov, “Unifying Kinetic and Thermodynamic Analysis of 2 e^- and 4 e^- Reduction of Oxygen on Metal Surfaces”, *The Journal of Physical Chemistry C*, Vol. 118, No. 13, pp. 6706–6718, 2014.

46. Holton, O. T. and J. W. Stevenson, “The Role of Platinum in Proton Exchange Membrane Fuel Cells”, P*latinum Metals Review*, Vol. 57, No. 4, pp. 259–271, 2013.

47. Stacy, J., Y. N. Regmi, B. Leonard, and M. Fan, “The Recent Progress and Future of Oxygen Reduction Reaction Catalysis: A Review”, *Renewable and Sustainable Energy Reviews*, Vol. 69, pp. 401–414, 2017.

48. Priyadarshini, M., A. Ahmad, S. Das, and M. M. Ghangrekar, “Metal Organic Frameworks as Emergent Oxygen-Reducing Cathode Catalysts for Microbial Fuel Cells: A Review”, *International Journal of Environmental Science and Technology*, Vol. 19, No. 11, pp. 11539–11560, 2022.

49. Yang, W., J. Li, Q. Fu, L. Zhang, Z. Wei, Q. Liao, and X. Zhu, “Minimizing Mass Transfer Losses in Microbial Fuel Cells: Theories, Progresses and Prospectives” *Renewable and Sustainable Energy Reviews*, Vol. 136, p. 110460, 2021.

50. Logan, B. E., B. Hamelers, R. Rozendal, U. Schröder, J. Keller, S. Freguia, P. Aelterman, W. Verstraete, and K. Rabaey, “Microbial Fuel Cells: Methodology and Technology”, *Environmental Science & Technology*, Vol. 40, No. 17, pp. 5181–5192, 2006.

51. Cheng, S., H. Liu, and B. E. Logan, “Power Densities Using Different Cathode Catalysts (Pt and CoTMPP) and Polymer Binders (Nafion and PTFE) in Single Chamber Microbial Fuel Cells”, *Environmental Science & Technology*, Vol. 40, No. 1, pp. 364–369, 2006.

52. Khilari, S. and D. Pradhan, “Role of Cathode Catalyst in Microbial Fuel Cell”, *Microbial Fuel Cell: A Bioelectrochemical System that Converts Waste to Watts*, Springer Cham, pp. 141–163, 2018.

53. Zhang, F., T. Saito, S. Cheng, M. A. Hickner, and B. E. Logan, “Microbial Fuel Cell Cathodes with Poly(dimethylsiloxane) Diffusion Layers Constructed around Stainless Steel Mesh Current Collectors”, *Environmental Science & Technology*, Vol. 44, No. 4, pp. 1490–1495, 2010.

54. Wu, S., H. Li, X. Zhou, P. Liang, X. Zhang, Y. Jiang, and X. Huang, "A Novel Pilot-Scale Stacked Microbial Fuel Cell for Efficient Electricity Generation and Wastewater Treatment", *Water Research*, Vol. 98, pp. 396–403, 2016.

55. Rabaey, K., N. Boon, S. D. Siciliano, M. Verhaege, and W. Verstraete, "Biofuel Cells Select for Microbial Consortia That Self-Mediate Electron Transfer", *Applied Environmental Microbiology*, Vol. 70, No. 9, pp. 5373–5382, 2004.

56. Yang, W., W. He, F. Zhang, M. A. Hickner, and B. E. Logan, "Single-Step Fabrication Using a Phase Inversion Method of Poly(vinylidene fluoride) (PVDF) Activated Carbon Air Cathodes for Microbial Fuel Cells", *Environmental Science & Technology Lett*, Vol. 1, No. 10, pp. 416–420, 2014.

57. Hung, Y.-H., T.-Y. Liu, and H.-Y. Chen, "Renewable Coffee Waste-Derived Porous Carbons as Anode Materials for High-Performance Sustainable Microbial Fuel Cells", *ACS Sustainable Chemistry & Engineering*, Vol. 7, No. 20, pp. 16991–16999, 2019.

58. Yuan, Y., S. Zhou, and L. Zhuang, "Polypyrrole/Carbon Black Composite as a Novel Oxygen Reduction Catalyst for Microbial Fuel Cells", *Journal of Power Sources*, Vol. 195, No. 11, pp. 3490–3493, 2010.

59. Narayanasamy, S. and J. Jayaprakash, "Application of Carbon-Polymer Based Composite Electrodes for Microbial Fuel Cells", *Reviews in Environmental Science and Bio/Technology*, Vol. 19, No. 3, pp. 595–620, 2020.

60. Xue, W., Q. Zhou, F. Li, and B. S. Ondon, "Zeolitic Imidazolate Framework-8 (ZIF-8) as Robust Catalyst for Oxygen Reduction Reaction in Microbial Fuel Cells", *Journal of Power Sources*, Vol. 423, pp. 9–17, 2019.

61. Das, I., Md. T. Noori, M. Shaikh, M. M. Ghangrekar, and R. Ananthakrishnan, "Synthesis and Application of Zirconium Metal–Organic Framework in Microbial Fuel Cells as a Cost-Effective Oxygen Reduction Catalyst with Competitive Performance", *ACS Applied Energy Materials*, Vol. 3, No. 4, pp. 3512–3520, 2020.

62. Song, H.-L., Y. Zhu, and J. Li, "Electron Transfer Mechanisms, Characteristics and Applications of Biological Cathode Microbial Fuel Cells – A Mini Review", *Arabian Journal of Chemistry*, Vol. 12, No. 8, pp. 2236–2243, 2019.

63. Freguia, S., K. Rabaey, Z. Yuan, and J. Keller, "Sequential Anode–Cathode Configuration Improves Cathodic Oxygen Reduction and Effluent Quality of Microbial Fuel Cells", *Water Research*, Vol. 42, No. 6–7, pp. 1387–1396, 2008.

64. Vervoorts, P. *et al.*, "Coordinated Water as New Binding Sites for the Separation of Light Hydrocarbons in Metal–Organic Frameworks with Open Metal Sites", *ACS Applied Materials & Interfaces*, Vol. 12, No. 8, pp. 9448–9456, 2020.

65. Safaei, M., M. M. Foroughi, N. Ebrahimpoor, S. Jahani, A. Omidi, and M. Khatami, "A Review on Metal-Organic Frameworks: Synthesis and Applications", *TrAC Trends in Analytical Chemistry*, Vol. 118, pp. 401–425, 2019.

66. Sharanyakanth, P. S. and M. Radhakrishnan, "Synthesis of Metal-Organic Frameworks (MOFs) and Its Application in Food Packaging: A Critical Review", *Trends in Food Science & Technology*, Vol. 104, pp. 102–116, 2020.

67. Champness, N. R., Chen, X. M., Garcia-Martinez, J., Kitagawa, S., Öhrström, L., O'Keeffe, M., Suh, M. P., and Reedijk, J. (2012), "Coordination Polymers, Metal-Organic Frameworks and the Need for Terminology Guidelines", *Crystal Engineering Community*, Vol. 14, No. 9, pp. 3001–3004, 2012.

68. Hönicke, I. M., I. Senkovska, V. Bon, I. A Baburin, N. Bönisch, S. Raschke, J. D Evans, and S. Kaskel, "Balancing Mechanical Stability and Ultrahigh Porosity in Crystalline Framework Materials", *Angewandte Chemie International Edition*, Vol. 57, No. 42, pp. 13780–13783, 2018.

69. Lau, C. H., R. Babarao, and M. R. Hill, "A Route to Drastic Increase of CO_2 Uptake in Zr Metal Organic Framework UiO-66", *Chemical Communications*, Vol. 49, No. 35, p. 3634, 2013.

70. Xue, D.-X., Y. Belmabkhout, O. Shekhah, H. Jiang, K. Adil, A. J Cairns, and M. Eddaoudi, “Tunable Rare Earth fcu-MOF Platform: Access to Adsorption Kinetics Driven Gas/Vapor Separations via Pore Size Contraction”, *Journal of the American Chemical Society*, Vol. 137, No. 15, pp. 5034–5040, 2015.

71. Jin, Z. and H. Yang, “Exploration of Zr–Metal–Organic Framework as Efficient Photocatalyst for Hydrogen Production”, *Nanoscale Research Letters*, Vol. 12, No. 1, p. 539, 2017.

72. Llabrés i Xamena, F. X., A. Abad, A. Corma, and H. Garcia, “MOFs as Catalysts: Activity, Reusability and Shape-Selectivity of a Pd-Containing MOF”, *Journal of Catalysis*, Vol. 250, No. 2, pp. 294–298, 2007.

73. Gordon, J., H. Kazemian, and S. Rohani, “MIL-53(Fe), MIL-101, and SBA-15 Porous Materials: Potential Platforms for Drug Delivery”, *Materials Science and Engineering: C*, Vol. 47, pp. 172–179, 2015.

74. Guo, Y., X. Feng, T. Han, S. Wang, Z. Ling, Y. Dong, and B. Wang, “Tuning the Luminescence of Metal–Organic Frameworks for Detection of Energetic Heterocyclic Compounds”, *J Am Chem Soc*, Vol. 136, No. 44, pp. 15485–15488, 2014.

75. Chen, B., Y. Yang, F. Zapata, G. Lin, G. Qian, and E. B. Lobkovsky, “Luminescent Open Metal Sites within a Metal–Organic Framework for Sensing Small Molecules”, *Advanced Materials*, Vol. 19, No. 13, pp. 1693–1696, 2007.

76. Chen, X., J.-X. Zhao, J.-W. Wang, Y. Liu, L.-C. Wang, R. Weerasooriya, and Y.-C. Wu, “Doping ZIF-67 with Transition Metals Results in Bimetallic Centers for Electrochemical Detection of Hg(II)”, *Electrochimica Acta*, Vol. 387, p. 138539, 2021.

77. Gu, S., Z. Bai, S. Majumder, B. Huang, and G. Chen, “Conductive Metal–Organic Framework with Redox Metal Center as Cathode for High Rate Performance Lithium Ion Battery”, *Journal of Power Sources*, Vol. 429, pp. 22–29, 2019.

78. Cao, W., M. Han, L. Qin, Q. Jiang, J. Xu, Z. Lu, and Y. Wang, “Synthesis of Zeolitic Imidazolate Framework-67 Nanocube Wrapped by Graphene Oxide and Its Application for Supercapacitors”, *Journal of Solid State Electrochemistry*, Vol. 23, No. 1, pp. 325–334, 2019.

79. Chen, Z., Q. Wu, and H. Zhang, “Novel Co/UiO-66 Metal Organic Framework Catalyst for Oxygen Reduction Reaction in Microbial Fuel Cells”, *E3S Web of Conferences*, Vol. 245, p. 03017, 2021.

80. Raza, N., T. Kumar, V. Singh, and K.-H. Kim, “Recent Advances in Bimetallic Metal-Organic Framework as a Potential Candidate for Supercapacitor Electrode Material”, *Coordination Chemistry Reviews*, Vol. 430, p. 213660, 2021.

81. Zhou, K., B. Mousavi, Z. Luo, S. Phatanasri, S. Chaemchuen, and F. Verpoort, “Characterization and Properties of Zn/Co Zeolitic Imidazolate Frameworks vs. ZIF-8 and ZIF-67”, *Journal of Materials Chemistry A*, Vol. 5, No. 3, pp. 952–957, 2017.

82. Chen, L., H.-F. Wang, C. Li, and Q. Xu, “Bimetallic Metal–Oganic Frameworks and Their Derivatives”, *Chem Sci*, Vol. 11, No. 21, pp. 5369–5403, 2020.

83. Ahmed, S. A., D. Bagchi, H. A. Katouah, Md. N. Hasan, H. M. Altass, and S. K. Pal, “Enhanced Water Stability and Photoresponsivity in Metal-Organic Framework (MOF): A Potential Tool to Combat Drug-resistant Bacteria”, *Sci Rep*, Vol. 9, No. 1, p. 19372, 2019.

84. Zou, L., D. Feng, T.-F. Liu, Y.-P. Chen, S. Yuan, K. Wang, X. Wang, S. Fordham, and H.-C. Zhou, “A Versatile Synthetic Route for the Preparation of Titanium Metal–Organic Frameworks”, *Chemical Science*, Vol. 7, No. 2, pp. 1063–1069, 2016.

85. Fu, Y., L. Xu, H. Shen, H. Yang, F. Zhang, W. Zhu, and M. Fan, “Tunable Catalytic Properties of Multi-Metal–Organic Frameworks for Aerobic Styrene Oxidation”, *Chemical Engineering Journal*, Vol. 299, pp. 135–141, 2016.

86. Hu, Y. *et al.*, “One-Pot Synthesis of Bimetallic Metal–Organic Frameworks (MOFs) as Acid–Base Bifunctional Catalysts for Tandem Reaction”, *Catalysis Science & Technology*, Vol. 10, No. 2, pp. 315–322, 2020.

87. Sun, S., P. Wang, and M. Lu, “Modification with Ultrasonication for Enhanced Properties of Cobalt-Based Zeolitic Imidazolate Framework”, *MRS Communications*, Vol. 8, No. 3, pp. 1363–1370, 2018.

88. Yin, P. *et al.*, “Single Cobalt Atoms with Precise N-Coordination as Superior Oxygen Reduction Reaction Catalysts”, *Angewandte Chemie*, Vol. 128, No. 36, pp. 10958–10963, 2016.

89. Sanad, M. F. *et al.*, “Co–Cu Bimetallic Metal Organic Framework Catalyst Outperforms the Pt/C Benchmark for Oxygen Reduction”, *Journal of the American Chemical Society*, Vol. 143, No. 10, pp. 4064–4073, 2021.

90. Yoon, H., S. Lee, S. Oh, H. Park, S. Choi, and M. Oh, “Synthesis of Bimetallic Conductive 2D Metal–Organic Framework (Co_xNi_y-CAT) and Its Mass Production: Enhanced Electrochemical Oxygen Reduction Activity”, *Small*, Vol. 15, No. 17, p. 1805232, 2019.

91. Saiyed, T. A., J. O. Adeyemi, and D. C. Onwudiwe, “The Structural Chemistry of Zinc(II) and Nickel(II) dithiocarbamate Complexes”, *Open Chemistry*, Vol. 19, No. 1, pp. 974–986, 2021.

92. Rocío-Bautista, P., I. Taima-Mancera, J. Pasán, and V. Pino, “Metal-Organic Frameworks in Green Analytical Chemistry”, *Separations*, Vol. 6, No. 3, p. 33, 2019.

93. Cook, T. R., Y.-R. Zheng, and P. J. Stang, "Metal–Organic Frameworks and Self-Assembled Supramolecular Coordination Complexes: Comparing and Contrasting the Design, Synthesis, and Functionality of Metal–Organic Materials", *Chemical Reviews*, Vol. 113, No. 1, pp. 734–777, 2013.

94. Dai, S., A. Tissot, and C. Serre, "Metal-Organic Frameworks: From Ambient Green Synthesis to Applications", *Bulletin of the Chemical Society of Japan*, Vol. 94, No. 11, pp. 2623–2636, 2021.

95. Dai, J., X. Xiao, S. Duan, J. Liu, J. He, J. Lei, and L. Wang, "Synthesis of Novel Microporous Nanocomposites of ZIF-8 on Multiwalled Carbon Nanotubes for Adsorptive Removing Benzoic Acid from Water", *Chemical Engineering Journal*, Vol. 331, pp. 64–74, 2018.

96. Dai, S., F. Nouar, S. Zhang, A. Tissot, and C. Serre, "One-Step Room-Temperature Synthesis of Metal(IV) Carboxylate Metal-Organic Frameworks", *Angewandte Chemie International Edition*, Vol. 60, No. 8, pp. 4282–4288, 2021.

97. Han, Y., H. Yang, and X. Guo, "Synthesis Methods and Crystallization of MOFs", *Synthesis Methods and Crystallization*, IntechOpen, 2020.

98. Dey, C., T. Kundu, B. P. Biswal, A. Mallick, and R. Banerjee, "Crystalline Metal-Organic Frameworks (MOFs): Synthesis, Structure and Function", *Acta Crystallographica Section B: Structural Science, Crystal Engineering and Materials*, Vol. 70, No. 1, pp. 3–10, 2014.

99. Klinowsk, J., F. A. Almeida Paz, P. Silva, and J. Rocha, "Microwave-Assisted Synthesis of Metal–Organic Frameworks", *Dalton Transactions.*, Vol. 40, No. 2, pp. 321–330, 2011.

100. Wei, J.-Z., F.-X. Gong, X.-J. Sun, Y. Li, T. Zhang, X.-J. Zhao, and F.-M. Zhang, "Rapid and Low-Cost Electrochemical Synthesis of UiO-66-NH_2 with Enhanced Fluorescence Detection Performance", *Inorganic Chemistry*, Vol. 58, No. 10, pp. 6742–6747, 2019.

101. Chen, D., J. Zhao, P. Zhang, and S. Dai, "Mechanochemical Synthesis of Metal–Organic Frameworks", *Polyhedron*, Vol. 162, pp. 59–64, 2019.

102. Vaitsis, C., G. Sourkouni, and C. Argirusis, "Metal Organic Frameworks (MOFs) and Ultrasound: A Review", *Ultrasonics Sonochemistry*, Vol. 52, pp. 106–119, 2019.

103. Vaitsis, C., G. Sourkouni, and C. Argirusis, "Sonochemical Synthesis of MOFs", in *Metal-Organic Frameworks for Biomedical Applications*, Woodhead Publishing, Elsevier, pp. 223–244, 2020.

104. Stock, N. and S. Biswas, "Synthesis of Metal-Organic Frameworks (MOFs): Routes to Various MOF Topologies, Morphologies, and Composites", *Chemical Reviews*, Vol. 112, No. 2, pp. 933–969, 2012.

105. Bian, Y., N. Xiong, and G. Zhu, "Technology for the Remediation of Water Pollution: A Review on the Fabrication of Metal Organic Frameworks", *Processes*, Vol. 6, No. 8, p. 122, 2018.

106. Xiao, J.-D., L.-G. Qiu, F. Ke, Y.-P. Yuan, G.-S. Xu, Y.-M. Wang, and X. Jiang "Rapid Synthesis of Nanoscale Terbium-Based Metal–Organic Frameworks by a Combined Ultrasound-Vapour Phase Diffusion Method for Highly Selective Sensing of Picric Acid", *Journal of Materials Chemistry A*, Vol. 1, No. 31, p. 8745, 2013.

107. Rogers, R. D. and K. R. Seddon, "Ionic Liquids-Solvents of the Future?", *Science (1979)*, Vol. 302, No. 5646, pp. 792–793, 2003.

108. H.-C. Oh, S. Jung, I.-J. Ko, and E.-Y. Choi, “Ionothermal Synthesis of Metal-Organic Framework”, *Recent Advancements in the Metallurgical Engineering and Electrodeposition*, IntechOpen, 2020.

109. Seetharaj, R., P. V. Vandana, P. Arya, and S. Mathew, “Dependence of Solvents, pH, Molar Ratio and Temperature in Tuning Metal Organic Framework Architecture”, *Arabian Journal of Chemistry*, Vol. 12, No. 3, pp. 295–315, 2019.

110. Long, P., H. Wu, Q. Zhao, Y. Wang, J. Dong, and J. Li, “Solvent Effect on the Synthesis of MIL-96(Cr) and MIL-100(Cr)”, *Microporous and Mesoporous Materials*, Vol. 142, No. 2–3, pp. 489–493, 2011.

111. Huelsenbeck, L., H. Luo, P. Verma, J. Dane, R. Ho, E. Beyer, H. Hall, G. M. Geise, and G. Giri, “Generalized Approach for Rapid Aqueous MOF Synthesis by Controlling Solution pH”, *Crystal Growth & Design*, Vol. 20, No. 10, pp. 6787–6795, 2020.

112. Figueroa-Quintero, L., E. V. Ramos-Fernandez, and J. Narciso, “Synthesis and Characterization of the Metal–Organic Framework CIM-80 for Organic Compounds Adsorption”, *Materials*, Vol. 15, No. 15, p. 5326, 2022.

113. Rodríguez, N. A., R. Parra, and M. A. Grela, “Triethylamine as a Tuning Agent of the MIL-125 Particle Morphology and Its Effect on the Photocatalytic Activity”, *SN Applied Sciences*, Vol. 2, No. 11, p. 1881, 2020.

114. Guo, H., Y. Zhu, S. Wang, S. Su, L. Zhou, and H. Zhang, “Combining Coordination Modulation with Acid–Base Adjustment for the Control over Size of Metal–Organic Frameworks”, *Chemistry of Materials*, Vol. 24, No. 3, pp. 444–450, 2012.

115. Forgan, R. S., “Modulated Self-Assembly of Metal–Organic Frameworks”, *Chemical Science*, Vol. 11, No. 18, pp. 4546–4562, 2020.

116. Hou, G., L. Bi, B. Li, and L. Wu, "Reaction Controlled Assemblies of Polyoxotungstates (-molybdates) and Coordination Polymers", *Inorganic Chemistry*, Vol. 49, No. 14, pp. 6474–6483, 2010.

117. De Oliveira, C. A. F. *et al.*, "Effect of Temperature on Formation of Two New Lanthanide Metal-Organic Frameworks: Synthesis, Characterization and Theoretical Studies of Tm(III)-Succinate", *Journal of Solid State Chemistry*, Vol. 197, pp. 7–13, 2013.

118. McKinstry, C., E. J. Cussen, A. J. Fletcher, S. V. Patwardhan, and J. Sefcik, "Effect of Synthesis Conditions on Formation Pathways of Metal Organic Framework (MOF-5) Crystals", *Crystal Growth & Design*, Vol. 13, No. 12, pp. 5481–5486, 2013.

119. Minh, T. T., N. H. Phong, H. van Duc, and D. Q. Khieu, "Microwave Synthesis and Voltammetric Simultaneous Determination of Paracetamol and Caffeine Using an MOF-199-based electrode", *Journal of Material Science*, Vol. 53, No. 4, pp. 2453–2471, 2018.

120. Lai, L. S., Y. F. Yeong, N. Che Ani, K. K. Lau, and M. S. Azmi, "Effect of the Solvent Molar Ratios on the Synthesis of Zeolitic Imidazolate Framework 8 (ZIF-8) and Its Performance in CO_2 Adsorption", *Applied Mechanics and Materials*, Vol. 625, pp. 69–72, 2014.

121. Wang, S., X. Xie, W. Xia, J. Cui, S. Zhang, and X. Du, "Study on the Structure Activity Relationship of the Crystal MOF-5 Synthesis, Thermal Stability and N_2 Adsorption Property", *High Temperature Materials and Processes*, Vol. 39, No. 1, pp. 171–177, 2020.

122. Xu, H., J. Huang, C. Lin, J. Zheng, Z. Qiu, Q. Wen, Y. Chen, L. Qi, and Y. Wang, "Bio-functional Metal Organic Framework Composite as Bioanode for Enhanced Electricity Generation by a Microbial Fuel Cell", *Electrochimica Acta*, Vol. 368, p. 137622, 2021.

123. Lili, F., Z. Kang, M. Li, and D. Sun, “Recent Progress in Pristine MOF-based Catalysts for Electrochemical Hydrogen Evolution, Oxygen Evolution and Oxygen Reduction”, *Dalton Transactions*, Vol. 50, No. 17, pp. 5732–5753, 2021.

124. Murase R., C. F. Leong, and D. M. D’Alessandro, “Mixed Valency as a Strategy for Achieving Charge Delocalization in Semiconducting and Conducting Framework Materials”, *Inorganic Chemistry*, Vol. 56, No. 23, pp. 14373–14382, 2017.

125. Fu, S., C. Zhu, J. Song, D. Du, and Y. Lin, “Metal-Organic Framework-Derived Non-Precious Metal Nanocatalysts for Oxygen Reduction Reaction”, *Advanced Energy Materials*, Vol. 7, No. 19, p. 1700363, 2017.

126. Lu, X. F., B. Y. Xia, S. Zang, and X. W. (David) Lou, “Metal–Organic Frameworks Based Electrocatalysts for the Oxygen Reduction Reaction”, *Angewandte Chemie International Edition*, Vol. 59, No. 12, pp. 4634–4650, 2020.

127. Han, L., X.-Y. Yu, and X. W. D. Lou, “Formation of Prussian-Blue-Analog Nanocages via a Direct Etching Method and Their Conversion into Ni-Co-Mixed Oxide for Enhanced Oxygen Evolution”, *Advanced Materials*, Vol. 28, No. 23, pp. 4601–4605, 2016.

128. You, S., X. Gong, W. Wang, D. Qi, X. Wang, X. Chen, and N. Ren, “Enhanced Cathodic Oxygen Reduction and Power Production of Microbial Fuel Cell Based on Noble-Metal-Free Electrocatalyst Derived from Metal-Organic Frameworks”, *Advanced Energy Materials*, Vol. 6, No. 1, p. 1501497, 2016.

129. Satık, E., B. Topuz, and H. A. Yurtsever, “Sentez Koşullarının ve Çinko Öncülünün ZIF-L Membranlarının Gaz Geçirgenlik Özelliklerine Etkisi”, *Deu Muhendislik Fakultesi Fen ve Muhendislik Dergisi*, Vol. 18, No. 54, pp. 333–349, 2016.

130. Tan, P.C., O. B. Seng, A. L. Ahmad, and L. S. Chun, “Size Control and Stability Study of Zeolitic Imidazolate Framework-8 to Prepare Mixed Matrix Membrane”, *Journal of Physical Science*, Vol. 28, No. Suppl. 1, pp. 215–226, 2017.

131. Zhou L., N. Li, G. Owens, and Z. Chen, “Simultaneous Removal of Mixed Contaminants, Copper and Norfloxacin, from Aqueous Solution by ZIF-8”, *Chemical Engineering Journal*, Vol. 362, pp. 628–637, 2019.

132. Shi, X., N. Iqbal, S. S. Kunwar, G. Wahab, H. A. Kasat, and A. M. Kannan, “Pt Co@NCNTs Cathode Catalyst Using ZIF-67 for Proton Exchange Membrane Fuel Cell”, *International Journal of Hydrogen Energy*, Vol. 43, No. 6, pp. 3520–3526, 2018.

133. Fu, H., X.-X. Song, L. Wu, C. Zhao, P. Wang, and C.-C. Wang, “Room-Temperature Preparation of MIL-88A as a Heterogeneous Photo-Fenton Catalyst for Degradation of Rhodamine B and Bisphenol a Under Visible Light”, *Materials Research Bulletin*, Vol. 125, p. 110806, 2020.

134. Pednekar, P. P., S. C. Godiyal, K. R. Jadhav, and V. J. Kadam, “Mesoporous Silica Nanoparticles: A Promising Multifunctional Drug Delivery System”, *Nanostructures for Cancer Therapy*, Elsevier, 2017.

135. Moseley, H. G. J. and C. G. Darwin, “XIV. The Reflexion of the X-Rays”, *The London, Edinburgh, and Dublin Philosophical Magazine and Journal of Science*, Vol. 26, No. 151, pp. 210–232,1913.

136. Sekar, N. and R. P Ramasamy, “Electrochemical Impedance Spectroscopy for Microbial Fuel Cell Characterization”, *Journal of Microbial and Biochemical Technology*, Vol.5, 2013.

137. Cholewinski A., P. Si, M. Uceda, M. Pope, and B. Zhao, “Polymer Binders: Characterization and Development toward Aqueous Electrode Fabrication for Sustainability”, *Polymers (Basel)*, Vol. 13, No. 4, p. 631, 2021.

138. Sánchez C., P. Dessì, M. Duffy, and P. N. L. Lens, “Gauging Sediment Microbial Fuel Cells Using Open-Circuit Auxiliary Electrodes”, *Journal of Power Sources*, Vol. 527, p. 231216, 2022.

139. Nahir, T. M., R. A. Clark, and E. F. Bowden, “Linear-Sweep Voltammetry of Irreversible Electron Transfer in Surface-Confined Species Using the Marcus Theory”, *Analytical Chemistry*, Vol. 66, No. 15, pp. 2595–2598, 1994.

140. Wang T. *et al.*, “2D Dual-Metal Zeolitic-Imidazolate-Framework-(ZIF)-Derived Bifunctional Air Electrodes with Ultrahigh Electrochemical Properties for Rechargeable Zinc-Air Batteries”, *Advanced Functional Materials*, Vol. 28, No. 5, p. 1705048, 2018.

141. Wijaya C. J., S. Ismadji, H. W. Aparamarta, and S. Gunawan, “Facile and Green Synthesis of Starfruit-Like ZIF-L, and Its Optimization Study”, *Molecules*, Vol. 26, No. 15, p. 4416, 2021.

142. Park, K. S., Z. Ni, A. P. Cote, J. Y. Choi, R. Huand, F. J. Uribe-Romo, H. K. Chae, M. O’Keeffe, and O. M. Yaghi, “Exceptional Chemical and Thermal Stability of Zeolitic Imidazolate Frameworks”, *Proceedings of the National Academy of Sciences*, Vol. 103, No. 27, pp. 10186–10191, 2006.

143. Xie E., L. Zheng, X. Li, Y. Wang, J. Dou, A.Ding, and D. Zhang, “One-Step Synthesis of Magnetic-TiO2-Nanocomposites with High Iron Oxide-Composing Ratio for Photocatalysis of Rhodamine 6G”, *Plos One*, Vol. 14, No. 8, pp. 1-19, 2019.

144. Zhang J., T. Zhang, D. Yu, K. Xiao, and Y. Hong, “Transition from ZIF-L-Co to ZIF-67: A New Insight Into the Structural Evolution of Zeolitic Imidazolate Frameworks (ZIFs) in Aqueous Systems”, *CrystEngComm*, Vol. 17, No. 43, pp. 8212–8215, 2015.

145. Hou, W., Y. Huang, and X. Liu, “Highly Efficient and Recyclable ZIF-67 Catalyst for the Degradation of Tetracycline”, *Catalysis Letters*, Vol. 150, No. 10, pp. 3017–3022, 2020.

146. Li, Y., Y. Yang, D. Chen, Z. Luo, W. Wang, Y. Ao, L. Zhang, Z. Yan, and J. Wang, “Liquid-Phase Catalytic Oxidation of Limonene to Carvone over ZIF-67(Co)”, *Catalysts*, Vol. 9, No. 4, p. 374, 2019.

147. Guo, X., T. Xing, Y. Lou, and J. Chen, “Controlling ZIF-67 Crystals Formation Through Various Cobalt Sources in Aqueous Solution”, *Journal of Solid State Chemistry*, Vol. 235, pp. 107–112, 2016.

148. Benistez, A., J. Amaro-Gahete, D. Esquivel, F. J. Romero-Salguero, J. Morales, and Á. Caballero, “MIL-88A Metal-Organic Framework as a Stable Sulfur-Host Cathode for Long-Cycle Li-S Batteries”, *Nanomaterials*, Vol. 10, No. 3, p. 424, 2020.

149. Sert, E., E. Yılmaz, and F. S. Atalay, “Comparison of Solvothermal and Ionothermal Methods on Catalytic Activity of MIL-53(Fe)”, *Anadolu University Journal of Science and Technology A - Applied Sciences and Engineering*, Vol. 18, No. 5, pp. 1107-1117, 2017.

150. Xie, Q., Y. Li, Z. Lv, H. Zhou, X. Yang, J. Chen, and H. Guo, “Effective Adsorption and Removal of Phosphate from Aqueous Solutions and Eutrophic Water by Fe-based MOFs of MIL-101”, *Scientific Reports*, Vol. 7, No. 1, p. 3316, 2017.

151. Iqbal, B., M. Saleem, S. N. Arshad, J. Rashid, N. Hussain, and M. Zaheer, “One-Pot Synthesis of Heterobimetallic Metal–Organic Frameworks (MOFs) for Multifunctional Catalysis”, *Chemistry – A European Journal*, Vol. 25, No. 44, pp. 10490–10498, 2019.

152. Shao, L., Z. Yu, X. Li, X. Li, H. Zeng, and X. Feng, “Carbon Nanodots Anchored onto the Metal-Organic Framework NH_2-MIL-88B(Fe) as a Novel Visible Light-Driven Photocatalyst: Photocatalytic Performance and Mechanism Investigation”, *Applied Surface Science*, Vol. 505, p. 144616, 2020.

153. Benito, J., M. Fenero, S. Sorribas, B. Zornoza, K. J. Msayib, N. B. McKeown, C. Tellez, J. Coronas, and I. Gascon, “Fabrication of Ultrathin Films Containing the Metal Organic Framework Fe-MIL-88B-NH_2 by the Langmuir–Blodgett Technique”, *Colloids and Surfaces A: Physicochemical and Engineering Aspects*, Vol. 470, pp. 161–170, 2015.

APPENDIX A: COPYRIGHT NOTICES

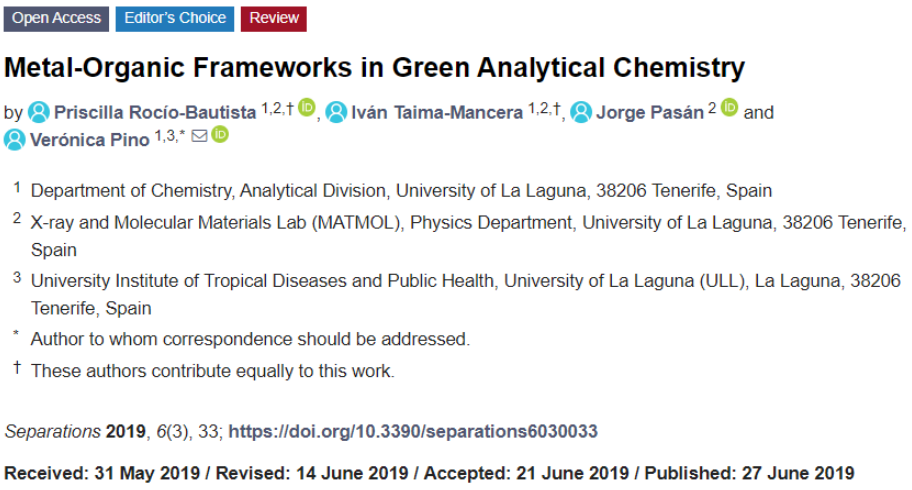


Bimetallic metal–organic frameworks and their derivatives

L. Chen, H. Wang, C. Li and Q. Xu, *Chem. Sci.*, 2020, **11**, 5369 **DOI:** 10.1039/D0SC01432J

This article is licensed under a Creative Commons Attribution 3.0 Unported Licence. **You can use material from this article in other publications without requesting further permissions** from the RSC, provided that the correct acknowledgement is given.

Figure A.1. Copyright notice for Figure 1.6. Reproduced from Ref. 82 with permission from the Royal Society of Chemistry.



Open Access Editor's Choice Review

Metal-Organic Frameworks in Green Analytical Chemistry

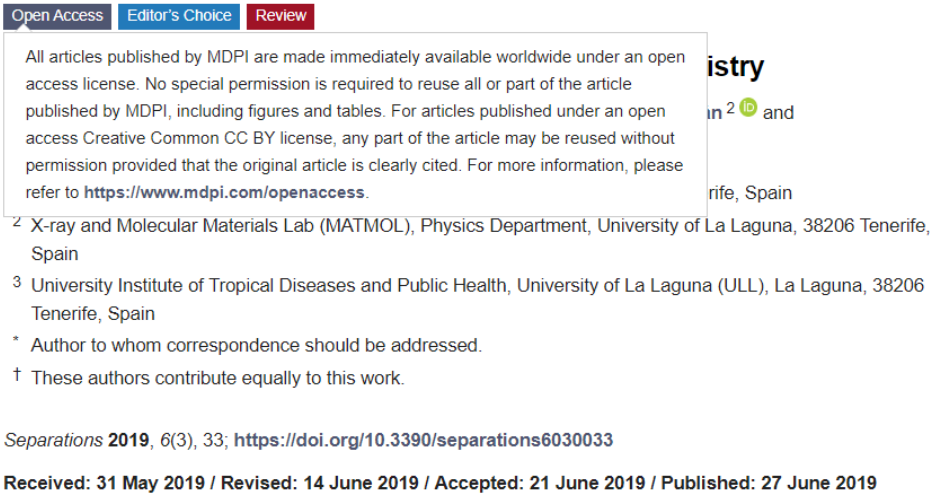
by **Priscilla Rocío-Bautista** [1,2,†], **Iván Taima-Mancera** [1,2,†], **Jorge Pasán** [2] and **Verónica Pino** [1,3,*]

[1] Department of Chemistry, Analytical Division, University of La Laguna, 38206 Tenerife, Spain
[2] X-ray and Molecular Materials Lab (MATMOL), Physics Department, University of La Laguna, 38206 Tenerife, Spain
[3] University Institute of Tropical Diseases and Public Health, University of La Laguna (ULL), La Laguna, 38206 Tenerife, Spain
[*] Author to whom correspondence should be addressed.
[†] These authors contribute equally to this work.

Separations **2019**, *6*(3), 33; **https://doi.org/10.3390/separations6030033**

Received: 31 May 2019 / Revised: 14 June 2019 / Accepted: 21 June 2019 / Published: 27 June 2019

Figure A.2. Copyright notices for Figure 1.7.



Open Access Editor's Choice Review

All articles published by MDPI are made immediately available worldwide under an open access license. No special permission is required to reuse all or part of the article published by MDPI, including figures and tables. For articles published under an open access Creative Common CC BY license, any part of the article may be reused without permission provided that the original article is clearly cited. For more information, please refer to **https://www.mdpi.com/openaccess**.

istry

[2] and

rife, Spain

[2] X-ray and Molecular Materials Lab (MATMOL), Physics Department, University of La Laguna, 38206 Tenerife, Spain

[3] University Institute of Tropical Diseases and Public Health, University of La Laguna (ULL), La Laguna, 38206 Tenerife, Spain

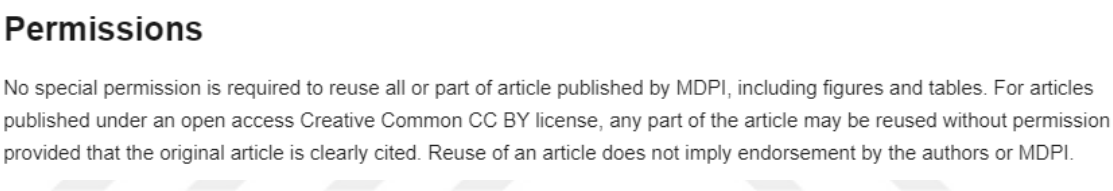
* Author to whom correspondence should be addressed.

† These authors contribute equally to this work.

Separations **2019**, *6*(3), 33; **https://doi.org/10.3390/separations6030033**

Received: 31 May 2019 / Revised: 14 June 2019 / Accepted: 21 June 2019 / Published: 27 June 2019

Figure A.3. Copyright notices for Figure 1.7.



Permissions

No special permission is required to reuse all or part of article published by MDPI, including figures and tables. For articles published under an open access Creative Common CC BY license, any part of the article may be reused without permission provided that the original article is clearly cited. Reuse of an article does not imply endorsement by the authors or MDPI.

Figure A.4. Copyright notices for Figure 1.7.